PLASMA-NEUTRAL INTERACTIONS AS AN ENERGY SINK IN THE EDGE OF THE MADISON SYMMETRIC TORUS

by

Ryan J. Norval

A dissertation submitted in partial fulfillment of
the requirements for the degree of

Doctor of Philosophy

(Engineering Physics)

at the

UNIVERSITY OF WISCONSIN–MADISON

2019

Date of final oral examination: 03/25/19

The dissertation is approved by the following members of the Final Oral Committee:
Oliver Schmitz, Professor, Engineering Physics
John Sarff, Professor, Physics
Chris C. Hegna, Professor, Engineering Physics
Raymond Fonck, Professor, Engineering Physics
John A. Goetz, Senior Scientist, Engineering Physics

Abstract

Reversed field pinch (RFP) plasmas are high density, moderate temperature plasmas, which efficiently utilize magnetic fields for fusion research and astrophysical studies. RFPs are operated with either a multihelicity (MH) or a quasi-single helicity (QSH) magnetic core. Core plasma confinement and heating is the main goal of RFP research. The influence of the plasma edge on the RFP energy balance has not been systematically studied. The Madison Symmetric Torus (MST), a large RFP device with a limiter, is ideal for studying the plasma-wall interaction (PWI) in the RFP edge. The RFP edge is a domain with a high fraction of neutral particles produced by neutralization of impinging plasma ions on the vessel wall and limiter. Neutral particles affect the plasma energy balance through the processes of dissociation, ionization, charge exchange, and radiation. In this work, boundary-viewing cameras are used to image the plasma edge. Absolute calibration of the camera system enables measurement of the D_α photon flux generated by PWI. Langmuir probes measure electron density (n_e) and electron temperature (T_e) in the edge. Core n_e and T_e are measured by an interferometer and a Thomson scattering diagnostic respectively. Knowledge of n_e and T_e is required to convert photon fluxes into particle fluxes by converting D_α atomic line emission intensities into particle fluxes using appropriate atomic data for excitation and radiative decay of the relevant line transitions. A helical bulge in the plasma pressure was discovered in QSH plasmas. The edge pressure maximum is phase-aligned to the magnetic mode in the plasma core domain. By referring to these experimental data from cameras and Langmuir probes, a three-dimensional (3D) plasma edge temperature and density was constructed and used to the fully model the 3D kinetic neutral particle

model EIRENE. A method of comparison between modeled EIRENE images of D_α emission with experimental data served as a first detailed benchmark for MST. Synthetic images are compared to experimental images validating the EIRENE model. For the first time, 3D profiles of neutral density in MST are constructed using EIRENE. This fully 3D neutral distribution then enabled an investigation of the role of neutral particles to the RFP energy balance. Neutral particles account for a significant percentage of power loss in QSH plasmas. Neutral particles account for up to 30% of the power losses in the plasma edge domain of MST. The main fraction is established by electron-impact ionization and molecular dissociation events. The remaining fraction is dissipated by charge-exchange. By injecting gas directly into the helical bulge, a QSH plasma may be fueled at 74% efficiency compared to 52% fueling efficiency at other locations. The localization of the PWI in the QSH mode may be exploitable in future RFPs by designing divertor-like edges where particles can be effectively pumped out. In addition control of the PWI could reduce energy losses in QSH plasma by up to 20% of total input power. Understanding the magnitude of these losses and what drives them can lead to improved optimization of the RFP as a fusion device.

Acknowledgments

Graduate school, anyway I slice it, has been one wild ride. I'm not certain I would have completed the journey by myself. I am grateful for the quantity and quality of the people around me during my graduate career. I would like to take this time to thank everyone who has helped me make my dreams of becoming a Ph.D. come true.

First and foremost, I would like to thank my undergraduate advisor, Dr. Danon. He planted the seed in my mind that graduate school and a Ph.D. were possible paths I should consider. He helped me to look beyond a dual (BS/MS) degree program. I'd like to thank all my roommates from RPI, specifically Jim, Asher, and Richard. Thank you for keeping in touch long after we parted and always asking me for my opinion on every fusion related news article you have seen.

I have made many friends out of the coworkers and classmates in graduate school. Marcos, Matt, and Kyle, thanks for making my time at UW the most memorable time in my life so far. You are some of the best people I have had the pleasure to know. On the MST team, I have come to see many of the other students, engineers, and scientists as friends as well. Peter Weix and Abdualgader Almagri, thank you for reminding me science is a hands-on and sometimes dirty process, whether it is from the regular maintenance of the vacuum equipment in the lab, or testing and calibrating probes. To my mentors and advisors in graduate school, John Goetz and Oliver Schmitz, thank you for having faith in me while I had my existential crisis. Finishing this dissertation is one of my crowning life achievements, and I would never have done it without the wisdom you shared along the way. Oliver's voice will be in the back of my head. It will always remind me that science

is a creative process. Ph.Ds. are those who can innovate, pull meaning out of the madness. Every time I have a eureka moment, I will look back and remember that advice.

And finally, I will thank the most important people in my life. Thank you to my parents, for never letting me forget that education is required to have a successful life. I have had so much opportunity for success, thanks to my pursuit of higher education. It all stems from the constant reminders that I must do well in school to do well in life. Everyone knows pursuing a Ph.D. is a stressful process. I can never provide enough cat treats to my feline friend, Jayna. She helped keep me on a sound sleep schedule and provided me with endless joy through her hide and seek antics. Finally, Kelsey, I'm sorry this has taken me so long to get together, but the hard work is done now. It would not have been possible without all your help. Here is to enjoying the rest of my life with you.

Contents

Abstract i

Contents v

List of Tables vii

List of Figures viii

1 Introduction 1
- *1.1 Nuclear fusion* 3
- *1.2 Axisymmetric or helical RFPs* 10
- *1.3 Overview of the MST RFP* 13
- *1.4 An overview of edge physics and phenomena* 18
- *1.5 Thesis overview and structure* 22

2 Experimental design and diagnostics details 24
- *2.1 Modeling of the MST edge and experimental design* 26
- *2.2 Diagnostic tools and analysis methods* 31
- *2.3 Computational tools and code details* 47

3 Breaking symmetry in the MST edge 60
- *3.1 Helical deformation of the QSH edge* 60
- *3.2 Properties of the QSH edge* 65
- *3.3 General survey of the plasma boundary* 74
- *3.4 Bolometer observation of plasma edge* 83

4 Numerical analysis of the 3D neutral particle distribution and associated power losses 87
- *4.1 Plasma backgrounds in the model* 87
- *4.2 Neutral sources in the model* 95
- *4.3 Validation of the synthetic model* 102
- *4.4 Fully 3D neutral profile computations* 107
- *4.5 Plasma-neutral losses* 115

5 Summary and Future Work 131
- *5.1 Summary and conclusion* 131
- *5.2 Future work* 134

Bibliography 136

List of Tables

1.1 Representative electron temperature and energy confinement time for MH plasmas 16
1.2 Representative electron temperature and energy confinement time for QSH plasmas 17

2.1 Recommended operating settings for the boundary viewing cameras . 41
2.2 Reactions utilized in the EIRENE modeling 48
2.3 Effective S/XB coefficients for each of BVC generated through simulation 59

4.1 EIRENE calculations for the energy lost per charge exchange event over a range of currents in both MH and QSH plasmas 128

List of Figures

1.1 Two views highlighting the macroscopic difference between MH and QSH RFPs . . . 1
1.2 Impurity transport scheme for limited plasma . . . 3
1.3 Hydrogen reaction rates for 1 ev to 1000 eV plasma for the most commons plasma-neutral interactions. . . . 6
1.4 Overview of the energy pathways for the RFP . . . 9
1.5 Cartoons of enhanced confinement schemes for the RFP . . . 10
1.6 A sketch of the general RFP configuration . . . 12
1.7 The MST coordinate system with limiters overlaid . . . 13
1.8 q-profile of MST, with resonant tearing modes labeled . . . 15
1.9 Typical 400 kA MH RFP time traces of plasma current, density, reversal parameter, and magnitude mode amplitudes. . . . 16
1.10 Typical 500 kA QSH RFP time traces of plasma current, density, reversal parameter, and magnitude mode amplitudes. . . . 18
1.11 Cartoon sketch labeled with the regions of a MH RFP plasma with a limiter boundary . . . 19

2.1 Generalized transport scheme for neutral recycling . . . 25
2.2 Scheme for the coupling of MST experiment data and EIRENE modeling 28
2.3 Density trace for curve fitting routine in gas injection experiments . . . 30
2.4 Comparison of the magnetic signature of MH, QSH, and PPCD discharges. Activity is surpressed in QSH and PCCD modes. . . . 33
2.5 Schematic of the MST active feedback system . . . 34

2.6 Plasma response to RMP Application showing phase locking to any demanded phase . . . 35
2.7 Time evolution of a QSH locking event . . . 36
2.8 Boundary camera optical design with ray traces . . . 37
2.9 Boundary camera mechanical design blueprint . . . 38
2.10 A sample image output from a boundary viewing camera with in-vessel features labeled. . . . 38
2.11 Boundary camera wavelength response curve showing peak response in the visible but capability into the IR . . . 39
2.12 A plot of bandpass filters Gaussians overlaid on lines searched for during an impurity surveys . . . 40
2.13 Dalsa camera calibration curve showing linear camera response to observed power flux . . . 42
2.14 Schematic overview of the D_α array . . . 45
2.15 Bolometer set up on MST . . . 46
2.16 Bolometer sensitivity curve to photons of energy 1 to 10000 eV . . . 47
2.17 EIRENE workflow overview showing inputs the kinds of input data into the model as well as output quantities of interest. . . . 50
2.18 Mapping based on V3Fit used for EIRENE cells . . . 51
2.19 V3Fit flux surfaces for an example QSH plasma . . . 52
2.20 V3Fit temperature and density profiles as a function of enclosed flux . . . 53
2.21 Mapping based on V3Fit used for EIRENE cells . . . 53
2.22 Deuterium refection on carbon from TRIM database at 6 different incidence angles. . . . 54
2.23 Eirene geometry construction for MST including the pump duct. A few sample trajectories are shown. . . . 55
2.24 A sampling of S/XB coefficients in a 400 kA QSH plasma . . . 58

3.1 Cartoon of Langmuir probe locations and V3Fit flux surfaces . . . 61
3.2 Electron temperature as measured by Langmuir probes in the edge . . . 62
3.3 Plasma density as measured by Langmuir probes in the edge . . . 63

3.4 Pressure in the MST edge as measured by Langmuir probes 64
3.5 Edge Pressure contours constructed based on probe data 65
3.6 Photon emission measured by BVCs for 400 kA QSH and MH plasmas 67
3.7 QSH recycling fluxes decrease linearly with increasing QSH presence . 68
3.8 Recycling coefficient vs. Mode phase in QSH plasmas 71
3.9 Experimental measurements of effective fueling 72
3.10 Confinement as a function of phase measurements in QSH 72
3.11 Experimental results showing saturation in the walls of MST 74
3.12 Image for 200 kA plasma overlaid with zones of interest used to determine features of the PWI 75
3.13 Toroidal variation in standard plasma for band-like structures at the edge 76
3.14 PWI in higher current MH plasmas is measured to be uniform in time and space 77
3.15 Time evolution of 200 kA MH recycling fluxes from each of the BVC views. 78
3.16 400kA Recycling Flux 79
3.17 Variation in Balmer photon flux as a function of plasma current 80
3.18 Emission variation with reversal 81
3.19 Impurity radiation in MST over the visible range 83
3.20 Bolometer Observations of the QSH Edge 84
3.21 Bolometer Observations of the MH Edge 86

4.1 Plasma background fields for V3Fit for 400 kA QSH plasma 88
4.2 Combined electron temperature backgrounds of V3Fit and probe data for QSH plasma with only edge data 90
4.3 Combined electron temperature backgrounds of V3Fit and probe data for QSH plasma 92
4.4 Combined plasma density backgrounds of V3Fit and probe data for QSH plasma. 94
4.5 Synthetic image results of recycling coefficent scan in EIRENE 97
4.6 Synthetic image results of a source ratio (distribution) scan in EIRENE 100

4.7 Comparison an EIRENE syntehtic image after tuning the EIRENE model to best replicate the experiment . . . 101
4.8 Comparison between synthetic and experimental D_α signals for 400 kA QSH plasma. . . . 103
4.9 Comparison between synthetic and experimental D_α signals for 400 kA MH plasma. . . . 104
4.10 Comparison between synthetic and experimental D_α signals for 200 kA MH plasma. . . . 105
4.11 Temperature scan of $T_{e_{edge}}$ on D_α detector measurements . . . 107
4.12 Neutral density in a poloidal cross section of QSH plasma . . . 108
4.13 $R-\phi$ cross sectional cut of 500 kA and 400 kA QSH neutral density profiles showing a 5-period pattern in neutral density. . . . 110
4.14 Neutral density profiles in the standard RFP plasma vs plasma current 113
4.15 $R-\phi$ cross-sectional cut of 200 and 400kA MH neutral density profiles 114
4.16 EIRENE results of electron-neutral losses plotted as poloidal cross sections at Φ=0°,18°,36° . . . 117
4.17 Ion neutral losses in a QSH cross-section, Φ=0 . . . 119
4.18 Density scaling of plasma-neutral losses . . . 120
4.19 CX losses for standard MH ion profile and flat ion profiles in a helically sourced simulation . . . 123
4.20 Electron neutral losses in a cross-section of 200 and 400 kA MH plasmas 124
4.21 Charge Exchange losses in a cross-section of 200 and 400 kA MH plasmas 126
4.22 Ohmic Input power to MST in QSH (400,500 kA) and MH (200,300,400,500 kA) configuration. . . . 127
4.23 A summary of plasma-neutral losses by RFP configuration and plasma current . . . 129
4.24 A summary of fractional plasma-neutral losses by RFP configuration and plasma current . . . 130

Chapter 1

Introduction

The reversed field pinch (RFP) can experience a transition between an axisymmetric and a helical state [1, 2] allowing researchers to study three dimensional (3D) physics. This topological transformation improves electron energy confinement and shifts the core plasma to a 3D helical structure. The primary focus of this thesis is the analysis of the transition from the multihelical (MH) state to the quasi-single helicity (QSH) state with respect to the neutral particle sources and associated energy sinks. The plasma-wall interaction (PWI) of each confinement state for the RFP along with a CAD image of the vessel interior are shown in Figure 1.1.

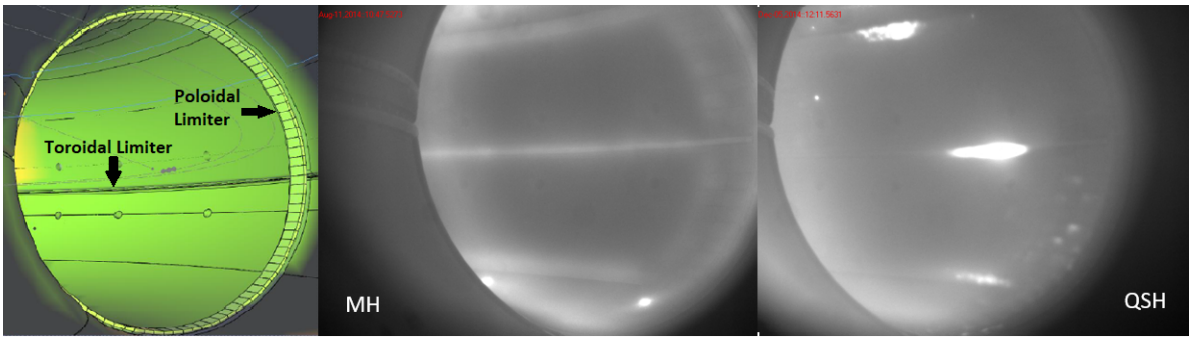

Figure 1.1: Two images taken by the newly developed boundary viewing cameras highlighting the macroscopic difference between MH and QSH RFPs. A CAD view of the interior of MST is on the left. Camera images are composed of light collected from emission of the Balmer-alpha transition of the deuterium atom. The center image is a standard 400 kA RFP in the MH state. The right image is a 400 kA QSH RFP. The MH wall recycling is uniform across the limiter while the QSH state produces a wall recycling that is localized.

A D_α (Balmer series emission from the n=3 to n=2 state) light image of wall recycling in the MH state is shown in the center image of Figure 1.1. The brightest spots on the image indicate where the PWI is occurring. These are located on the outboard belt limiter, located horizontally about the center of the image. The interaction is uniform throughout

the edge. A D_α light image of QSH wall recycling is shown in the right of Figure 1.1. Bright regions observed on the limiters are a consequence of the PWI between the helical plasma and outboard limiter. A helical structure can be seen starting from the bottom contact point, moving left and upwards in the image (a short toroidal distance and larger poloidal distance). The PWI in the image is the helical footprint of the m/n=1/5 core magnetic mode extending to the plasma edge.

This work focuses on how neutral particles, produced by PWI in the edge of a limited plasma, act as an energy sink through plasma-neutral interactions. This work studies the transition from MH to QSH limited RFPs focusing on the production of neutrals by recycling, and the energy losses as a result of the neutrals entering the plasma. A simplified version of the production, recycling, and transport scheme for neutrals is shown in Figure 1.2. In the Figure, neutrals produced from plasma hitting the limiter exit into the scrape-off layer (SOL), move through the edge, and enter the core to be ionized. These ions eventually exit the core and the recycling process restarts. Identification of the neutral source and assessment of its impact on the energy balance has implications for the particle and energy confinement times. Particle and energy confinement times are metrics that define how well a fusion device performs [3, 4]. Understanding the magnitude of these losses and what drives them can lead to improved optimization of the RFP as a fusion device.

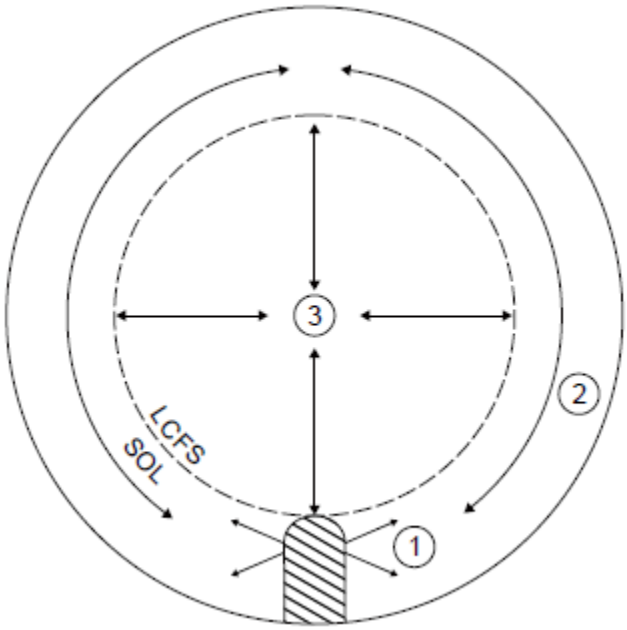

Figure 1.2: An impurity transport scheme for limited plasma reproduced from Stangeby's Figure 6.3 [3]. 1 represents the source of neutral particles from recycling on the limiter. 2 represents the transport of particles in the scrape-off layer. 3 represents the core transport with ions and neutrals both entering and exiting the core.

1.1 Nuclear fusion

Plasma is the most ubiquitous form of matter in the universe, comprising the stars, black hole accretion disks, and interplanetary media. A plasma is a group of fully or partially ionized particles that undergo collective electromagnetic interactions. A plasma is obtained by adding energy into a gaseous system in order to excite atoms which emit electrons, causing a separation of charges, but maintaining a quasi-neutral behavior. Once separated, the electrons and ions are subject to long-range electromagnetic forces. Nuclear fusion occurs in stars. The goal of fusion research is to replicate the process taking place in these stars and harness the energy of these reactions in a confined manner in order to produce electricity [5].

The first step of nuclear synthesis is the fusion of hydrogen (H) in stars. Hydrogen isotopes of deuterium (D) and tritium (T) have higher cross sections for reaction the standard hydrogen. The most common fusion reactions are shown below with the energy they produce. The D+T reaction has the lowest technical requirements, having a reaction cross-section that peaks at lower temperatures than the others. The D+He^3 reaction is

more difficult to achieve and has no neutron radiation [5].

$$D + D \longrightarrow {}^{3}He + n + 3.27MeV$$

$$D + D \longrightarrow T + p + 4.03MeV$$

$$D + {}^{3}He \longrightarrow \alpha + p + 18.3MeV$$

$$D + T \longrightarrow \alpha + n + 17.6MeV$$

Two types of reactor schemes are commonly studied: magnetic confinement devices and inertial confinement devices. Magnetic confinement devices use magnetic fields to confine the plasma. Energy production from a plasma requires long confinement times and high particle densities. Confinement is made possible by a combination of Lorentz forces and the cyclical motion of charged particles around magnetic field lines. Inertial confinement fusion devices use solid fuel and blast the target with laser or mechanical shocks to compress and heat the particles. The goal is for energy production to exceed the energy used to compress the fuel before the target expands and cools.

When technically realized, nuclear fusion will offer serval advantages over other power sources. Unlike nuclear fission, fusion plants pose no risk of meltdown and produce significantly less radioactive waste. Unlike the more intermittent sources of wind and solar power, fusion plants have the potential to function as baseload electricity generators. In order to produce energy, the plasma core needs to be hot, dense, and well confined. The Lawson criterion defines this minimum requirement as:

$$n\tau_E \geqslant \frac{12}{E_{ch}\frac{k_B T}{\langle \sigma v \rangle}} \tag{1.1}$$

where n is the plasma density, τ_E is the energy confinement time, E_{ch} is the energy of charged fusion products (assumed to redeposit in the plasma), k_B is the Boltzmann constant, T is a temperature, and $\langle \sigma v \rangle$ is a rate coefficient averaged over a temperature distribution. This quantity is a function of temperature with a minimum near 25 keV for D-T fusion (higher for other fuels). Energy confinement time is one of the most important metrics of a plasma confinement scheme in this criterion. There are many factors which can prevent plasma from achieving good confinement. The focus of this thesis is energy losses from neutral particles which interact with confined plasma. Neutrals in a plasma travel multiple mean free paths, react by change exchange or ionization, and eventually, if they are not ionized, break free from magnetic confinement and carry their energy to the vessel walls or limiting surfaces. In previous research, the main focus on the RFP energy

balance has been on core transport, and ways to reduce it [6–10]. A complete picture of the RFP energy balance is lacking. One area which has not been systematically studied is the losses due to plasma-neutral interaction at the edge of RFPs.

1.1.1 Neutrals in fusion plasma

Neutrals provide a particle supply to the plasma and consume energy during ionization. There are many possible reactions to consider between the plasma and the neutrals. Many kinds of reactions can occur. Neutral atoms and molecules can be excited from electron (and far less likely ion) collisions. Excited neutrals can, over time, de-excite by photon emission. Neutrals may also become ionized by electron impacts, the ionization does not necessarily have to dissociate a molecule. Ionized molecules would then be affected by the electric and magnetic fields of a plasma all while likely to undergo another collision that may excite or dissociate the ionized molecule. In addition ion collisions with neutrals can transfer electrons, so-called charge exchange that switches the velocities of the neutral and ion. The number of basic processes that can occur can become large in a detailed analysis. Furthermore the rate the plasma-neutral interactions occur depends on the temperature and density of the plasma which the neutral is interacting with. The temperature dependence is strongly non-linear. In a non-uniform plasma, as many experimental and naturally occurring plasmas are, this further complicates analysis. A detailed analysis of plasma-neutral interaction can be conducted by numerical simulation codes. A summary of hydrogen atomic and molecular reactions over a range of plasma temperature is shown in Figure 1.3 referenced from Stangeby [3].

The collisions with the most significant reaction rate coefficients, $\langle \sigma v \rangle$, in the expected temperature range of fusion plasma edges (1-100 eV) are further discussed. First discussed are electron-ionization events. Through these events, atoms or molecules are ionized. Excitation events are a second type of electron collision that excite a atom or molecule rather than ionize it. Excitation collisions will excite the bound electrons, which usually releases the extra energy as photon radiation. As neutrals may also be released as molecules, they are often first dissociated by plasma-neutral collisions. In dissociation the neutrals can also be excited post collision leading to photon emission. Below 8 eV it is more likely by a factor of a 2-3 that a neutral is dissociated by electron impact rather than ionized as a molecule. Over 8 eV it becomes more likely that a neutral molecule will be ionized in a electron-neutral collision. At around 100 eV electron-neutral collisions are more likely to break a molecule into an ion and neutral than to dissociate it into two neutrals. Over the entire temperature range considered, the highest reaction rate coefficient is for the dissociation of singly ionized $D^+{}_2$ into a D atom and D^+ ion. As these molecules are broken

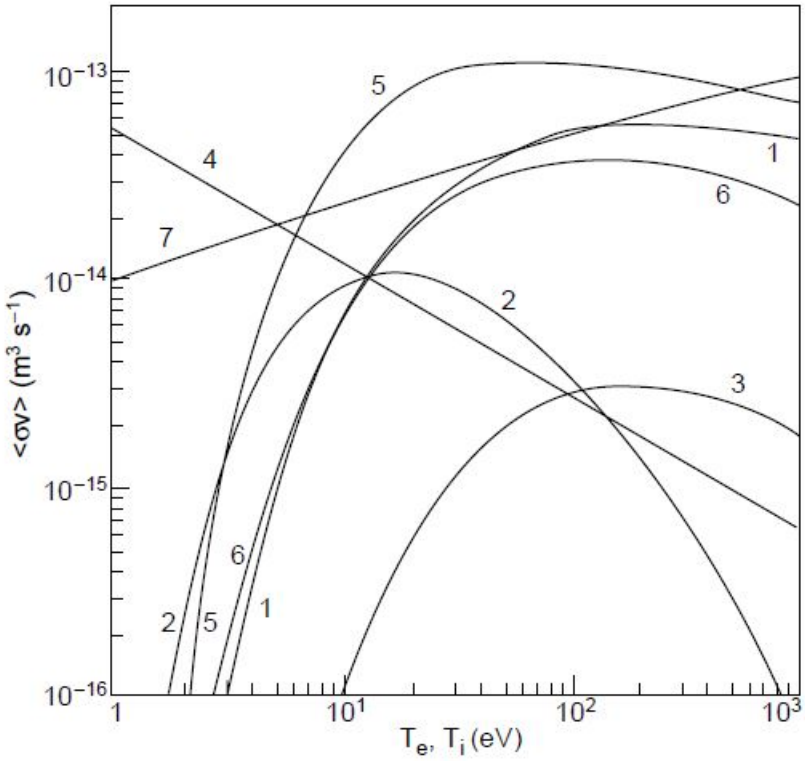

Figure 1.3: A visual summary of hydrogen reaction rates from Stangeby's Figure 1.25. [3]. 1 is molecular ionization, 2 is molecular dissociation to two neutrals, 3 is molecular dissociation to a neutral and an ion, 4 is the dissociation of an ionized molecule to a pair of neutrals, 5 is dissociation of an ionized molecule to a neutral and ion, 6 is atomic ionization and 7 is charge exchange.

down the atomic deuterium that results can have kinetic energy of 1-4 eV from the energy released in dissociation. These neutrals with a few eV of kinetic energy have much longer mean free paths in the plasma.

Charge exchange is a process where an ion impacts a neutral molecule and the bound electron is transferred. Pre-collision, the ions are typically hot, and the neutrals move at thermal velocity, post-collision, the ion is moves at a thermal velocity and the neutral is accelerated. Other processes such as excitation of neutrals by ion collision could also occur, but have negligible reaction rate coefficients in most fusion relevant plasma edge regions [3].

Energy transport can occur during a charge exchange event between a slow neutral and a fast plasma ion, decreasing or relocating the energy of the plasma. The mean free path λ_{mfp} is the average distance a particle will travel, and varies strongly with the plasma

temperature and density.

$$\lambda_{mfp} = \frac{v_n}{n\langle\sigma v\rangle} \tag{1.2}$$

The $\langle\sigma v\rangle$ in the mean free path is the sum over all the possible reaction cross-sections (σ). The reaction rate coefficient is calculated in a frame of reference where the neutral particles are at rest, an approximation made due to the relative velocity of a free electron to a thermal neutral. v_n is the neutral velocity, with faster neutrals having longer mean free paths. $\langle\sigma v\rangle$ is an average reaction rate coefficient, calculated as a weighted average over the velocity distribution. The total reactions that occur is computed as the product of the reaction rate coefficient, the neutral density, n_D, and the electron density, n_e. For reactions with ions, the ion density, n_i and temperature, T_i are used in the computations. The total reaction rate is S_{rx} is calculated as:

$$S_{rx} = n_e n_D \langle\sigma v\rangle \tag{1.3}$$

In this way the reaction rate depends on both the neutral density, plasma density, and plasma temperature. The reaction rate coefficient has a strong dependence on temperature, and a weak dependence on plasma density. The total number of reactions which occur then are influenced by the densities and the reaction rate coefficient.

The mean free path for a given reaction, such as the charge exchange path length, λ_{CX} or ionization path length, λ_{EI}, can be calculated individually. For example, consider the case of a thermal (KE « 1 eV) deuterium atom entering a plasma. The neutral is considered stationary relative to the plasma. , $\langle\sigma v\rangle_{cx}$ varies over most fusion plasma temperatures and is approximately $1x10^{-14}$ m^3s^{-1} at 1 eV up to $1x10^{-13}$ m^3s^{-1} at 1 keV. Over a short distance plasma temperature can be considered constant enough that the rate coefficient does not change much it becomes possible to estimate the ionization length scale. Assuming reasonable values of a plasma edge such as 20 eV for T_e and T_i with a n_e of $5x10^{18}$ the reaction rate coefficient of atomic ionization ($\langle\sigma v\rangle_{ei}$, process 6 in 1.3) is found be $3x10^{-14}$ m^3s^{-1} and the resulting mean free path of charge exchange is 1.6 mm. $\langle\sigma v\rangle_{ei}$ is approximately $2x10^{-13}$ m^3s^{-1}, and the mean free path to ionize is slightly longer at 2.4 mm. Each ionization event would use around 13.6 eV , the ionization potential of deuterium, which would cool the plasma slightly. A charge exchange event would transfer the kinetic energy of the neutral and ion. This phenomenon is called neutral acceleration and tends to increase neutral penetration into the plasma. A charge exchange event in the sample edge plasma initially causes a loss of 20 eV from the plasma. The new fast neutral has a λ_{mfp} of 29.8 cm. λ_{mfp} decreases in a realistic plasma which gets hotter and more dense towards the core domain, this fast neutral still has a λ_{mfp} of 5.16 mm in a $n_e = 1x10^{19}$ T_e=400 eV plasma. If a collision with a plasma ion occurs, then up to 400 eV can now be

transferred from plasma to neutral and carried to the edge or wall by the fast neutral. The constantly changing collision rates and potential for multiple reactions require a modeling solution [3]. Modeling this cycle of recycling, ionization, and transport enables a greater understanding of particle and energy balances in RFP plasmas.

Neutral particle sources are first identified to begin quantifying the energy loss through plasma-neutral interactions. This work addresses the spatial distribution of neutral particles by using EIRENE [11], a fully 3D kinetic neutral particle code, to model and construct fully 3D profiles of the neutral density under two plasma conditions: MH and QSH. These are detailed in Sections 1.3.2 and 1.3.3 over a range of plasma currents. Calculating the neutral profiles requires knowledge of the plasma background. Reconstructions from existing diagnostics such as Langmuir probes, Thomson scattering, interferometers, and magnetic arrays are used to obtain this data. This work focuses on the neutral density at the edge of the plasma and utilizes diagnostics which probe this region. In order to quantify the recycling sources in the plasma edge, a new diagnostic system of filtered cameras is utilized. A synthetic camera routine was developed for EIRENE to verify interpretation and conversion between filtered camera images and neutral sources.

1.1.2 Current understanding of the RFP edge relative to other fusion devices

RFPs require edge magnetic control such as close-fitting conducting shells to maintain plasma stability. Previous research on RFP physics focused on the core region and magnetohydrodynamic (MHD) phenomena. Both the tokamak and the stellarator have received dedicated attention to the boundary and edge physics. By understanding boundary physics in these devices, higher performance plasmas have been produced. The major discovery of previous work is the high confinement mode on tokamaks, more commonly known as H-mode [12]. The introduction of a divertor led to the observation of H-mode on W7-AS [13]. The RFP has received limited exploration in the area of boundary physics, due to the complicated nature of the confined plasma. Exploration of the boundary physics of the RFP may lead to improved control and higher performance. One example of the importance of boundary physics is how Spizzo claimed boundary physics is more related to power balance and fueling methods than a limit on RFPs and tokamaks, which is the current understanding using the Greenwald density limit [1, 14–17].

MST, a limiter device, creates an interesting edge regime of particle recycling. Neutral particles generated from recycling have direct access to the bulk plasma. Recycling was suspected of causing a large population of neutral particles at the edge of the machine. The initial question which inspired this work was “How do these neutrals affect the energy balance of MST?”.

The possible paths for energy to leave the system are shown in Figure 1.4. Energy is injected by driving plasma current. This plasma current creates magnetic fields U_f which store energy and may undergo magnetic reconnection [18] heating the ions U_i. The electrons, U_e, are directly ohmically heated and may transfer energy to the ions by collision. Energy may leave the system in the form of heat fluxes Q_e, Q_i which may be conductive or convective and through radiation P_{rad}. The energy lost through charge exchange interactions occurs when a slow neutral swaps charge with a fast ion and leaves the plasma before re-ionizing. Obtaining P_{rad} and P_{cx} is the focus of this work as they depend on the neutral population in the confinement volume.

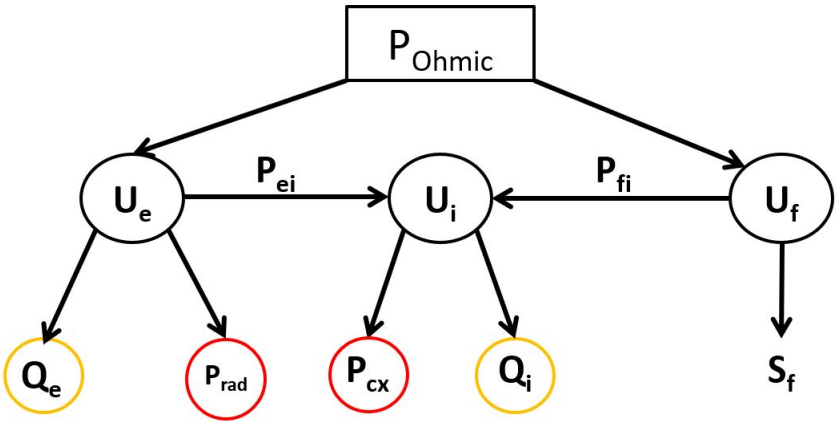

Figure 1.4: Schematic overview of the energy pathways for the RFP. An ohmic input power provides energy stored in electrons, ions, and fields U_e, U_i, U_f, and is exhausted by ion and electron heat fluxes Q_e, Q_i or neutral interactions. Of note are energy exhausted through neutral interactions in the form of P_{rad}, power radiated, and P_{CX}, energy loss due to charge exchange.

$$P_{rad} \propto n_e n_D \langle \sigma_{ex_e} v \rangle + n_i n_D \langle \sigma_{ex_i} v \rangle \tag{1.4}$$

$$P_{cx} \propto n_i n_D \langle \sigma_{cx} v \rangle \tag{1.5}$$

with n_e, n_i, and n_D being a density of electrons, ions, and neutrals. n_D is used to represent the neutral term as the plasmas studied use deuterium as the regular fuel source. The terms σ_{ex_e} and σ_{ex_i} are the cross-sections for ionization by electrons and ions respectively, of which the ion cross-section is nearly insignificant. The reaction rates depend on both local plasma temperature and density. These terms have been expressed as a proportion rather than an equation, because the energy exchanged in these reactions is again a function of

plasma temperature. EIRENE computes the two terms of P_{rad} and P_{cx} based on models in which experimental data is the foundation. These two terms represent the losses of the plasma to electron-neutral and ion-neutral interaction.

Another question arose during this work: "How does the edge of MST differ between the standard case and the QSH helical case concerning recycling and plasma-neutral interactions?". A cartoon of the transition from a multi-helicity to helical RFP is shown in Figure 1.5. Exaggerated magnetic flux surfaces of each configuration are shown in the Figure. A standard RFP is shown at the top of the Figure in the MH state. Having multiple magnetic modes with various amplitudes leads to an uneven, bumpy surface. This surface rapidly rotates inside the machine leading to symmetric measurements when time averaging data collected at a particular toroidal location. The plasma may be reconfigured with current profile control to greatly reduce the magnetic modes leading to the smooth surface shown in the lower right. If enough current is driven into the plasma, the plasma will self organize into the single helical state on the lower left. This state has a dominant mode which produces the periodic flux surfaces shown. In MST, the QSH tends to lock in place. This work investigates the effects of this transition from uniform to 3D structure in the plasma core region on the plasma edge.

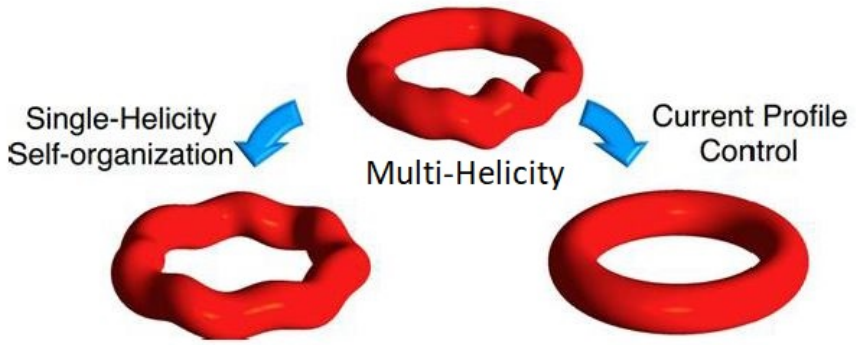

Figure 1.5: Cartoons of enhanced confinement schemes for the RFP. On the left the shift from MH to QSH is shown. On the right the transition from MH to a pulsed poloidal current drive where all magnetic perturbations are reduced is shown. Originally in [19] as Figure 1.

1.2 Axisymmetric or helical RFPs

A successful magnetic confinement system confines a plasma with magnetic forces. The macroscopic equilibrium is defined $\mathbf{J} \times \mathbf{B} = \nabla P$, where $\mathbf{J}$ is the current density, $\mathbf{B}$ is the

magnetic field and ∇P is the pressure gradient, called MHD equilibrium. Confinement results from charged particles spiraling around a magnetic field line with an orbit the size of the Larmor radius:

$$\rho_L = \frac{m v_\perp}{qB}$$

where m is the mass of the particle, q the charge and $v_\perp$ the perpendicular velocity to the magnetic field, B. These orbits are small for energetic particles. For example, a one keV deuterium ion in a 1 Tesla field would have a ρ_L of 3mm. Electron gyro-orbits are smaller than ion orbits by a factor of their mass ratio, about 2000 times smaller for deuterium plasma. Magnetic fields are needed to confine charged particles. Cylindrical configurations, such as magnetic mirrors, were first attempted but led to the discovery of large losses at the end. The change in topology from an open cylinder to closed cylinder created toroidal confinement devices. Toroidal fields alone are not sufficient to confine the plasma, as grad-B drifts lead to charge separation, which in turn leads to ExB drifts and charges migrating outward from the core region of the plasma. The addition of a poloidal magnetic field counteracts these forces, which leads to a helical field. Helical magnetic fields are required to confine plasma in a toroidal geometry [4, 20].

The RFP is a confinement concept based on magnetic self-organization. This idea originated when the external current drive was turned off in the ZETA pinch experiment, and the plasma relaxed to a more organized state [21]. Taylor worked out the theory behind this behavior and identified a minimum-energy state where the toroidal field at the edge of the plasma can be in the opposite direction of the toroidal field of the central plasma [22]. The reversal of the toroidal field is the defining characteristic of the RFP configuration. The typical RFP field configuration, with a reversed (negative) toroidal field at the edge, is shown in Figure 1.6. The Figure includes a sketch of the magnetic fields within the vacuum vessel as well as the relative amplitudes of the toroidal and poloidal fields across the midplane. Reversal can be noted by the change in direction of the toroidal field at the edge relative to the central region. This configuration utilizes magnetic fields more efficiently than the tokamak. In magnetic notation, vector components are presented in toroidal geometry. A vector such as **B** has components B_ϕ, B_θ, and B_r, where B_ϕ points along the long way around the torus/doughnut shape, B_θ points the short way around the torus and B_r points radially from the central axis outward. Any point is uniquely defined by a (ϕ, θ, r) coordinate. It is common in an RFP that $\frac{B_\phi}{B_\theta} \approx 1$ unlike the tokamak where B_ϕ is the dominant field component. Two parameters used to describe the equilibrium of an

RFP plasma are F, the reversal parameter, and θ, the pinch parameter

$$F = \frac{B_\phi(a)}{\langle B_\phi \rangle} \tag{1.6}$$

$$\theta = \frac{B_\theta(a)}{\langle B_\theta \rangle} \tag{1.7}$$

where a is the minor radius of the plasma, and B_ϕ and B_θ are the toroidal and poloidal field components. The reversal parameter and pinch parameter are the ratios of the components of the respective magnetic fields at the wall to their volume averaged value.

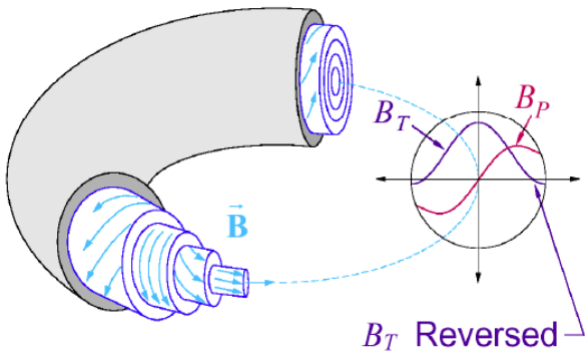

Figure 1.6: Magnetic fields in the RFP, highlighting reversal at the edge. The maximum magnitude of B_ϕ (B_T) and B_θ (B_P) is similar. Reproduced form Eilerman's Figure 1.1 [23].

When considering the RFP as a plasma confinement device, a few specific types of discharges are possible. These are standard MH RFPs, QSH discharges, and pulsed poloidal current drive discharges (PPCD). The magnetic configuration of the discharges tends to vary from the axisymmetric stochastic standard RFP configuration to the enhanced confinement discharge of the 3D QSH configuration. RFPs typically have a stochastic core, which causes rapid transport from the central region to the edge of the plasma.

The existence of this rapid transport outward in the RFP is not desired for fusion energy production, as it limits confinement. The alternate discharges QSH and PPCD produce enhanced confinement states through control of the magnetic topology. In the QSH state, a transport barrier forms which confines electron thermal energy in the new helical core region [2]. This helical state is 3D, and unlike the MH standard plasma, the magnetic modes of a QSH plasma tend to lock to fixed positions based on machine construction [24]. This locking of a 3D state to a location enables measurements of the 3D helical edge.

1.3 Overview of the MST RFP

The MST [15] is a toroidal confinement device, with a major radius of 1.5 m and minor radius 0.52 m. MST is operated with plasma currents up to 600 kA, although 200-500 kA is typical. Plasma densities are in the order of $\approx 10^{19} \mathrm{m}^{-3}$. The primary goal of research on MST has been to study basic physics issues of a toroidally confined plasma. MST is operated primarily as an RFP but may be operated as a tokamak, enabling researchers to perform experiments on both magnetic configurations. The MST coordinate system and overall geometry are shown in Figure 1.7. The outboard limiter is shown in red, the inboard limiters are shown in blue, and the gap limiter is shown in green. The directions of plasma current and some select physical quantities are also shown. This setup is valid for a standard RFP plasma. In the top-down view, the positive and negative toroidal sense are labeled from the 0-reference point. Similarly, the poloidal reference point of 0 is outboard, and the positive and negative sense are labeled. The 0 toroidal degree mark is located on the poloidal gap.

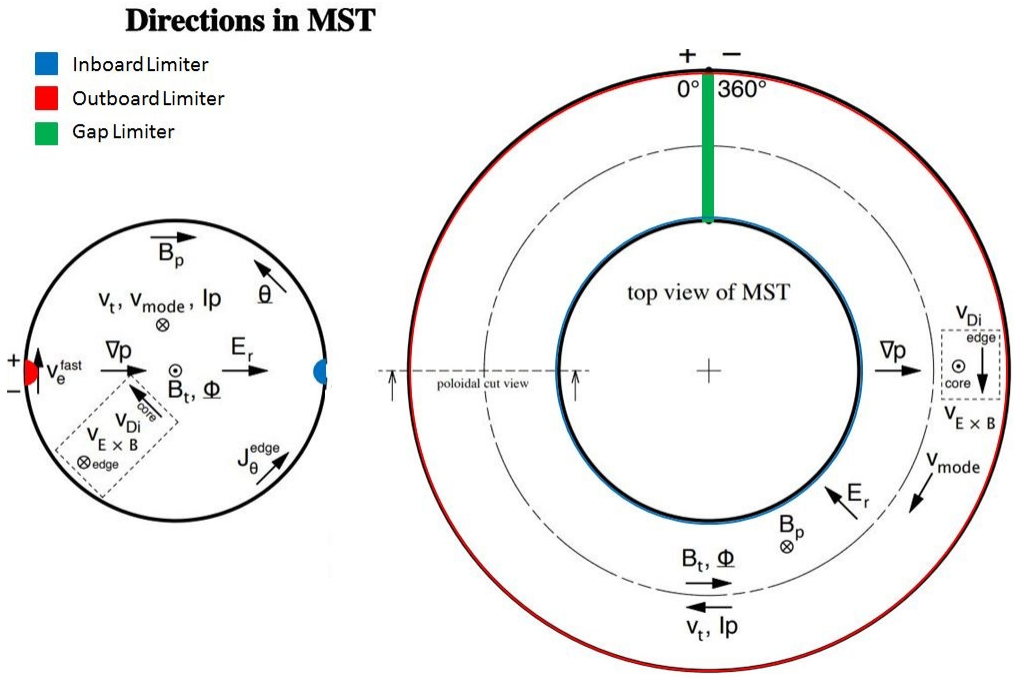

Figure 1.7: MST coordinate system, with limiters labeled in color to orient the reader. Limiters not to scale. Adapted from MST internal reference document 10V01D-A-001.

1.3.1 MST Plasma Facing Components

The MST shell is 5.0 cm thick aluminum and serves three purposes. First and foremost, the aluminum shell is the vacuum vessel for the experiment. Secondly a current is driven through the shell to create the toroidal field. Lastly, currents can form in the conducting shell in response to plasma motion which stabilize external kink mode instabilities. Current is driven through the shell by discharging capacitors to create the toroidal field. The boundary is often treated as an ideally conducting wall, however magnetic error fields exist where diagnostic portholes have been cut out. Current driven through the iron core induces a plasma current, I_p, which in turn creates the confining poloidal field, B_θ. There are a poloidal and a toroidal gap in the MST shell which are required to drive current on a fast time scale. In order to correct for the error fields produced by the gaps in the shell, an active feedback error correction system measures and attempts to minimize the error at the poloidal gap is present on MST. Graphite limiters cover 10% of the vessel wall. The gap limiters, both toroidal and poloidal are composed of graphite half round-tiles with a diameter of 1.27 cm that cover the electrical insulation and vacuum seals. Before beginning this work, a high fraction neutral fraction was believed to be exist in MST, a result of PWI with the limiter. Recycling and wall fueling is operationally used to sustain most discharges after the initial start-up gas injection. MST is fueled by deuterium injected by piezoelectric gas valves [15].

1.3.2 Multi-helicity - The standard RFP

The RFP configuration has lower applied fields, which makes the RFP concept attractive for possible reactor schemes. Lower applied fields can lead to cheaper construction costs, and a more economical fusion power plant or neutron source for industrial applications [26] if the physics issues are solved. Using low toroidal field leads to plasma instability. The safety factor, $q(r)$, is related to the susceptibility of plasma to current-driven instabilities [27]. This factor can be expressed in terms of the chamber geometry and magnetic fields, $q(r) = \frac{rB_\phi}{RB_\theta}$, where r is the radial coordinate, R is the major radius of the device, and B_ϕ and B_θ are the toroidal and poloidal field components at the radial coordinate. The typical q-profile for an MST RFP discharge is shown in Figure 1.8.

Locations in the plasma where q=m/n, where m and n are integers, are called rational surfaces. Magnetic perturbations (modes) can grow on these surfaces. Modes are labeled by the m and n numbers of the surface. The resonance condition for the tearing modes to grow is $\mathbf{k} \cdot \mathbf{B} = 0$. In MST (m,n)=1,n modes grow in amplitude, the lowest n being 5 or 6 depending on the plasma and increasing upward. The surfaces of 1/6, 1/7 and 1/8 are

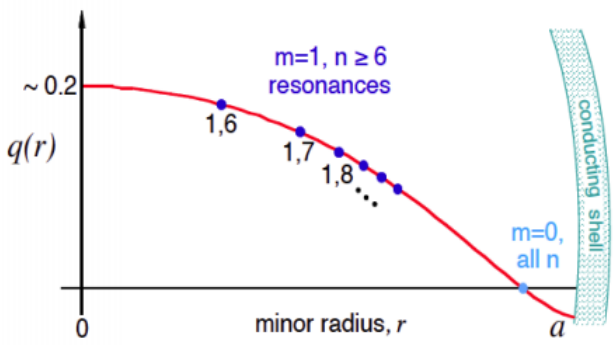

Figure 1.8: A typical MST q-profile with resonance surfaces labeled reproduced from Eilerman's Figure 1.2 [23].

shown in the Figure. Lower n modes are larger in amplitude. On the q=0 surface, denoted as the reversal surface, all m=0 modes can grow. Once mode amplitudes are sufficiently large they begin to overlap. This overlap of magnetic modes forms a stochastic region in the confined plasma. This stochasticity leads to rapid energy transport outward [25].

The standard MST discharge is an RFP discharge with I_p ranging from 200-500 kA and density from 0.5-1.5x$10^{19} m^{-3}$. The density limit in the standard MST RFP follows closely the Greenwald density limit $n_G = \frac{I_p(MA)1x10^{20}}{\pi a^2 m^3}$ [5, 28]. The plasma current can be maintained at the peak value for 20 milliseconds which defines a current "flattop" period. The reversal parameter, $F = \frac{B_t(a)}{\langle B_t \rangle}$ can be varied, typically from 0 to -0.5, but most plasmas are created with F=-0.2. Changing the reversal parameter changes the q-profile of the plasma, as the edge magnetic field is increasingly reversed. The reversal surface, where q=0, is pushed deeper into the plasma. Traces of a standard multi-helicity RFP plasma are shown in Figure 1.9. The plasma current evolution is shown in the upper left of the Figure 1.9 (a). The flattop period exists between 20 and 40 ms. The plasma density measured by a CO_2 interferometer is in the upper right frame of 1.9(b). Density peaks during formation, stabilizes during the flattop, then decreases with plasma current. Sawtooth activity is seen in the trace of F in the lower left of the Figure 1.9 (c). Magnetic activity is shown in the lower right frame of 1.9 (d). All modes are of comparable amplitude in MH plasma. Spikes in the magnetic mode amplitudes are caused by magnetic reconnection. Various MH plasma states and their 0D energy confinement properties are summarized in Table 1.1. Electron temperature and energy confinement times are the flattop values from 120 MSTFit, a Grad Shafranov solver [29] , reconstructions averaged together. The ohmic input power is calculated as $I_p V_{loop}$ from the flattop averaged MST signals.

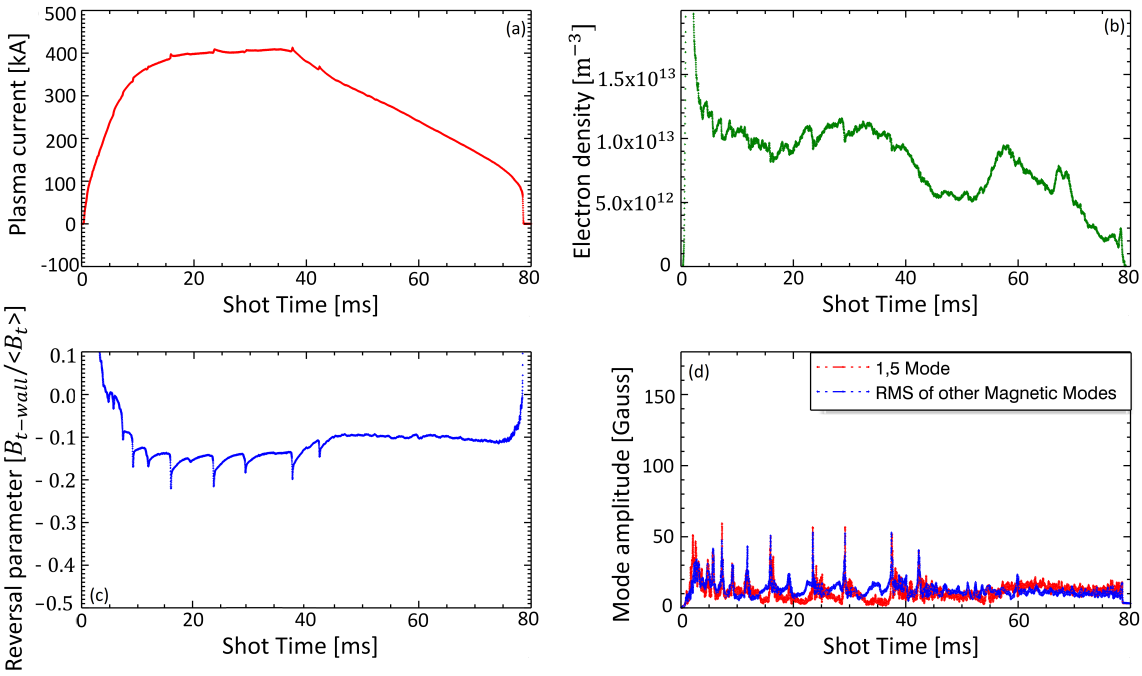

Figure 1.9: Typical 400 kA MH RFP operational time traces. The signals are the plasma current, density, reversal parameter, and magnitude mode amplitudes. Sawtooth behavior is seen in the reversal and magnetic mode trace while the current is peaked. The m/n=1/5 mode is shown in red, and the RMS of the other secondary modes is shown in blue, they are all similar amplitude. Data from MST discharge 1190104010

	T_e[eV]	τ_e [ms]	Ohmic Input Power (MW)
200 kA MH	270 ± 25	1.0 ± 0.3	5.3 ± 0.3
300 kA MH	310 ± 30	1.2 ± 0.4	5.2 ± 0.5
400 kA MH	355 ± 30	1.5 ± 0.6	6.1 ± 0.7
500 kA MH	440 ± 30	1.8 ± 0.8	6.6 ± 2.2

Table 1.1: Standard MH peak electron temperatures and average energy confinement and ohmic input power during the MST flattop period. These terms are calculated by the MSTFit reconstruction code. Confinement increases with plasma current, as well as the energy required to sustain the discharge.

1.3.3 Quasi-single helicity - the helical RFP

One of the recent developments in RFP research has been the identification of a new RFP regime where the plasma spontaneously transitions to a helical state where the innermost tearing mode grows and merges with the equilibrium magnetic axis. Secondary mode

amplitudes drastically decrease, leaving a helical core region with an enhanced transport barrier. The QSH state has been observed in many different RFP devices, such as RFX, EXTRAP T2R, and MST [2]. In RFX particle diffusion has been observed to drop from 50 $\frac{m^2}{s}$ to 1 $\frac{m^2}{s}$, and energy diffusion reported as low as 5 $\frac{m^2}{s}$ [30, 31]. In MST the QSH regime is typically accessed at high plasma current and shallow reversal parameter, F=0 is optimal. In MST it is the m/n=1/5 mode that grows in amplitude to become the helical axis. A sample of QSH plasma parameters is shown in Figure 1.10. In Figure 1.10 (a) is shown the plasma current trace, in Figure 1.10 (b) is shown the plasma density trace, in Figure 1.10 (c) is shown a lack of sawtooth activity, and in Figure 1.10 (d) is shown reduced magnetic activity compared to the MH state. The presence of this regime has been found to scale with the plasma Lundquist number, $\frac{I_p T_e^{3/2}}{n^{-1/2}}$ [1]. MST is operated at high current (400-500 kA) and low density $0.5\text{x}10^{19} m^{-3}$ when QSH plasmas are requested. With the m=0 rational surface outside the plasma (located at the wall), the nonlinear coupling between the tearing modes is significantly reduced. Various QSH plasma states and 0D energy confinement properties are summarized in Table 1.2. These 0-D properties are the output of the V3Fit reconstructions, where the electron temperature is the peak temperature in the reconstruction. The energy confinement time is calculated as the ratio of the stored energy to heating power.

	T_e [eV]	τ_e [ms]	Ohmic Input Power (MW)
400 kA QSH	610 ± 25	4.5 ± 0.4	3.3 ± 0.3
425 kA QSH	630 ± 30	4.8 ± 0.6	3.5 ± 0.4
500 kA QSH	820 ± 50	6.0 ± 1.2	4.1 ± 0.8

Table 1.2: Typical temperature, energy confinement times, and observed ohmic input powers for QSH discharges on MST as computed by V3Fit reconstructions.

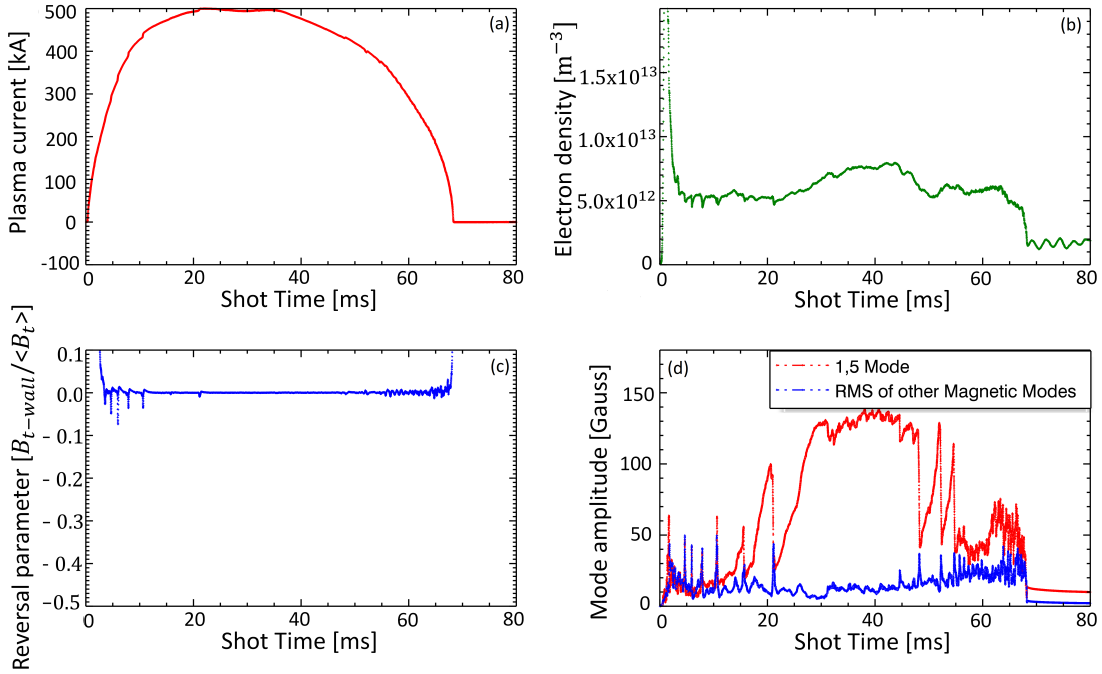

Figure 1.10: QSH 500 kA RFP operational time traces. Signals shown are the plasma current, density, reversal parameter, and magnitude mode amplitudes. No sawtooth behavior is seen in either the reversal trace or magnetics. The core magnetic mode, the 1/5 mode grows to large amplitude at the expense of secondary modes forming the QSH state. Density is around half the value of an MH plasma. Data from MST discharge 1150513006

1.4 An overview of edge physics and phenomena

Confined magnetic plasma is held inside "good flux surfaces". The last closed flux surface (LCFS) is the divider between confined plasma and plasma in the scrape-off layer (SOL). In a limited plasma, the limiter defines the LCFS where the plasma extent is "limited" by the material. Outside the LCFS but before the limiting material surface is known as the scrape-off layer. Because the way the magnetic fields in the SOL are structured the flux surfaces are not closed and field lines intercept limiting surfaces. Various control coils may be present near the edge for plasma control or other uses. In limited geometry, the poloidal or toroidal field lines are designed to intersect the limiter surface [3]. Wherever a material surface exists an electrostatic sheath forms. Electrons travel more rapidly to the walls of the confinement vessel, building up potential on the surface, forming an electrostatic sheath around the plasma. Ions drawn into the electrostatic sheath are commonly assumed to have a velocity equal to the ion sound velocity c_s, this assumption is known as the

Bohm criterion [32]. In RFP configurations with F <0, the edge is everything outside the reversal surface. This configuration for a MH RFP is shown in Figure 1.11. In this figure the outermost boundary in black represents the vessel wall. Moving inward is the blue region of plasma representing the SOL. The SOL is defined as region of plasma in the shadow of the limiter. The limiters are shown in green. The edge plasma of the RFP is then shown in red, between the limiter and the reversal surface (where B_T flips direction inside the plasma). The reversal surface can be moved radially in the plasma by changing the operational settings of the RFP. Everything inside the reversal surface, is the core plasma region.

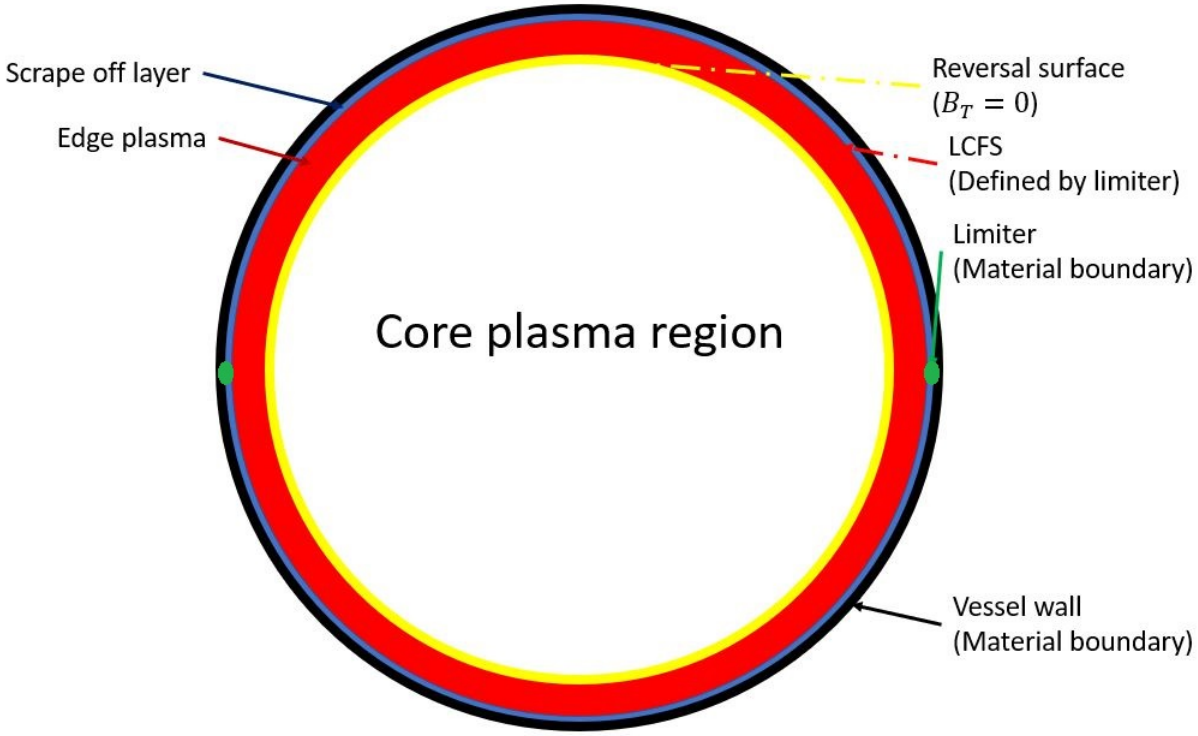

Figure 1.11: A sketch of the regions of a MH RFP plasma with a limiter boundary. Boundaries are labeled on the right side of the figure, and the regions are labeled from the left side.

Large tearing modes cause rapid transport from the core region outward until the reversal surface where large magnetic shear forms a transport barrier. It is common for RFPs to use some form of boundary control. For MST a conducting shell forms a near-ideal boundary where B_r is 0 at the wall. Other machines typically use active feedback correction coils to cancel out B_r in their edge [33, 34]. The close-fitting shell leads to well-structured

magnetic surfaces at the very edge of the plasma [35]. Experiments have shown that the plasma-wall interaction (PWI) greatly depends on the edge magnetic topology. For instance in tokamaks, ELM control [36, 37], density limits [38], improved confinement access [39, 40] and flow control [41], vary as the magnetic structure of the edge is changed with resonant magnetic perturbations.

1.4.1 Impurities

In a idealized plasma confinement system, only the fusing isotopes, namely deuterium (D) and tritium (T) would exist. However such a system is impossible to construct as the act of fusing produces helium which will act as an impurity. Generation of the helium impurity requires a design with particle exhaust in order to remove the helium produce in fusion. The removal of these particles implies a convective energy loss to the system. The removal of the particle and energy from the system could lead to plasma-material interaction with the vacuum vessel, first wall limiters/divertors, and potentially diagnostics. Plasma-material interaction generates impurities which may enter the plasma. Impurities can be both helpful or harmful to the plasma and often in order to be helpful, the system must be engineered to control their abundance and location. Impurity radiation can cause energy losses in the plasma, which increase with the impurity's atomic number. Impurities also may serve as a diagnostic tool in plasma research [42].

Another drawback of impurities is fuel dilution. Total plasma pressure has a limit; the quantity beta represents the ratio of plasma pressure to magnetic pressure $\beta = \frac{nkT}{\frac{B^2}{2\mu_0}}$. In tokamaks and RFPs this limit is the Troyon beta limit $\beta_{max} = \frac{2.8 I_p}{aB}$, I_p is the plasma current in MA, B is the magnetic field, and a is the minor radius of the plasma. The Troyon beta limit seems to be a strict constraint for RFPs only when edge fueling is used, with pellet fueling being able to bypass the limit without adverse effects on the plasma [43]. Impurities released will use up a fraction of the β limit without contributing to fusion.

One effect of impurities is ionization cooling. Here impurity neutrals are ionized by the plasma. Ionization is a sink for the plasma energy balance. Energy must be injected into the plasma system in order to sustain the ionization of neutrals or the plasma will cool off and revert to a neutral gas.

Impurities may also be excited before ionization can occur. The neutral particle can emit tens of photons to de-excite from the collision causing the energy lost by the plasma to be higher than just the energy of ionization. When the ions recombine with electrons, they radiate yet more energy out of the plasma by emitting photons. The recombination rate depending on the temperature and density of the plasma. Radiated photons are detrimental

to the confined plasma as the photons are not confined by magnetic fields and can escape the confinement volume. This radiation effect may also be useful to dissipate heat loads at the limiter or divertor. Plasma particles being exhausted will carry some energy with them to the limiting surfaces. Rather than have large local heat fluxes, the energy can be spread out by injecting a gas and dispersing the heat load by ionization or radiative cooling. This is one example where controlling plasma-neutral interactions is desired [44].

An impurity source is characterized by determining the impurity species, the locations (walls, limiters, probes, portholes, etc.), the absolute magnitudes of fluxes, and the ionization locations. Visible wavelength emission spectroscopy is a common technique to measure impurity influxes used on many magnetic confinement devices. Absolute measurement of photon intensity at various line emission wavelengths can provide information about the influx of particles, $\Gamma = \frac{4\pi I_{ph}}{PE}$ where Γ is a particle flux, I_{ph} is the photon intensity and PE is the photon efficiency, a function of electron density and temperature. The values are determined experimentally utilizing calibration with known sources or calculated with collisional-radiative models (CRMs). If the plasma is strongly ionizing, PE can be simplified to a ratio or excitation cross-sections to ionization cross sections, reducing the complexity to just a function of temperature. A method for converting measured photon fluxes to a particle flux rate is the S/XB method.

$$\Gamma = I_{ph}\frac{S}{XB} \tag{1.8}$$

Here the S/XB coefficient represents the ratio between excitation and ionization, and a branching coefficient that depends on the excited states [45, 46]. The S/XB coefficient effectively is the number of photons emitted per neutral particle until ionization occurs. This method is discussed in more detail in Chapter 2, where it is primarily applied to identify the deuterium recycling source.

1.4.2 Edge transport

Simple 1-D transport models have long been applied to the edge and core regions of RFP plasma devices [3, 8]. Toroidal and poloidal localization of neutral sources and the repeated process of ionization and recombination occur in the edge which often necessitates 2D or 3D treatments for accuracy. Transport in the main plasma that is inside the LCFS can be described by 1-D models [4–6]. Diffusion is the simplest model for plasma transport, $\Gamma_\perp = -D_\perp \frac{dn}{dr} - v_{drift} n$ where $D_\perp$ is a cross-field diffusion coefficient and v_{drift} is a drift velocity. However, determining an accurate value for $D_\perp$ is difficult due to turbulence and transport. Often the diffusion is measured experimentally. Inside the MH RFP transport

is very strong. Sawteeth create a periodic temporal element to the movement of plasma between core and edge regions. $D_\perp$ is often on the order of 0.1-50 $m^2 s^{-1}$ while the drift velocity varies. In MST, the diffusion in MH plasmas tends to be closer to the 50 $\frac{m^2}{s}$ value. Both quantities may vary with the plasma radial coordinate. Notably the particle transport shifts from electromagnetic driven to electrostatic driven at around r/a=0.9 in MH RFP plasmas [47].

Complete analysis will include transport from source to sink of the quantity of interest, such as density or energy. Typically transport of density is by convection, or turbulence, with the particles being treated as a fluid. Energy transport includes convection, conduction, and radiative transport, with the potential for turbulence aiding the convection. In a plasma, gradients in the temperature and density profile drive heat conduction. Heat convection occurs as the particles that carry energy move within the plasma. Radiation occurs through atomic processes, when electrons recombine with atoms, or in the aftermath of a collision with a neutral particle, as the neutral looses energy by radiative decay. These emitted photons then carry off energy. Moreover, when collisional processes are considered, there is the option for a neutral to collide with the hot plasma, charge exchange, and then for the previous hot ion, now hot neutral, to fly out of the plasma removing energy.

1.5 Thesis overview and structure

The transition of the RFP from an asymmetric to a 3D helical structure dramatically changes the edge structure of the RFP. Dedicated experiments on MST investigated the influence of the magnetic structure of the RFP plasma on fuel recycling and PWI. The plasma-wall interaction and recycling flux changes from the axisymmetric to helical state, both becoming increasingly localized, and increasing in magnitude, despite lower density plasma being utilized to form the QSH state.

In order to accurately model the neutral density profile and the interaction of the plasma and neutrals in MST, experimental data was collected by edge probes and other existing diagnostics to form the plasma background in the EIRENE simulations. The reaction rate of plasma-neutral interactions depends strongly on the plasma parameters and requires accurate knowledge of local plasma conditions. Camera observations of MST obtained direct measurement of D_α light. This light is used to reconstruct, through the before mentioned atomic processes, measurements of recycling flux. Recycling flux is the neutral source in MST. Experimentally informed EIRENE models calculate the plasma-neutral interactions for various MST configurations. The results highlight differences between the standard RFP configuration and the helical, QSH state. The RFP energy balance is yet to be

fully understood; this work addresses the role neutral particles play in that energy balance, acting as an energy sink for the plasma.

New camera diagnostics were prototyped and integrated into MST as part of this work. The diagnostics and codes used in this work along with the details of the analytical techniques are described in Chapter 2. The details of the synthetic image routine developed for EIRENE and the general workings of the EIRENE code are also presented in Chapter 2. The details and analysis of probe and bolometer experiments on the MST edge are presented in Chapter 3. Magnetic array measurements identify the plasma state as either an MH or QSH plasma. Boundary viewing cameras measure the neutral sources by observing the D_α photon flux. Conversion of the photon flux into the neutral flux requires accurate knowledge of the local plasma parameters. The modeling efforts utilizing EIRENE and including the techniques of tuning the model recycling and source distributions to obtain strong agreement to synthetic diagnostics, along with the full 3D neutral profiles are presented in the first half of Chapter 4. The power losses of the plasma due to plasma-neutral interactions is presented in the second half of Chapter 4.

Chapter 2

Experimental design and diagnostics details

In this Chapter the experimental framework of the thesis is established. First, the overall theory of edge measurements and modeling are discussed. Next, the diagnostic tools, including the details of the boundary viewing cameras, are reviewed. The methods of analyzing experimental data are then presented. Lastly, a review of the computational tools is presented.

In order to build a particle or energy balance for MST, neutral sources must be identified. MST is fueled by gas injection and sustained by neutral particle recycling. There is a small chance for the injected fuel particles to ballistically bounce back from the wall in direct recycling. More likely the particle will adsorb or embed itself in the material. Once the material is saturated, incident particles collide with the wall and in the process release saturated atoms and molecules from the surface. These neutrals enter the plasma edge; they may scatter with plasma, become ionized, or charge exchange with the plasma. Wall fueling is the ability of plasma to fuel itself from particles released from plasma-material interactions. This transport is often complex even in simple geometries, necessitating the EIRENE modeling. Lower energy electrons impacting neutral molecules may not have sufficient energy to dissociate them but can still vibrationally excite the molecule. Transport and collision physics is a complicated process that involves the molecular dissociation, charge exchange acceleration, and ionization or excitation of multiple species in a plasma. It is a rate-kinetic problem that necessitates a modeling solution.

A generalization of the cyclical transport processes is shown visually in Figure 2.1 [48]. Beginning on the left of the Figure, a neutral particle recycling flux (Γ), is the neutral particle flux released from the material surface by ions through the process of recycling. This neutral flux can be atoms or molecules knocked off the surface by the incident plasma flux, or neutralized and reflected plasma directly. It is usually the case that an incident plasma ion will knock off molecular deuterium from the saturated surface, and implant itself in the material, rather than be reflected. Graphite, the material of the limiter in MST,

emits a neutral flux that is 90% molecular deuterium and 10% atomic deuterium when bombarded by a plasma flux and the temperature of the tile is less than 900K. The 10% deuterium atomic flux represents the direct reflection of the plasma from a collision with the material. The 90% atomic flux arises from plasma knocking off molecules formed on the surface [49]. This mix of atoms and molecules released from the graphite limiter makes up the wall fueling. The molecular deuterium then can be transported as a molecule or dissociate. The atomic deuterium can transport into the plasma until ionized or charge exchanged. The dissociation of excited molecules can produce Franck-Condon neutrals; these higher energy neutrals penetrate deeper into the plasma [50]. Repeated charge exchange losses can cause a neutral particle to accelerate into the plasma. The energy of a neutral tends to increase as it penetrates the plasma. After each charge exchange, the neutral acquires the local ion energy, which tends to increases as the particle moves from the edge to the core.

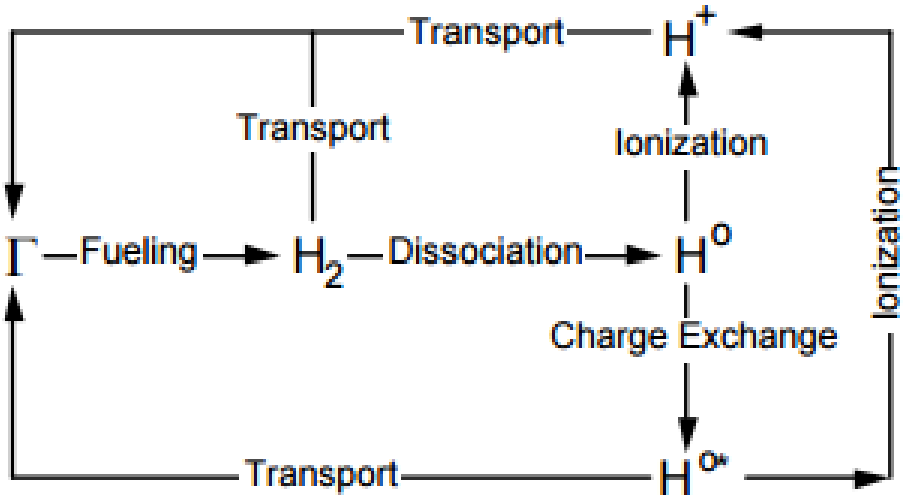

Figure 2.1: Generalized neutral particle life cycle. Neutrals are injected as fuel or recycled, and can dissociate, ionize, charge exchange and transport in the plasma before recycling or being removed. Reproduced from Lanier's Figure 3.1 [48].

2.1 Modeling of the MST edge and experimental design

2.1.1 Quantities of interest

In MST, many diagnostics are available for use, enabling the plasma to be thoroughly analyzed. The primary diagnostic in this thesis is the newly built boundary viewing camera system [51]. These cameras were developed to measure the PWI at the edge of MST. In addition to the camera system, other diagnostics already in use on MST were utilized to provide additional data to support modeling efforts.

The plasma density is a drive for recycling. The recycling flux is proportional to the ion flux on the walls and limiters,

$$\Gamma_R = R * \Gamma_{ion} \tag{2.1}$$

where the recycling flux of neutrals Γ_R, is equal to the incoming ion flux, Γ_{ion} times some coefficient R. This recycling coefficient is typically near unity.

R=1 does not imply that the ions are bouncing back off the walls as neutrals. What is occurring instead is that ions impacting are absorbed into the wall material. These impacts provide energy which allows molecular desorption of neutralized deuterium from the wall[49]. During MST operations at low current, recycling is able to sustain plasma density. When MST is operated at higher currents (400 kA+), additional external fueling by gas injection during the discharge is often required. This fueling during the discharge introduces additional sources of neutrals to the plasma and additional asymmetry to the shot. Accurate, neutral particle measurements will allow for better estimates of energy radiating out of the plasma from plasma-neutral collisions and charge exchange; and is the primary goal of this work.

In addition to direct probing of the MST edge, laser interferometry and Thomson scattering collect data over a set of chords in the plasma. The far infrared laser interferometer collects density measurements out to r/a=0.83. This data contributes to MSTFit and V3Fit reconstructions. Lastly, the MST bolometers are utilized to obtain wall neutral power fluxes.

The list below summarizes what physical quantities are either measured or modeled in this work.

1. T_e, n_e, T_i - basic edge plasma properties
2. P_{rad}, P_{CX} - power removed from the plasma by neutral interactions
3. Γ_i - plasma particle fluxes
4. Γ_{Rec} - recycling fluxes

The plasma properties T_e and n_e are measured directly in the plasma edge by triple tip Langmuir probes [52]. These values are important for both understanding the plasma edge structure and in modeling the reaction rates of plasma-neutral interaction. Laser interferometry is used to obtain n_e and Thomson scattering is used to obtain T_e in the plasma core region. P_{rad} and P_{CX} are measured with bolometers and modeled in EIRENE. These terms generally represent the losses from electron-neutral and ion-neutral interactions in the plasma. The ions Γ_i and neutrals Γ_{Rec} represent the flux of plasma onto the material surface and the flux of neutrals returning from the material surface. The ratio of these two fluxes can be used to identify recycling. Γ_{Rec} is the neutral particle source in the system, which must be known for EIRENE modeling.

2.1.2 Experimental design and workflow

The rest of the Chapter discusses each diagnostic or modeling tool used in detail. The workflow of the combind experimental and modeling work is shown in Figure 2.2. First measurements of the MST edge are obtained experimentally. These include images (Γ_{Rec}), measurements of the plasma (T_e, n_e), and line integrated optical measurements. These measurements form a plasma background and neutral source constructed in EIRENE. EIRENE models the plasma-neutral interactions and synthetic diagnostic signals , producing both images and line integrated signals. Synthetic signals are compared with both experimental images and experimental D_α signals. EIRENE calculates the P_{rad} and P_{CX} measured by synthetic diagnostics which can be compared to the experimental measurements.

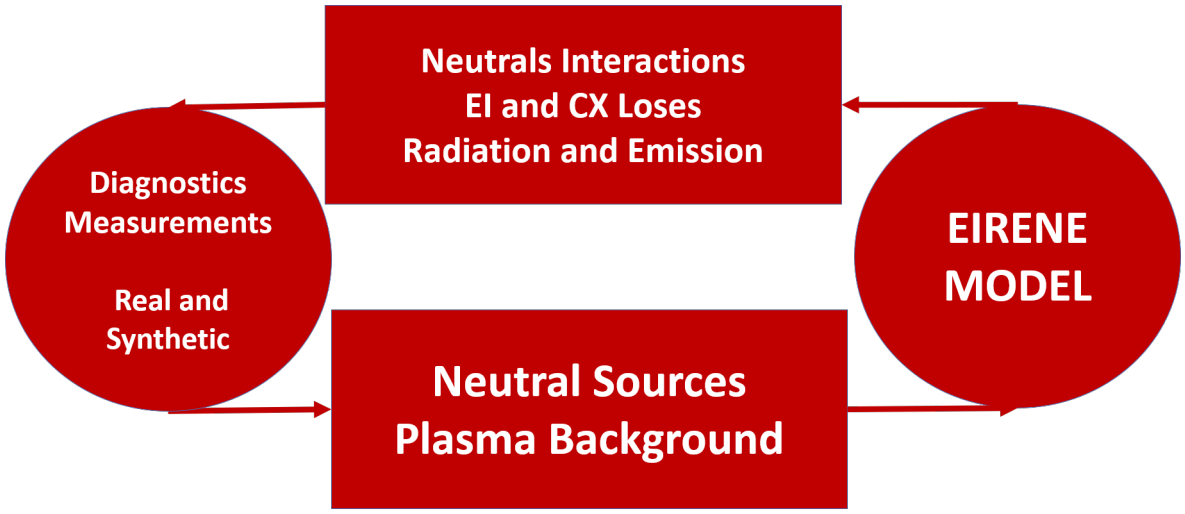

Figure 2.2: This diagram outlines the scheme used to couple experimental measurements and modeling work. The process begins with experimental measurements of the edge and images of PWI. Neutral sources are constructed from images and reconstructions of the plasma background from diagnostics are formed. EIRENE computes the plasma-neutral losses as well as produces synthetic diagnostic signals, including images. Images are compared with the experimentally measured data.

An approach to globally assess the balance between fueling particles, exhaust and the plasma particles is a single reservoir particle balance. A single or multiple reservoir model characterizes the basic particle balance in the plasma edge [53, 54]. The single reservoir model is shown in Eqn. 2.2, where N_{tot} is the total number of particles, τ_p is the particle confinement time, f_{rec} is the recycling efficiency, f_{gas} is the fueling efficiency for external sources, Φ_{rec} is the recycled neutral particle flux, Φ_{gas} is the external gas source, and Φ_{wall} and f_{wall} are the wall fueling rate and efficiency.

$$\frac{dN_{tot}}{dt} = -\frac{N_{tot}}{\tau_p} + f_{rec}\Phi_{rec} + f_{wall}\Phi_{wall} + f_{gas}\Phi_{gas} \tag{2.2}$$

This single reservoir model is applied to MST. The magnitude and fueling efficiency of the wall fueling is deduced from gas injection experiments and simulations. The model has been shown to describe plasma in near steady-state conditions [55–58]. This equation is solved as a 1st order differential equation, and the characteristic time scale of the solution is τ_p. Included in the model are the associated fueling efficiencies for each possible neutral source term relative to the plasma configuration. Each fueling efficiency can be represented as a fraction of the neutral source that is ionized, S_{ion}, relative to the total neutral source

S_{neut}:

$$f_{eff} = \frac{S_{ion}}{S_{neut}} \tag{2.3}$$

The ionization rate $\langle \sigma_{iz} \rangle$ will depend on the local plasma temperature, and density. This changes with plasma configuration and radius. These fueling efficiencies are experimentally measured by injecting a known amount of gas into the plasma, as well as modeled in EIRENE for QSH configurations. N_{tot} is calculated as the product of the line averaged density, n_e, and the MST confinement volume, V_{conf}. MST, with its major radius of 1.5m and minor radius 0.52 m, has a confinement volume of $8m^3$ [15]. The presence of the limiter decreases V_{conf} to $7.61m^3$.

Experiments are performed over a variety of plasma conditions to obtain the effects of controllable parameters on the plasma-wall interaction and the plasma-neutral interactions. The two main control knobs in the experiment are the plasma current and density. Changing the current and density in the experiment drives the plasma configuration from MH to QSH. Experiments are conducted by varying I_p in both the MH and QSH states.

2.1.3 Measurement of the effective particle confinement time

The MST gas fueling system was used in experiments to determine the effective particle confinement time. Effective particle confinement time, τ_p^*, is a measurement of the total particle confinement including the increase of particle lifetime from recycling [59].

$$\tau_p^* = \frac{\tau_p}{1 - R} \tag{2.4}$$

By injecting a known amount of gas into the system, two quantities can be calculated. The fueling efficiency is the ratio of gas ionized in the plasma to the amount of gas injected. Fueling efficiency is calculated by integrating the density rise during the time immediately following the gas injection, shown in Figure 2.3. The time trace of line averaged density throughout the shot is shown in the top frame. The gas injection during the shot is shown in the next frame. Gas injected after 50 ms is not part of the experiment but used to soften MST discharge termination. The results of the fitting routine are shown in the bottom frame. The peak density is identified at just after 30ms. A fitting routine is applied to determine exponential decay of the density between peak time and the time when the density reaches the pre-injection average value. An integration region is determined by computing density rise from the start of gas injection to where it returns to the pre-gas injection level. The total density rise is compared to the amount of fuel injected into the system, and f_{eff} is computed. The peak density magnitude and time are identified.

An exponential decay curve is fit from the density peak to the point where the density returns to baseline, and from that, the value of τ_p^* obtained. The general form of the fit is:

$$Y = A_2 + A_0 * exp(A_1 * X) \tag{2.5}$$

The A_1, A_2, A_3 coefficients are calculated with the IDL routine CURVEFIT. The initial guess values for the A_0, A_2 are the density peak value. The initial value for A_1 is 0.1. The exponential coefficient is used to calculate τ_p^* as $A_1 = \frac{1}{\tau_p^*}$.

The particle confinement time unadjusted by recycling, τ_p, is also obtainable by knowledge of the source and loss rates of the particles. This is only possible in a model where the source rate and loss rates are exactly known. τ_p defined this way is shown below as a ratio of the volume to loss terms:

$$\tau_p = \frac{\int n_p \, dV}{\int (S_p - \frac{dn_p}{dt}) dV} \tag{2.6}$$

where S_p is the source of all particles in the system and n_p is the particle density. The particle density can be any plasma species; electron, primary ion, or impurity ion. The source of electrons and ions is the ionization of neutrals. The neutrals are sourced by

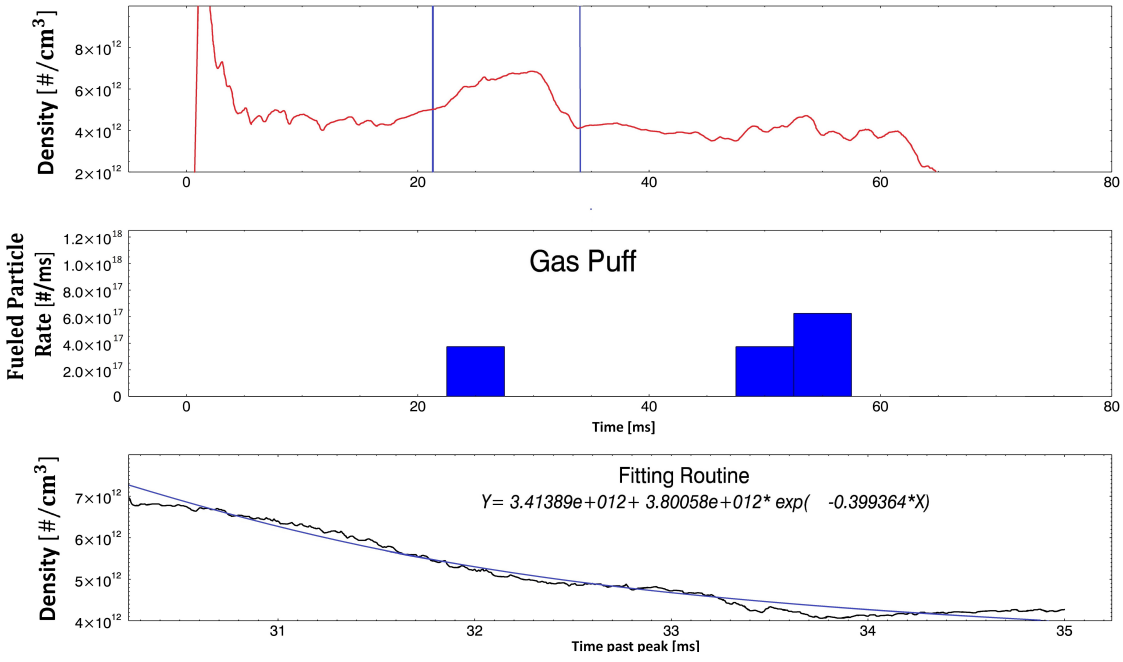

Figure 2.3: Sample discharge showing the region of curve fitting to the density trace during gas injection experiments. A sample fit is shown. τ_p^* is by definition the inverse of the exponential fit coefficient.

gas injection, recycling, and wall fueling, known quantities in a model. Recycling is the dominant source. If the density is constant, $dn/dt = 0$, then the loss of electron or ion density to the walls is balanced exactly by the ionization rate:

$$S_p - \frac{dn}{dt} = S_{ionization} \tag{2.7}$$

In a steady state system, the τ_p is the ratio of the stored density to the ionization rate integrated over the system volume. In a model, such as EIRENE, the particle confinement can be computed as the ratio of the volume integrated density of the plasma background compared to the ionization source calculated by EIRENE as the neutrals transport in the plasma.

2.1.4 Neutral density

As part of the attempt to identify neutral particles as an exhaust and fueling pathway, the neutral density n_N must be known. The neutral particle density can be calculated from measurement of D_α emission and the known electron density. The source rate of photons is related to the particle densities by:

$$S(r) = n_e(r) n_N(r) \langle \sigma v \rangle_{ionization}(T_e) \tag{2.8}$$

with $S(r)$ being the ionization rate of neutrals, $\langle \sigma v \rangle_{ionization}$ the ionization rate coefficient, and n_N is the neutral density [3].

2.2 Diagnostic tools and analysis methods

2.2.1 MST magnetics array

This work quantifies the differences in neutral particle sources and sinks measured in the QSH and MH (standard) RFP. The first diagnostic reviewed is the MST magnetic array. The magnetic signals collected by the array are used to identify these two modes of operation. The magnetic array is composed of 32 poloidal and 32 radial magnetic pickup coils on the interior of the poloidal gap. These coils monitor equilibrium and fluctuating magnetic field quantities. In addition, a toroidal array on the lower inboard side of the machine has 64 coil stations, each with a (B_r, B_ϕ, B_θ) measurement. Signals are decomposed into Fourier harmonics. Poloidal mode (m) and toroidal mode (n) numbers can be picked out of the processed data. Data provided by the array include mode amplitudes, phases, and velocities. The strength and phase of the harmonics are used to determine the state

of the plasma. Having only one poloidally located array formally only allows toroidal mode numbers to be identified. The assumption is made in MST that the poloidal mode number is a function of toroidal number based on the resonance of the modes or m=m(n). The resonance of magnetic modes in MST is given by $\frac{m}{n} = -\frac{rB_\Phi}{R_0 B_\theta}$ [60]. The QSH plasma studied in MST is defined by a m/n=1/5 mode. Mode amplitudes for various MST plasmas are plotted in Figure 2.4; a case for standard MH magnetics and two enhanced confinement modes of operation, QSH and PPCD are shown. In the standard spectrum, all modes are of comparable size; this leads to a stochastic core plasma in which there is rapid transport between the core and edge. Control of the modes leads to improved confinement. The first method of doing so was the transient PPCD. In PPCD all mode amplitudes are strongly suppressed, the electron temperature triples, and plasma beta doubles for a brief time [61]. The PPCD period is labeled in the Figure, it can be seen that magnetic activity is greatly reduced in this period. The other enhanced confinement path, QSH consists in MST of the $\frac{m}{n} = \frac{1}{5}$ mode growing at the expense of the other modes as seen in the Figure from 0.025 seconds to 0.04 seconds. The global energy confinement in the QSH case can be up to 1.5 times larger than in the MH case [19].

The quality of the QSH mode is defined as a ratio of the 1/5 amplitude to the rms value of secondary mode amplitude.

$$Q = b_{\theta,(1,5)} / \sqrt{1/n * \sum_{n \neq 5} (b^2_{\theta,(1,n)})} \tag{2.9}$$

Shots with at least Q=8 qualify as QSH. Occasionally the QSH mode will dither back to the MH state, and then recover back into QSH. This back transition must occupy less than 10% of the current flattop period, otherwise the shot will not be classified as QSH. Another metric for the strength of the QSH is the spectral index N_s:

$$N_s = [\sum_n b^2_{\theta,(1,n)} / \sum_{n=5}^{14} b^2_{\theta,(1,n)}]^{-1} \tag{2.10}$$

where b_θ is the poloidal magnitude of the m/n=1/n mode and N_s is a spectral index indicating the concentration of the mode magnetic energy. A pure single helical axis would have $N_s = 1$ [62]. The QSH quality of 8, corresponds approximately to a N_s less than 1.5. The QSH discharge presented in Figure 2.4 qualifies for a sufficient QSH during the period between 35.6 ms and 39.8 ms.

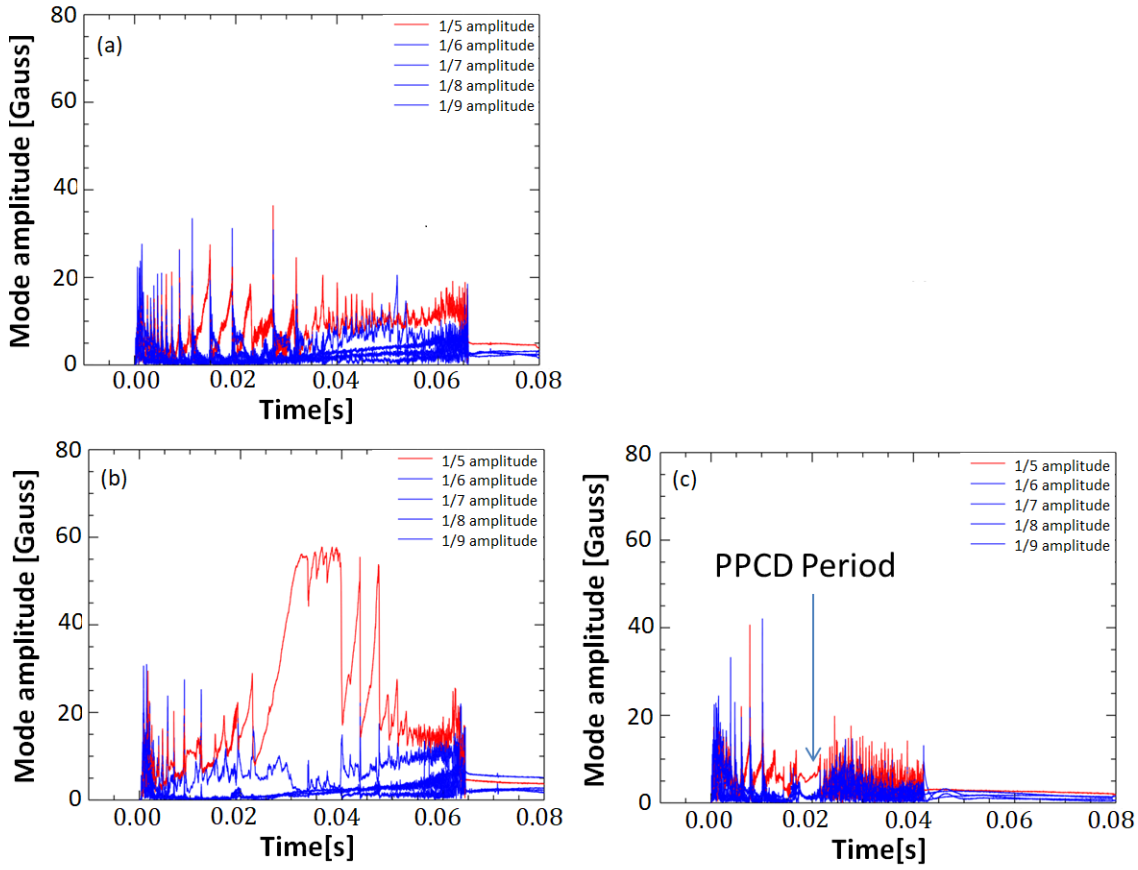

Figure 2.4: Comparison of the magnetic signature of the various MST discharges. Shown in (a) is the standard MH spectrum, (b) is a QSH discharge with a single large mode and (c) is a PPCD discharge with all modes reduced, for a temporary time. In red is the m/n=1/5 mode amplitude. This mode is highlighted as it is a mode that forms the helical axis in MST's QSH. The m/n=1/5 mode mode has no distinguishing features when MST is operated as a MH RFP. When MST is operated as a QSH discharge, the m/n=1/5 mode grows while other magnetic modes shrink.

2.2.2 MST active feedback system

A resonant magnetic perturbation (RMP) can be applied by the active feedback system of MST to lock the shot-to-shot orientation of the QSH mode. The active feedback system consists of 32 sense coils used to measure the local magnetic field and 38 saddle coils, which are used to minimize the radial field at the poloidal gap. A sketch of the active feedback system is shown in Figure 2.5. However, saddle coils can also be used to produce resonant magnetic perturbations.

One interesting application of RMPs is controlling the dynamics of the tearing modes,

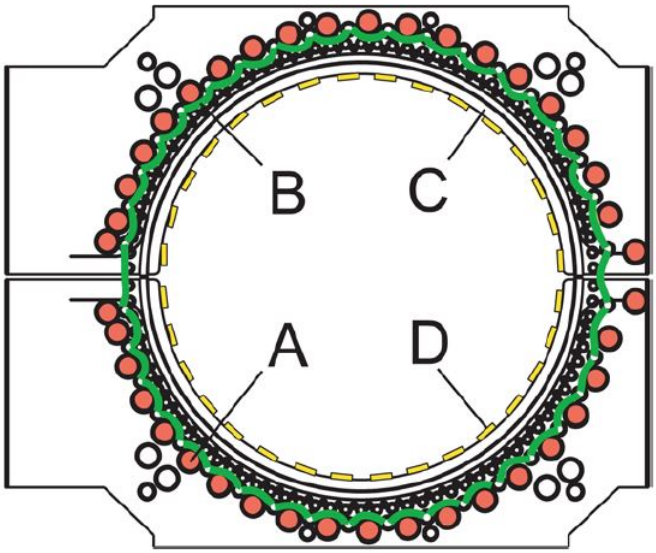

Figure 2.5: Cross section of MST's poloidal gap. The outboard side is on the right. Primary copper winding in red (A), 30-turn saddle coils in green (B), the vacuum vessel (C), and lastly in-vacuum sense coils (D).

particularly plasma rotation and locking. Control of QSH shots has been shown to be possible with the active feedback system on MST. This system is used to lock the QSH state to a prescribed poloidal phase at the gap. The feedback coils generate an electromagnetic torque of $T_{em} \propto j_{eddy} \times b_{mode}$, where j_{eddy} is the current driven in the active feedback system and b_{mode} is the magnetic mode amplitude. The system, being toroidally localized, controls the orientation of the poloidal phase of the $1/5$ mode. A full poloidal rotation of the mode as controlled by the active feedback would cover one of the five toroidal periods. The ability to lock at a prescribed phase is robust. A set of discharges for which the locking angle was scanned over is shown in Figure 2.6. Phase lock can be reliably achieved at any demanded angle.

A sample locked discharge is shown in Figure 2.7. The magnetic mode phase is shown in degrees on the top plot. RMP amplitudes are shown in the next plot. The main RMP is applied from t=16 to t=20 ms. For some phases locking would be difficult as the mode would drift. This can be combated by extending the lock at significantly lower amplitude for 4 ms longer, as seen in the step down of the RMP amplitude from t=20 to t=24 ms. The plasma current and magnetic modes are shown in the next two sub-plots. The QSH mode stays locked in position without RMP though the flattop period. When current decreases the QSH mode weakens and unlocks. The active feedback system and the mechanism of

locking the plasma are described in [24]. The lock angle sent to the RMP system is

$$LA = 241 + (\phi * 5 + \theta) \tag{2.11}$$

where LA is the lock angle request by the RMP system, 241 is a refrence angle of the magnetic array, and ϕ and θ are the wall coordinates of the diagnostic to which the lock is desired. The system is able to lock the QSH state to the location of any diagnostic on MST.

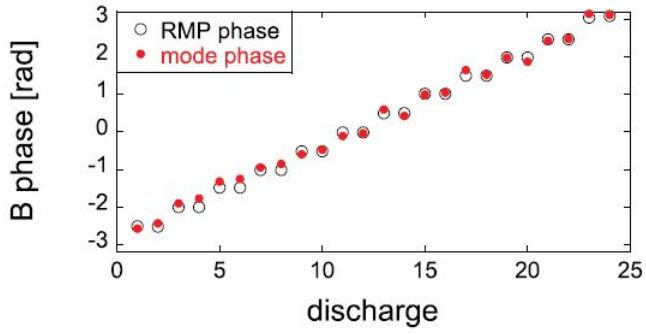

Figure 2.6: The plasma response to RMP phase scan, showing reproducible locking, and ability to lock plasma to any demanded phase.

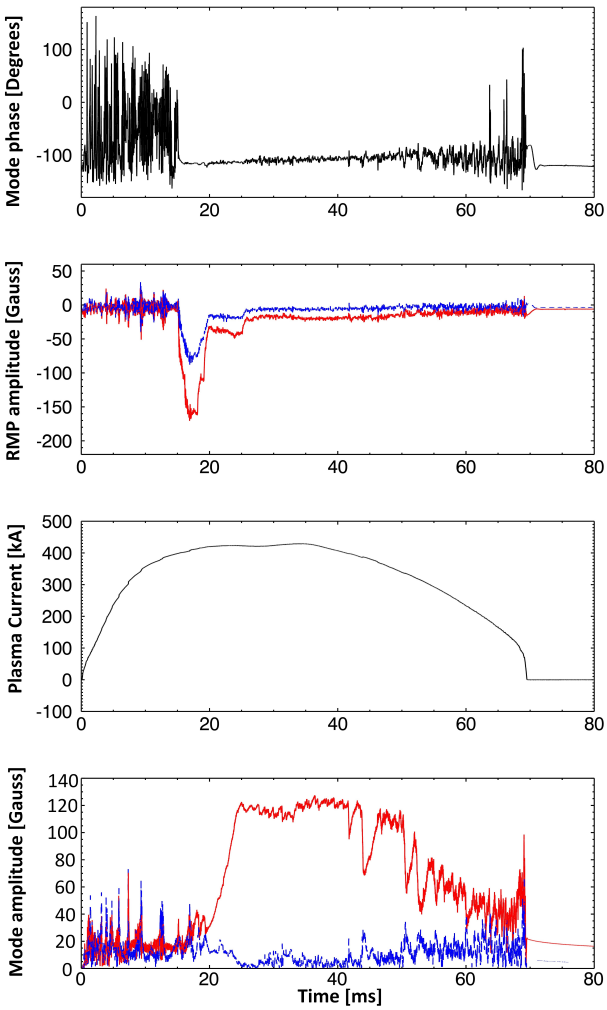

Figure 2.7: Time evolution of MST discharge 118050955, (a) the phase of the 1/5 mode, (b) the drive current for the RMP perturbation (red/solid the sine, and blue/dashed the cosine component), (c) the plasma current, (d) the magnetic mode amplitudes (red/solid the 1/5, and blue/dashed the average of the next five highest mode amplitude. The QSH phase is locked once the RMP turns on, the phase remains locked even as the plasma current decays and the QSH begins to transition back to MH.

2.2.3 Visible imaging spectroscopy of the plasma boundary

The MST boundary-viewing cameras (BVC) are a new diagnostic developed in this thesis work. Currently, nine cameras and associated optics are installed on MST. The purpose of this diagnostic was to provide views of the edge plasma and the MST walls. The camera system was designed to collect light from the visible spectrum.

Various filters are added to allow light from a single emission line to be collected. This is typically D_α light. The camera system, which consists of Dalsa HM640 CCD cameras, has a

high spatial resolution and adequate temporal resolution. The optomechanical diagrams for the diagnostic are shown in Figures 2.8 and 2.9. The optical design is shown in Figure 2.8. A set of rays are traced from the interior of MST to an image plane outside the vacuum vessel. Light is first passed through a Pyrex window, the plasma-facing component. This Pyrex is easily replaced during vents of MST. This window is slightly recessed into the MST wall, and the transmission through it decays slowly as sputtered material accumulates on the window. After a 6-month exposure in the machine, the prototype Pyrex lens transmission decayed to 96% of the clean lens value. The rest of the optical elements transport light through the 5 cm thick shell of MST and focus it onto an image plane. The optics which transfer light from inside the shell to outside the shell create a focal plane. The flexible design of the light collection allows for other collection methods to be used in the future, such as fiber bundles and faster cameras. The mechanical design and assembly of the BVC system are shown in Figure 2.9. A two-axis optical stage (8) is mounted between the camera (14) and the G10 support element (7). G10 is the support element that connects the camera side and port plug side. This provides electrical isolation. MST is independently grounded from the building ground that the back-end electronics were connected to. An aluminum element (8) acts as a spacer and heat sink for the camera. The vacuum seal is made both on the interior and exterior of the port plug by Viton O-rings. The interior seal is between the Pyrex lens and the aluminum tube, where the exterior seal is between the tube and the drilled-out MST shell. The remaining elements are the optical lens and holders.

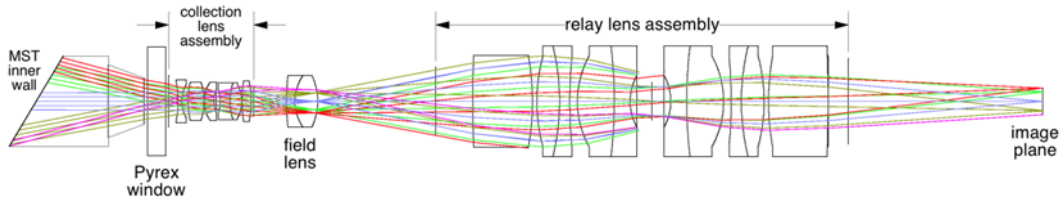

Figure 2.8: Boundary camera optical design produced in Zeemax, showing the collection of light from inside and the transfer to an image plane outside the machine.

The typical operating frame rate is 300 frames per second (fps) at full resolution. The fastest frame rate possible by the camera is 1000 fps, at a reduced resolution of no more than 120 vertical lines. Full resolution for the camera is 640x480 pixels. When viewing the MST interior, this resolution is about 1 mm^2 per pixel in real space, which varies depending on the camera view. The CCD chip has controllable exposure timing. The minimum exposure time is 10 μs, the maximum is limited by the frame-rate. A sample image is shown below in

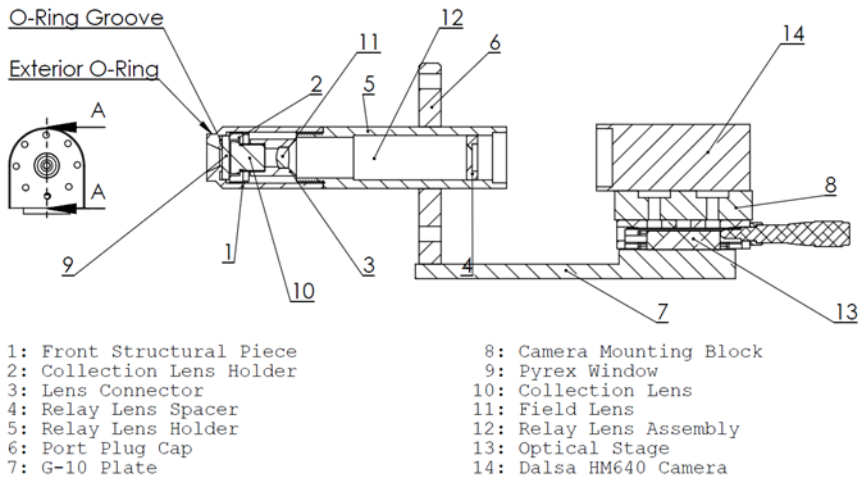

Figure 2.9: Boundary camera mechanical design. Key design features include a G10 electrical isolation plate from the MST shell, and a movable optical stage with which to adjust the focus of the camera.

Figure 2.10. In this image, the graphite tiles of the poloidal gap limiter are visible. The light sensitivity curve for the camera system is shown in Figure 2.11. The camera's sensitivity varies about 20% over the visible spectra, with the peak sensitivity at 680 nm. The camera sensitivity falls off as the light shifts into the infrared.

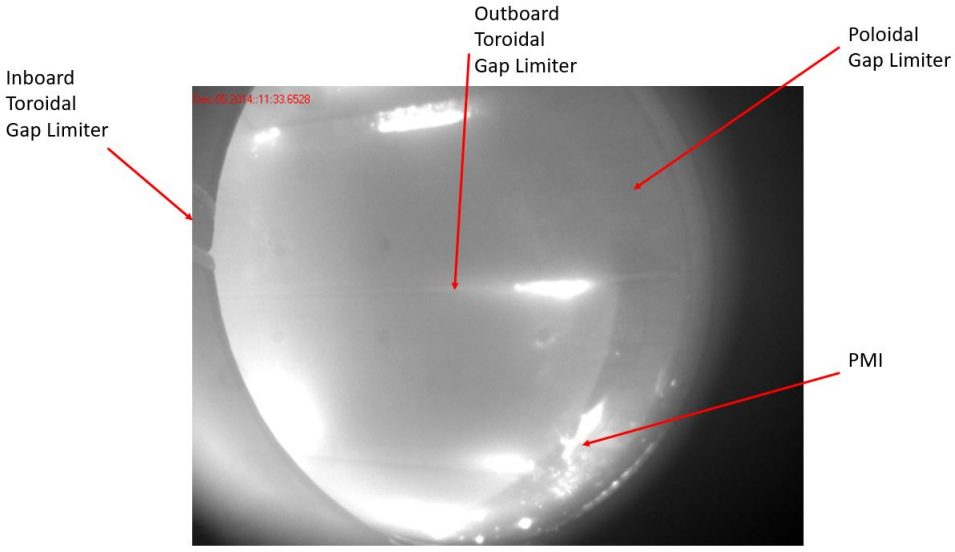

Figure 2.10: Boundary camera sample image from camera nine, looking across the poloidal gap. The image is unfiltered. Image exposure for 100 μs during plasma start-up.

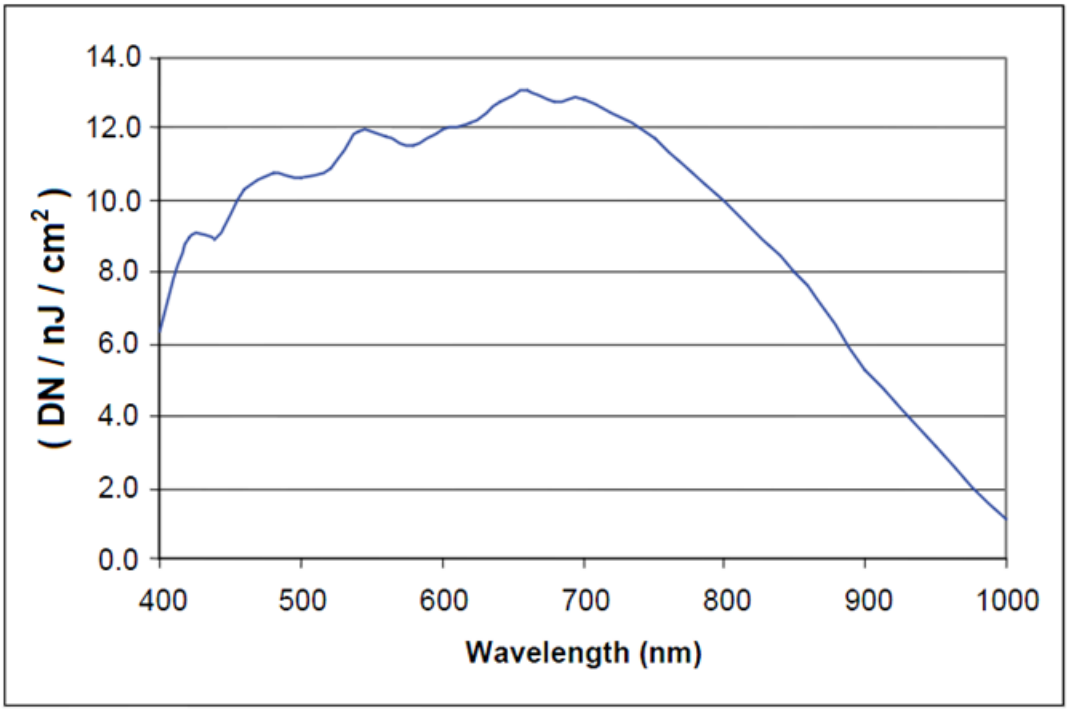

Figure 2.11: The response curve for the cameras used in the boundary viewing system. The efficiency of the CCD chips peaks in the visible range and trails off in both the UV and the IR spectrum.

The BVCs could also be used as an impurity monitoring system. Bandpass filters are mounted in the gap between the CCD chip of the camera and the exit of the optical port. Most of the available filters are narrow bandpass filters with full-width at half-max (FWHM) in the range of 2-7 nm. Each filter passes a single line of interest. Bandpass filters can be added in front of the cameras to measure the emission from impurity species. The transmission curve of the filters used is shown in Figure 2.12. The transmission curves used in the filter survey are overlaid on the Figure as Gaussians defined by the mean and FWHM of each filter. The light that potential impurities and deuterium species could emit is plotted as vertical lines. The color on the Figure represents the wavelength of the light.

The lines searched for are the Balmer series deuterium lines, 656.1 (D_α), 486.0 (D_β), and 443.9 nm (D_γ). Additional bandpass filters were used to survey the rest of the visible spectrum for possible impurity light emission. For example, the C-I line at 601.0 nm, has a high relative intensity compared to other adjacent lines. This relative intensity is used to identify potential impurity species based on the NIST Atomic Spectra Database [63]. Potential lines for the filters used are shown in Figures 2.12. The transmission curves plotted are based on the peak transmission, central location, and FWHM of the bandpass

filters. The effective transmission is easy calculated as the interception of the transmission curve and the line location, for example, the D_α bandpass filters used in the identification of the neutral source transmits the line at 26.6%. Images taken with bandpass filters need to be corrected for the transmission. This is done by dividing by the transmission level of the filter at a given line location.

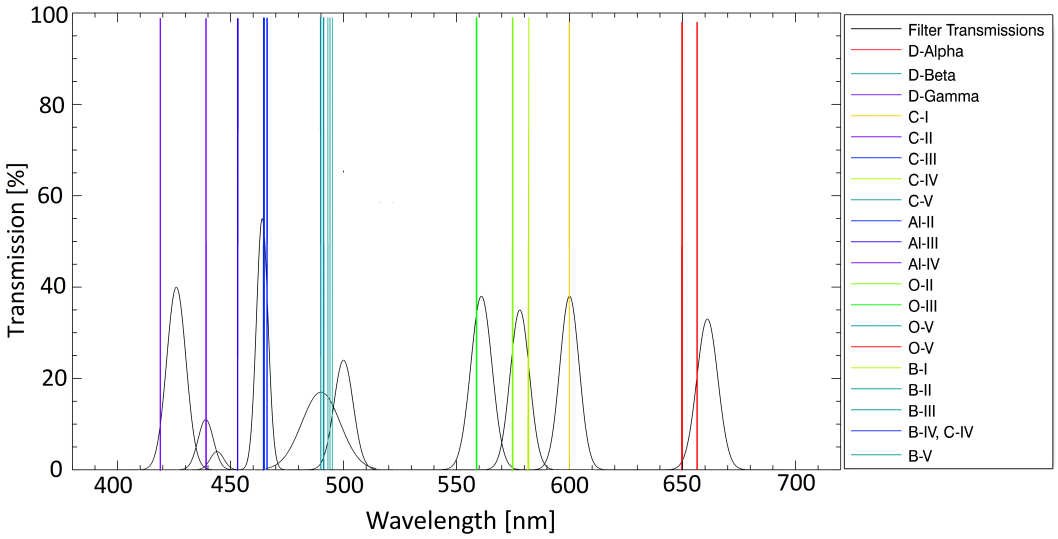

Figure 2.12: Bandpass filter curves and impurity line radiation locations. The impurities shown are those of major concern in MST. Boron from probe housing, carbon and aluminum from the vessel wall and limiters and oxygen from water impurities in the vacuum.

2.2.4 Camera technique and operation

A LabView program (singlecamcontrol, or multicamcontrol) controls camera parameters, such as exposure time, gain adjustments, and size of images. Reducing the image size can enable faster frame capture. The LabView program automatically cycles through the day with the MST shot number collected from the MDS data tree before the shot. The cameras require an individual trigger per frame. Each trigger sourced from the MST remote trigger system which can produce up to 1023 trigger pulses on a 10 kHz clock. This is adequate for camera needs. The fastest speed the camera can operate at is 1000 Hz. Operating in this way requires images no taller than 200 pixels. An image may be taken every 1 ms allowing for up to 70-100 frames per MST discharge. Triggers are carried from MST remote trigger boxes to an optical fiber box which sends an optical pulse to each camera. In the camera

	200 kA	300 kA	400 kA	500 kA	400 kA QSH
Frame Rate	300	300	300	300	300
Exposure	30	40	80	100	80
Gain	1	1	1	1	1
	500 kA QSH	Fast Camera			
Frame Rate	300	1000			
Exposure	60	50			
Gain	1	2			

Table 2.1: A table of the commonly use settings for the BVC, listing frame rate in frames/s, exposure in microseconds, and gain.

power supply boxes optical signals are reverted to electrical signals and sent along the camera power cable to trigger the frame. Data is output from the camera in the form of gigabyte Ethernet signal, which is then converted to fiber, relayed across the MST machine area, converted back to Ethernet signal, and lastly input to the control PC. The control PC then writes data into a 640x480 byte array for each frame. Trigger data for the timing of each frame is stored. Common operating parameters for the cameras are shown in Table 2.1, with respect to plasma current. The exposure time is in μs and is chosen such that the pixel values do not saturate.

Each camera is mounted on a 2-D optical stage for axial focusing the image and left-right fine alignment, except for the prototype system, in which a single axial stage is used for focusing. Cameras require a bright light source for focusing. A light source was inserted into MST during venting, which allowed for alignment, but focusing the camera was difficult. The best approach was determined to adjust the camera positioning between discharges. Typically alignment is achieved in under 10 shots once one is familiar with making the adjustments.

The power seen by the cameras is measured after attaching the camera to an integrating sphere light source, optical housing, and a bandpass filter. The pixel intensities were measured as the power of the source was varied. Calibration occurred in an optics lab with the cameras and associated optics connected to the integrating sphere. The light source was operated at four power levels. This calibration of pixels to power observed can also be used to convert to photons required to transmit that much energy to the cameras knowing the energy per photon. Here the factor for D_α emission is 4.16×10^5 photons collected per pixel byte level. Camera pixels are 7.4 μm by 7.4 μm. Camera sensors were found to be in good agreement with the manufacturer specification. Each camera in turn was connected to the integrating sphere. The sphere power level was measured and a camera image was taken. The average pixel value of the image was calculated and plotted against the power

of the light source. The results of calibration are shown in Figure 2.13. All cameras are remarkably uniform in their pixel count to observed power.

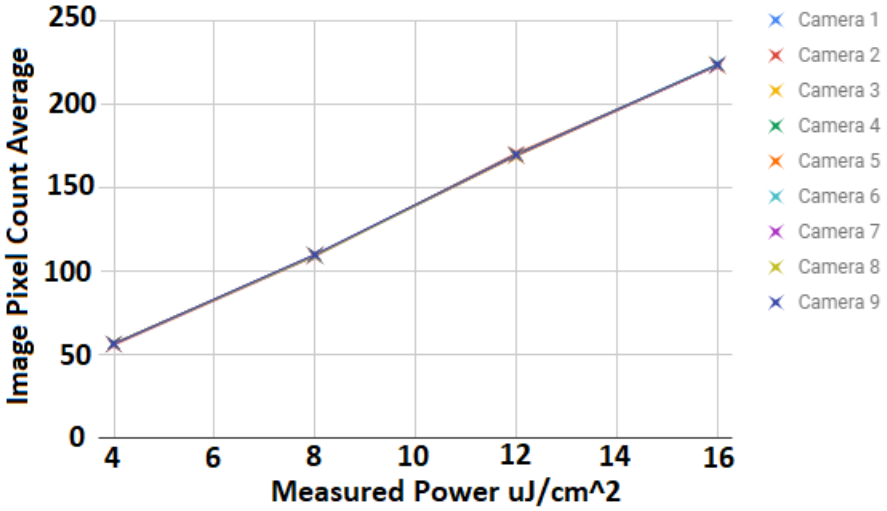

Figure 2.13: Calibration data for the Dalsa cameras when benchmarked against an integrating sphere light source.

2.2.5 Triple tip Langmuir probes

Langmuir probes were one of the first tools developed to study plasma [52]. A probe is constructed as an electrode inserted into a plasma which draws current, sampling the local plasma. Probes are still actively used today, although they have adopted a more sophisticated form. Probes are typically restricted to the plasma edge, where the plasma is much colder and less destructive to the probe. Probes used in this experiment consisted of three magnetic pickup coils inside a boron-nitride housing and a set of three 3.175 mm molybdenum electrodes. This made up the triple Langmuir probe head.

A probe inserted into a plasma creates a sheath around it. The plasma is a collection of free electrons and ions, that will reorganize themselves to cancel out local voltages such as the one created by biasing a probe tip. This effect is known as Debye shielding. The reorganization occurs because of the mobility of the electrons relative to the ions. A sheath forms around the probe with thickness defined by the Debye Length [5]:

$$\lambda_D = \sqrt{\frac{\epsilon_0 T_e}{n e^2}} \tag{2.12}$$

where n is the electron density of the bulk plasma away from the tip, T_e is electron temperature, e and ϵ_0 are the electronic charge and permittivity of free space. This formulation of the Debye length assumes immobile ions, which if taken into the calculation would reduce λ_D slightly.

One of the probe heads of a triple probe can "float" up to Φ_f, the floating potential. This potential is created because electron mobility is greater than ions. The flux of electrons to the material surface is initially greater then ions. This charges the floating tip to voltage, which then equalizes the rate of electrons and ions to the surface. The total current density seen by this tip is then:

$$J = 0.25e(n_i v_i - n_e v_e) \tag{2.13}$$

with n_e and n_i being the density of electrons and ions, and v_e and v_i being the mean velocity of those species. The total current collected by the probe tip, if it is floating will eventually tend to 0. However, if the probe tip is strongly biased, then either all the ions or all the electrons can be repelled. A probe biased negative will collect all the ions as the ion saturation current $J_{i,sat}$. A sufficient bias voltage would be on the order of 2-3 times the electron temperature in eV. Bias voltage for these experiments on MST was -200V. $J_{i,sat}$ can be calculated as:

$$J_{i,sat} = exp(\frac{-1}{2})en_{inf}(\frac{T_e}{m_i})^{1/2} \tag{2.14}$$

A triple tip probe has three electrodes. Two tips are biased relative to each other, and the third tip is the floating tip. This configuration is useful to the experiment. The simultaneous measurements of T_e,Φ_f, and n_e are obtained without sweeping the applied voltage, as in the case of a single tip probe. The first probe tip is biased negatively and collects the ion saturation current, that is:

$$J_1 = J_{sat}. \tag{2.15}$$

The second tip collects an equal and opposite current to tip one due to the relative bias. This current is from electrons due to the faster arrival rate of electrons to the probe tip, that is the electron current, depends on the thermal velocity of those electrons. It can be shown [64] that the T_e depends on explicitly measured quantities:

$$T_e = \frac{e}{ln2}(\Phi_f - V_2) \tag{2.16}$$

where the electron temperature is proportional to the difference between the floating and bias voltage. Similarly, once the electron temperature is known, the bulk ion density can be

worked out from the ion saturation current as:

$$n_i = \frac{J_{i,sat}}{0.61 A_{probe} e}\sqrt{\frac{kT_e}{m_d}} \tag{2.17}$$

where n_i is the ion density, with $n_e = n_i$ assumed in the MST edge. J_{sat}, V_{fl}, and V_p are the saturation current, floating potential, and bias potential recorded by the probe electronics, m_d and k are constants, the mass of deuterium and the Boltzmann constant, A is the probe area, and e the electronic charge [52].

Probe data collected over the entire discharge was analyzed only for the flattop (region of the peak near constant current) period of good quality QSH. The initial goal was to obtain probe data for 500 kA QSH plasmas. This was found to be impractical as the probe's casing was acting as a source of boron and nitrogen, and the QSH was unstable to the impurities. Probe data was collected over four days, with about 100 shots per day. QSH plasmas of target density $0.5 \text{x} 10^{13} \frac{\#}{cm^3}$ and I_p of 400-425 kA were used. Reliable QSH, where the 1/5 mode was sufficiently strong $Q > 8$ (Section 2.2.1) were able to be produced with the probes inserted up to 0.5 cm past the limiter at 400 kA. As the experimental campaign progressed, an attempt to raise the current was made. Advancing I_p beyond 425 kA caused the plasma to dither between QSH and MH states on approximately half the discharges.

The error for probe data shown in Chapter 3 is the standard deviation of the flattop averaged values. As the floating voltage is a direct measurement, the error works out to be:

$$\sigma_{T_e} = \sqrt{\frac{1}{N} * \sum (T_{ei} - \bar{T_e})} \tag{2.18}$$

Error in the electron temperature,σ_{T_e}, was from measurement and fluctuations in the floating voltage. T_{ei} is the shot average electron temperature as calculated as the difference between the bias and measured floating voltage, by Equation 2.16. $\bar{T_e}$ is the data set average for T_e for a given plasma condition. The ion saturation current is also directly measured, so its error follows a similar form:

$$\sigma_{J_{sat}} = \sqrt{\frac{1}{N} * \sum (J_{sat_i} - \bar{J}_{sat})} \tag{2.19}$$

with $\sigma_{J_{sat}}$ being the error bounds for the ion saturation current, and J_{sat_i} being the average ion saturation current for a single discharge, averaged over the flattop period, and $\bar{J}_{sat}$ being the mean of the data set for given plasma conditions. The plasma density is a derived quantity worked out from two other measured quantities, namely the saturation current

and the electron temperature, as such its error is propagated through the calculation.

$$\sigma_{n_i} = n_i * \sqrt{\frac{\sigma_J}{J_{sat}} + \frac{\sigma_{T_e}}{T_e}} \tag{2.20}$$

2.2.6 D_α Array

The neutral particle density can be informed by measurements of D_α photon emission. A D_α photon is generated by the transition between the n=3 and n=2 levels of atomic deuterium and has a $\lambda = 656.1nm$, a very small shift from H_α light of 656.3 nm. D_α emission strength is proportional to the ionization rate of neutral deuterium [65].

$$\gamma_{D_\alpha} \propto n_e n_0 \langle \sigma v \rangle_{ionization} \tag{2.21}$$

The neutral deuterium profile is observed by a seventeen-chord array of filtered monochromators that detect D_α emission as shown in Figure 2.14. The observation chords through a MST cross section are shown in the left half of the Figure. The collection optics of the photodiodes are shown in the right half of the Figure. High speed photodiodes pick up the signal which is then amplified and stored. The photodiodes have bandpass filters which transmit light at 657 nm with a FWHM of 11 nm. This filter enables collection of D_α light. D_α chords span from -0.9 < r/a < 0.9, allowing the full cross section to be measured.

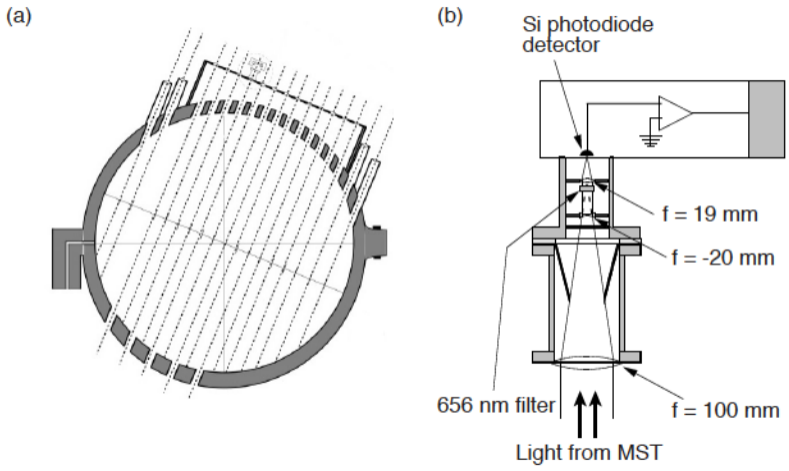

Figure 2.14: D_α emission array with the physical layout shown in (a) and the measurement technique in (b). Reporduced from Eilerman's A.1 [23].

2.2.7 Bolometers

Bolometers measure all the radiation from the plasma in a given line of sight. In a plasma this means neutral particles and photon radiation. Pyrobolometers are paired with XUV photon detectors. The XUV can detect the radiation heat flux, and the pyrobolometer will measure the total heat flux. MST has 5 bolometers about the vessel. A pyrobolometer/photodiode pair mounted on the exterior of MST is shown in Figure 2.15. The detectors are recessed 20 cm from the vacuum vessel to provide collimation of the signal and to prevent charged particles from being measured. A gate valve allows for the diagnostic to be removed for repair or testing.

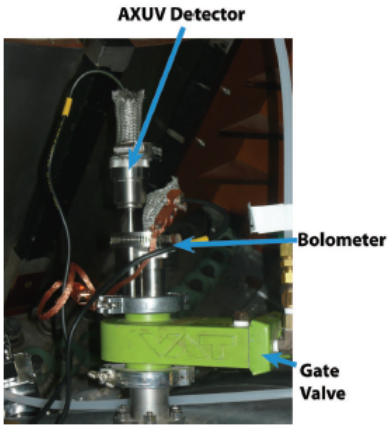

Figure 2.15: Bolometer on MST. Labeled from the exterior are the gate valve, and the housing for the pyrocrystal, and the XUV detector.

Pyrobolometers generally operate on a proportionality between the temperature of the crystal, and the electric polarization of the crystal $P = k_{pyro}T$. MST's bolometers are made of $LiTaO_3$ and are ferroelectric, which allows for the crystal to heat up and cool down cyclically. As the temperature of the crystal rises the increase of the electric field draws current proportional to the heat flux on the crystal, $I_{bolometer} \approx \frac{k_{pyro}PA}{c\delta}$, with I being the current drawn, P being the power flux to the crystal, A being the area of the crystal, and c being a coefficient that relates temperature to stored energy, and δ being the width of the crystal. MST bolometers have a diameter of 10.6mm, thickness of 0.5 mm, k_{pyro} of 0.096 μJK^{-3}, and c coefficent of 0.251 J $g^{-1}K^{-1}$. Estimated detection levels are $6.5x10^{-8}$ Amps/Watt [66].

The sensitivity of the XUV sensor to photons, starting from the visible spectrum near 1 eV and progressing into the UV and XUV is shown in Figure 2.16. It is possible to calculate

the contribution from neutral particle flux to energy exhaust by removing the power of photon radiation from the total power measured by the pyrobolometer [67].

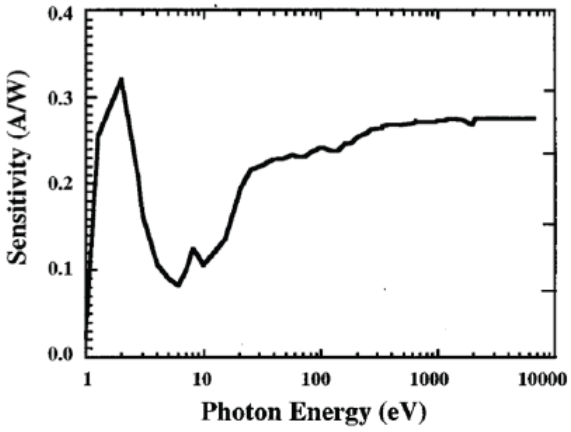

Figure 2.16: Photon radiation sensitivity of XUV detectors used as bolometers on MST. Originally from A.3 of Waksman [66]

2.3 Computational tools and code details

The use of computational tools is necessary to determine the contribution of neutrals as a power exhaust channel in MST. Direct measurement of the full 3D plasma-neutral interaction is all but impossible with the availability of diagnostic space on MST. Therefore, modeling is used for this calculation. The BVCs inform the source rate of neutrals for the modeling effort, and reconstruction codes provide a plasma background. EIRENE is the workhorse of this framework. The codes V3Fit and MSTFit provide plasma background. EIRENE then uses a Monte-Carlo kinetic transport model to calculate the motion and interaction of the neutrals.

2.3.1 EIRENE

The EIRENE code [11] is a general-purpose tool for modeling the interaction of plasma and neutrals (particles or photons). This Monte-Carlo code uses a combinatorial discretization of general 3D computational domains. It is a multi-species code solving simultaneously a system of time-dependent (optional) or stationary (default), linear or non-linear kinetic transport equations of arbitrary complexity. A basic model for transport of ionized particles in an externally specified magnetic field is also included. EIRENE is coupled to external

$D + e^-$	$\rightarrow$	$D^+ + 2e^-$	electron impact ionization
$D^+ + D$	$\rightarrow$	$D + D^+$	charge exchange
$e^- + D_2$	$\rightarrow$	$e^- + D + D$	dissociation
$e^- + D_2$	$\rightarrow$	$2e^- + D_2^+$	non dissociative ionization
$e^- + D_2$	$\rightarrow$	$2e^- + D + D^+$	dissociative ionization
$e^- + D_2^+$	$\rightarrow$	$2e^- + 2D^+$	dissociative ionization
$e^- + D_2^+$	$\rightarrow$	$e^- + D + D^+$	dissociative excitation
$e^- + D+$	$\rightarrow$	$D + h\nu$	recombination
$e^- + D_2^+$	$\rightarrow$	$D + D$	dissociative recombination

Table 2.2: Table summarizing the reactions used in EIRENE for this work, and a brief description of the reaction.

databases for atomic and molecular data and for surface reflection data. It can call various user-supplied routines for exchange of data with other (fluid-)transport codes. The main goal of the code's development was to provide a tool to investigate neutral gas transport in magnetically confined plasma. Due to its flexibility, it also can be used to solve more general linear kinetic transport equations, by applying a stochastic rather than a numerical or analytical method of solution. Simulations run for this thesis were done on a computational domain of regular toroidal grid divided into a 90x50x50 radial by poloidal by toroidal mesh.

The general Boltzmann transport equation is:

$$[\frac{\partial}{\partial t} + \mathbf{v}\cdot\nabla_r + \frac{\mathbf{F}(\mathbf{r},\mathbf{v},t)}{m}\cdot\nabla_v]f(\mathbf{r},\mathbf{v},t) + \sum_t(\mathbf{r},\mathbf{v})|\mathbf{v}|f(\mathbf{v}) = \int d^3\nu' C(\mathbf{v}'\rightarrow\mathbf{v})|\mathbf{v}'|f(\mathbf{v}') + Q(\mathbf{r},\mathbf{v},t) \tag{2.22}$$

where the distribution function F for a species is in 3 spatial, 3 velocity, and 1-time dimensions, Q is a source term for the species, and C is a collision operator which moves particles between energies. A solution is obtained by transporting many test particles from their source location and source energy, through the plasma background, with collisions occurring. Reactions used in this thesis are shown in the Table 2.2. These reactions are chosen to allow all possible paths of a molecular deuterium being dissociated, excited, or ionized as either a molecular or atomic species.

The rates for these collisions and other process are drawn from molecular and atomic interaction databases. HYDHEL and the AMJUL databases are utilized [68, 69]. Material databases for sputtering and other material interactions are sourced from the TRIM code [70]. EIRENE can be coupled for data exchange with fluid transport codes or user-generated data to populate the cells. Two popular combinations are the B2 and EMC3 fluid codes [71, 72]. No fluid coupling is used in this work due to the reversed field nature of the RFP,

which would be incompatible with the flux coordinates of EMC3 or B2. For input data, the code takes either standard 1D, 2D, or 3D grids and can expand on these by adding "input surfaces" which are defined by boundary representations of cells. Surfaces can then be assigned properties such as transparency, reflection, recycling source, or pump sink. These surfaces act then as terms in the single reservoir model of the particle balance, Eqn. 2.2. The Φ_{rec} and Φ_{wall} terms are represented as various neutral sources in EIRENE. Fueling efficiencies are calculated by tracking which neutrals ionize and which are removed by pumping. Volume elements are assigned plasma properties, which in the simplest case is just temperature, and density, and magnetic field vector. Each species of plasma particle is defined; that is electrons, bulk ions, or impurities wished to be included in the model. Particles may be sourced from points, lines, surfaces, or volumes. Time dependency in the code is handled by advancing particles a set distance for a given energy, then saving the simulation data, then updating the background and repeating the calculation. This allows for an iterative approach to a time dependency. EIRENE is used with reconstructions from MSTFIT or V3Fit providing the necessary background data with no additional coupling.

A graphic summarizing the input and output data of EIRENE is shown in Figure 2.17. On the left of this chart are the inputs to the EIRENE code. The input quantities of interest are n_e, T_e, $\mathbf{B}$, cross-sections, and collision data. The user must define neutral sources fully in EIRENE; this input data is based on camera measurements. Material databases and models are packaged with EIRENE to handle PMI. The plasma backgrounds also must be user defined; these are produced by other reconstruction codes. Lastly sets of reactions from atomic databases are required. EIRENE outputs n_N profiles as well as the interactions and energy losses between those neutrals and the plasma background.

2.3.2 Plasma backgrounds

The first of the computational tools used to model the plasma background in MST is the MSTFit code [29]. MSTFit is a toroidal geometry equilibrium reconstruction code. The full details of the code are found in Anderson's thesis [29], but a summary is described below. MSTFit solves the Grad-Shafranov equation for MST geometry,

$$\Delta^* \Psi = -\mu_0 R^2 \frac{dp}{d\Psi} - \frac{1}{2}\frac{dF^2}{d\Psi} \tag{2.23}$$

MST diagnostic data is used to constrain the equilibrium. The data MSTFit will utilize are pressure profile, plasma current, and toroidal flux. MSTFit does have some limitations such as the assumption that all quantities are toroidally symmetric. Most quantities are poloidally symmetric as well. MSTFit is a used to obtain 1-D profiles of plasma parameters. If Thomson

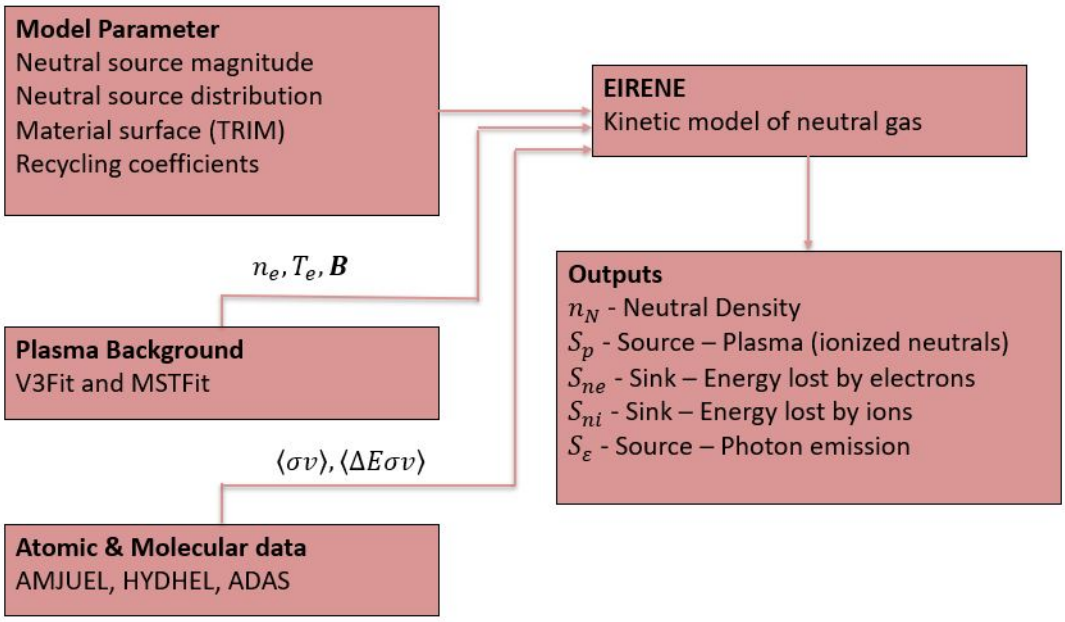

Figure 2.17: Overview of the EIRENE workflow used as a flowchart. On the left side are the input data to the model. Quantities of interest are shown above the arrows that connect data sources to the code. The output of the flow highlights the sources and sinks modeled by the EIRENE code, which inform the particle and energy balance.

scattering data is available, the electron temperature profile is fit to the data; otherwise a model based on I_p determines the electron temperature profile. Line integrated density data comes from the FIR [73] and CO_2 interferometers [15]. A sample reconstitution of the plasma temperature and density profiles are shown in Figure 2.18. Here the density profile is a function of radius with no toroidal and poloidal variation. Shafranov shift moves the otherwise symmetric plasma outboard 2-3 mm, this as a slight skew towards higher radius of the density. The peak density is 7.8×10^{18} $\frac{\#}{m^3}$ which is slightly below the average target density of 1.0×10^{19} $\frac{\#}{m^3}$. Density gradients are large in the edge plasma. T_e is collected by Thomson scattering and fit to a MSTFit equlibrium. The profile of the data is plotted as a function of normalized radius ρ. Error bars are large in the plasma core and diminish in the plasma edge. The gradient in T_e is less severe than the density gradient. Experimentally measured temperature decreases moving from central to edge regions, while MSTFit models the temperature of the core region as flat. This data for standard plasma has no angular dependence. There are no error bars in the edge because the Thomson scattering signal error is on the order of the measurement in the edge.

While MSTFit provides a solution for the background for MH plasmas, a 3D code

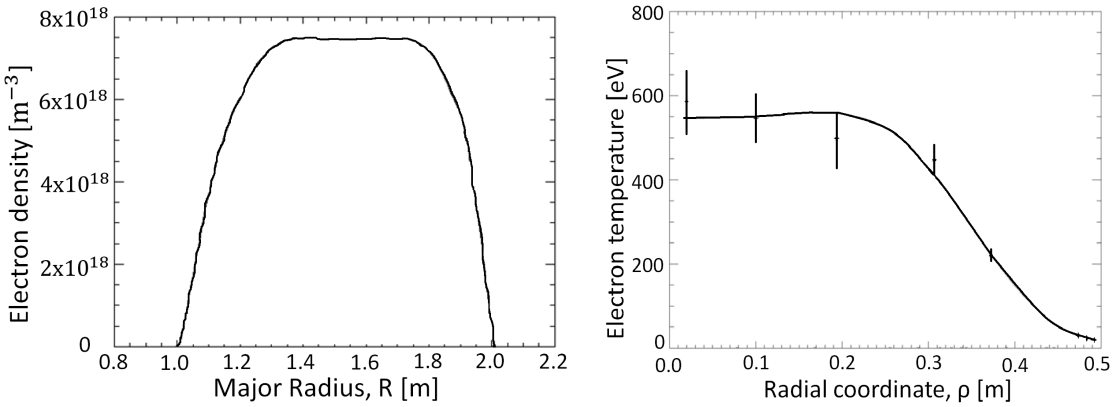

Figure 2.18: MSTFit temperature and density profiles computed for a sample 400 kA MH plasma.

is required for the QSH plasmas. V3Fit is used to reconstruct MST QSH plasmas using data from available diagnostics to produce the best fit equilibrium. V3Fit is a code for performing equilibrium reconstruction in three-dimensional plasmas. It is a modular code that computes an arbitrary internal state of the plasma based on the externally measured response [74]. Magnetic array data is required to perform the reconstruction. Flux surfaces from a well-diagnosed QSH shot are shown in Figure 2.19. In this Figure the QSH mode helical axis has caused the flux surfaces in the central region to take on a "bean" shape. The code predicts increasingly circular flux surfaces as radius increases. Profiles for this shot, where the radial coordinate is the percent of magnetic flux enclosed, are shown in Figure 2.20. The plasma density drops off monotonically with the radius, that is, decreases from the core to the edge region. Peak density is at 6.8x10^{18} $\frac{\#}{m^3}$ on the higher end of experimentally attainable QSH density for MST. The T_e profile is in contrast to the density profile as it has a peak around 0.4 of normalized radius. This peak in temperature is caused by improved confinement in the QSH core, although the peak value is not substantially hotter than the central plasma, the whole plasma is hotter than the comparable MH case shown in Figure 2.18.

EIRENE's custom plasma background profiles require that the cell parameters (plasma parameters) be specified by the user for all computational cells. Temperatures were mapped from the flux coordinates of the equilibrium reconstruction codes to regular geometric grid locations. This data was translated into an EIRENE compatible format as seen in Figure 2.21. Minimal loss of information is achieved. The cell centers in R-Z coordinates were calculated. The nearest V3Fit data point was found. Its temperature, density, and B-field data were formatted and written into files that became EIRENE input. While some

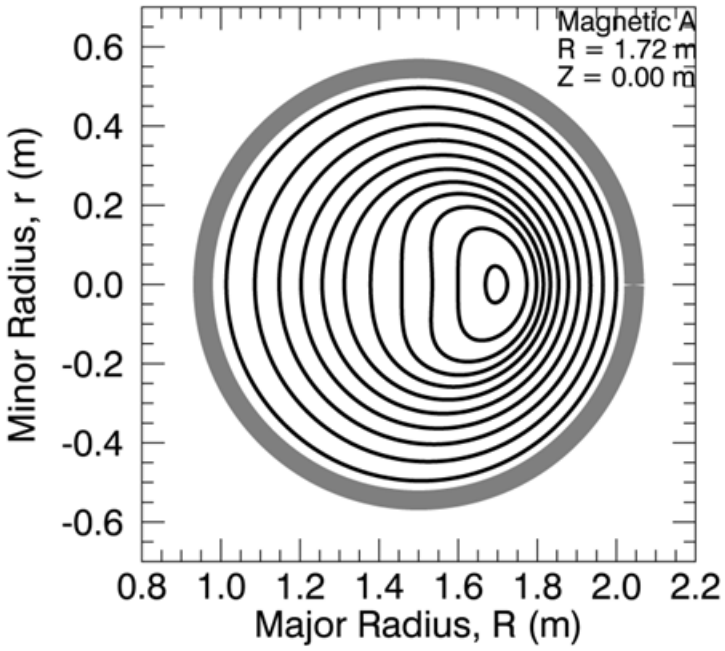

Figure 2.19: V3Fit flux surfaces for an example QSH plasma. The helical bean shaped core region is easily seen aligned outboard. This particular flux surface is reconstructed from MST discharge 1110602080 from a poloidal cut that is aligned outboard. V3Fit reconstruction performed by Boguski.

of the data density around the helical core is lost the shape and magnitude of the data is preserved. A bean-shaped hot spot exists on the Figure. This structure rotates poloidally as different toroidal cuts are selected.

2.3.3 Neutral source construction

The neutral source input of EIRENE is constructed based on camera observations. Camera images provide a spatial distribution of D_α emission from the edge plasma region. The EIRENE simulations in this work are constructed using three surface sources. These surfaces represent the outboard limiter, the wall, and the poloidal gap limiter. The two limiters are defined as additional surfaces in the simulation. The outboard limiter surface is subdivided into 5-degree toroidal slices, from 0 to 360 degrees. Each 5-degree region is then assigned a total flux based on camera observations of that region. The outboard limiter source is composed of a mix of atomic and molecular deuterium. The MST wall region is a uniform recycling source of thermal molecular deuterium. The poloidal gap limiter source is used only in the simulation of helical plasma. The poloidal gap limiter

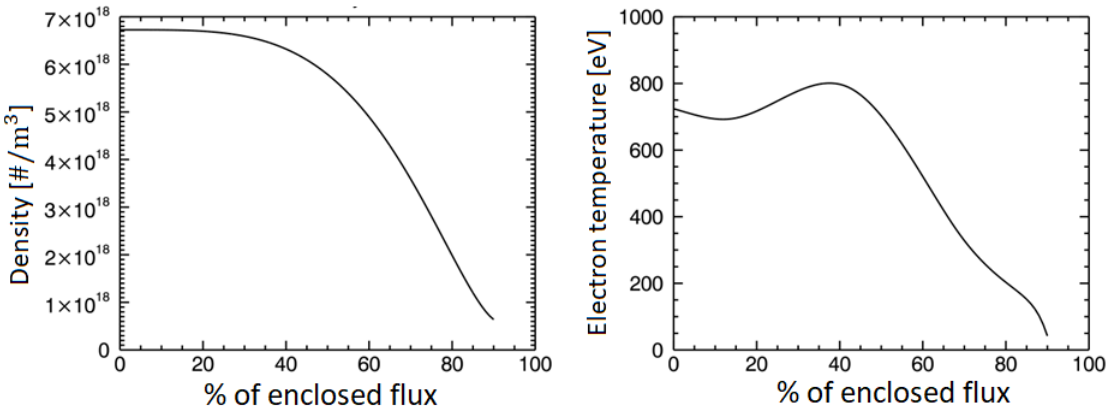

Figure 2.20: V3Fit temperature and density profiles as a function of enclosed flux. Density is monotonically decreasing outward with increasing radius. Temperature does not track monotonically downward from the center as a result of the helical core providing thermal confinement in helical axis.

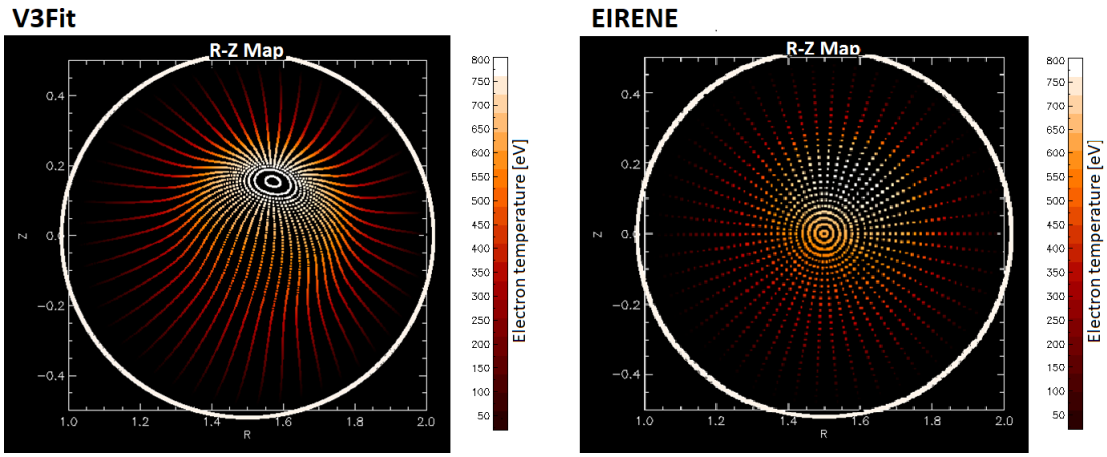

Figure 2.21: Mapping based on V3Fit used for EIRENE cells showing a side by side of the V3Fit and EIRENE temperature profiles.

source is a point source on the limiter titles which is phase aligned to the helical magnetic mode at the gap. The poloidal gap source intensity is calculated based on the interpretation of camera images.

A sample of the TRIM data that EIRENE uses for sampling the reflection probability of a deuterium particle is shown in Figure 2.22. This data is for the reflection deuterium on carbon. A different incidence angle is shown in each panel of the Figure. EIRENE linearly interpolates this data as needed. Data sets for energy and momentum reflection for particle wall interactions are also utilized. The primary ones used in setting up EIRENE physics

in MST are D on C (graphite limiters) and D on Al (vacuum vessel). EIRENE outputs tabulated data of the neutral density over the computational cells. The geometry used in EIRENE is a simple torus with additional limiters and pump duct cells. A cross-section of this geometry can be seen in Figure 2.23. In this Figure, the geometry of EIRENE is shown. In green are the limiting surfaces. A small number of particle tracks are shown; in blue are traces of molecule deuterium and in red are traces of atomic deuterium. Traces end in electron or ion collisions, such as ionization.

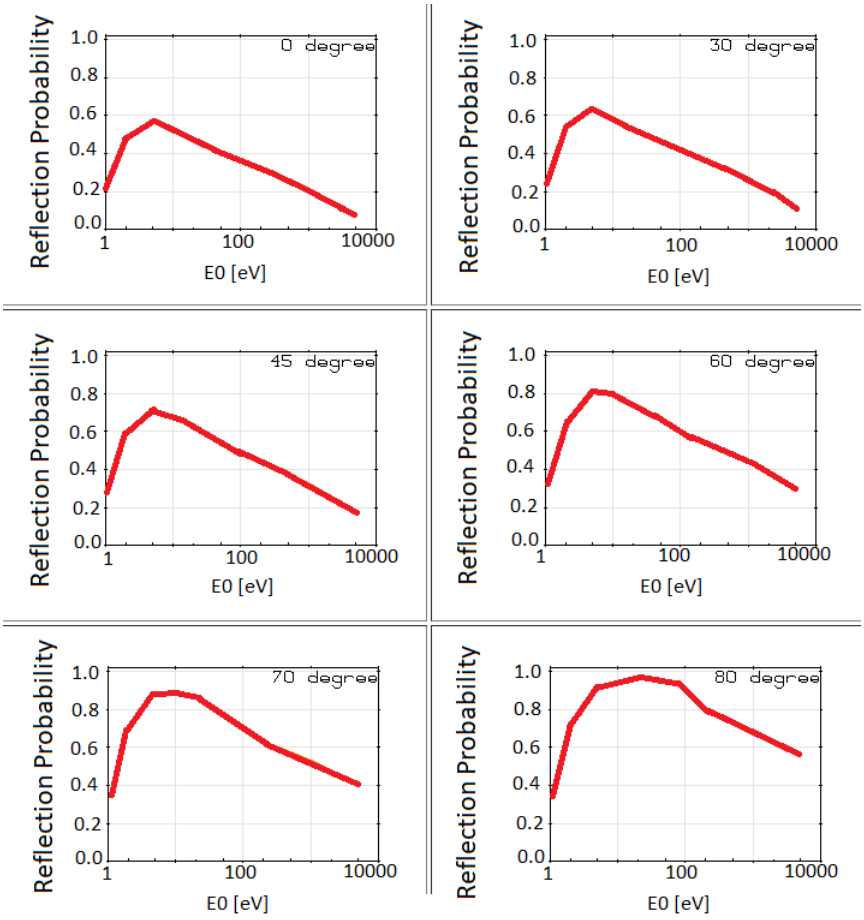

Figure 2.22: Trim data used in EIRENE showing the reflection probability of a deuterium atom onto a carbon surface at various angles of incidence measured from the vertical (such that 0° is perpendicualr).

EIRENE outputs can include the neutral density, neutral temperature, and atomic emission for each cell. Ions produced from charge exchange are tracked. Surfaces may be defined about the plasma volume, or subsets of volume to tally photon and neutral particle fluxes over them, as a measurement of radiation or charge exchange fluxes. EIRENE also

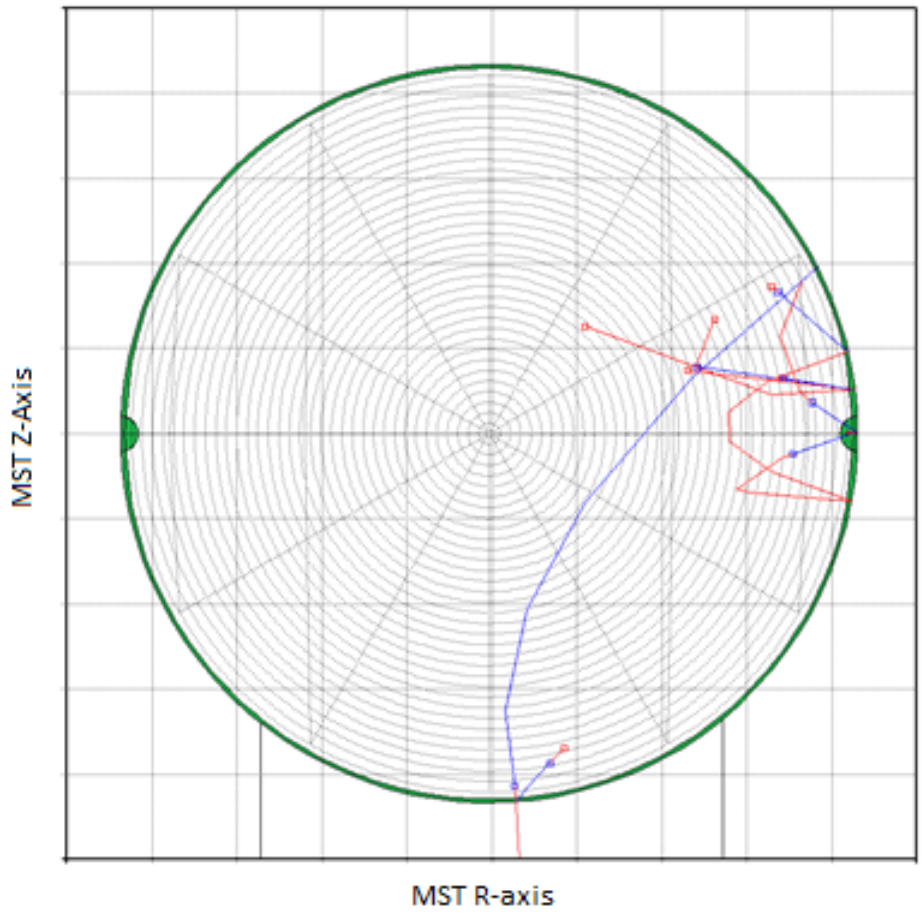

Figure 2.23: EIRENE MST geometry, showing the vessel wall, limiters, and a pump duct with sample particle traces in red and blue. Here the blue traces are that of molecular and the red is atomic deuterium. Collisions occurring are represented by a square. Units are omitted as gridlines are in terms of the simulations boundaries, rather than machine size. The red track leaving the vacuum vessel at the bottom of the Figure is detuerium lost to pumping.

can calculate the energy transferred between the neutrals and the plasma as a result of collisions.

2.3.4 Interpretation of images

The interpretation of spectroscopic quantities is difficult because the quantities are often a line of sight or imaged through a plasma where the local parameters that produced emission are not well known. A flux of particles on a limiter can be obtained by the

proper interpretation of the D_α emission at $\lambda = 656.1nm$. Camera images are converted to recycling fluxes using the S/XB formalism. The S/XB coefficient assumes all neutrals entering the plasma are atomic, which is usually not the case [75]. Under 1100 K graphite recycles 90% as molecules and 10% as atoms. As the surface temperature rises graphite releases more atomic and less molecular deuterium [46]. The S/XB coefficient for a neutral molecule tends to be a factor of two more than if the same total number of particles are started as atoms and then ionized [76]. The S/XB factor changes as a function of the local plasma parameters as neutrals propagate inwards. A particle flux onto the limiter Γ is obtained by multiplying photon flux Φ by the S/XB conversion factor:

$$\Gamma = S/XB(n_e, T_e) \cdot \Phi \tag{2.24}$$

This S/XB coefficient is derived from the absolute intensity, $I(r)$, of a photon line emitted at a position r from particles $n_A(r)$ by electrons $n_e(r)$ with a rate coefficient $\langle \sigma_{Ex} \nu_e \rangle$. The quantity $\langle \sigma_{Ex} \nu_e \rangle$ is the rate coefficient for the excitation of neutral atoms to an excited state.

$$I(r) = B \frac{h\nu}{4\pi} n_a(r) n_e(r) \langle \sigma_{Ex} \nu_e \rangle \tag{2.25}$$

where the factor of $4\,\pi$ represents the emission isotropically, and with B being the branching ratio. The quantity $\langle \sigma_{Ex} \nu_e \rangle$ is the velocity weighted rate coefficient for ionization interactions of neutral atoms. This intensity which may be integrated over the line of sight or the volume observed to give the total intensity, I_{total}. The atomic flux that enters a plasma is similarly computed as

$$\Phi_A = \int_{r_1}^{r_2} n_A(r) n_e(r) \langle \sigma_I \nu_e \rangle dr \tag{2.26}$$

where σ_I is an ionization cross-section. This atomic flux is the source that creates the ionization observed. A solution is possible with knowledge of the T_e and n_e everywhere. This is where modeling with a synthetic diagnostic becomes useful. The relation can be simplified to

$$\Phi_A = \frac{4\pi}{\Gamma} \frac{I_{total}}{h\nu} \frac{\langle \sigma_I \nu_e \rangle}{\langle \sigma_{Ex} \nu_e \rangle} = 4\pi \frac{S}{XB} \frac{I_{total}}{h\nu} \tag{2.27}$$

where S/XB relates the photon intensity to atomic flux, which depends only on the local temperature and density of the plasma. That is the S/XB coefficient is the ratio of the rate ionization to rate ($\langle \sigma_{Ex} \nu_e \rangle$) of excitation ($\langle \sigma_{Ex} \nu_e \rangle$) of the neutral particles for a particular plasma. The S/XB coefficient can further be adjusted in the presence of molecular flux.

$$\left(\frac{S}{XB}\right)_{effective} = S/XB\left(1 + \frac{2\eta \Gamma_{D_2}}{\Gamma_{total}}\right) \tag{2.28}$$

where here the effective S/XB is boosted by a factor η, which is proportional to the ratio of the molecular to the total influx of neutral particles. η depends on the types of processes available when dissociating or exciting and is usually on the order of a few (2-3) [46]. EIRENE was used to calculate the effective S/XB coefficients for a given plasma background. These effective coefficients then allowed for the conversion of the experimentally measured photon fluxes to provide an absolute magnitude of the recycling source.

The use of a synthetic diagnostic is inspired by previous work in the 3D-PSI group in EMC3-EIRENE [76]. This work, however, uses EIRENE as a standalone code, without the coupling to EMC3. A set of cameras to match the boundary viewing cameras are set up in the model. EIRENE can output the D_α emission from each cell. Line of sight integrals for each camera pixel looking through the EIRENE grid are then computed and synthetic images are produced. The EIRENE model has a plasma background for each cell, which can produce simulated emission that the volume would have generated for the sourced recycling flux. Synthetic emission enables the reconstruction of a synthetic camera image which can be compared to the source images, from which the recycling fluxes are derived,

$$\Phi_{ij} = \int_{LS} \epsilon(s) ds \tag{2.29}$$

with $\epsilon(s)$ being the photon emission rate in a cell calculated by EIRENE. When discretized, this value is taken to be the cell averaged emission rate.

$$\Phi_{ij} = \sum_{k}^{n} \epsilon_k \cdot \delta s_k \tag{2.30}$$

Cameras are defined to have a source, a target, a view angle, and pixel count. An image plane is calculated based on the view angle and target location. Lines of sight are traced for each pixel to a location through the plasma domain until a wall is intercepted. The line of sight is then integrated to obtain emission from the plasma. Plasma emission is based on both molecular and atomic contributions to the D_α light.

Once a given plasma background is established, a set of deuterium molecules are sourced. The source distribution matches the relative spatial photon distributions seen by the camera on the outboard limiter. These particles and their interactions are simulated to determine an effective S/XB for a given plasma background. EIRENE calculates emission of photons per cell and the results are tallied against the ionizations that occur per cell. The calculation of this effective S/XB is shown in Figure 2.24. Here the results of 4 lines-of-sight are presented on a view for camera #2.

The average S/XB over all camera lines-of-sight is weighted by relative neutral density

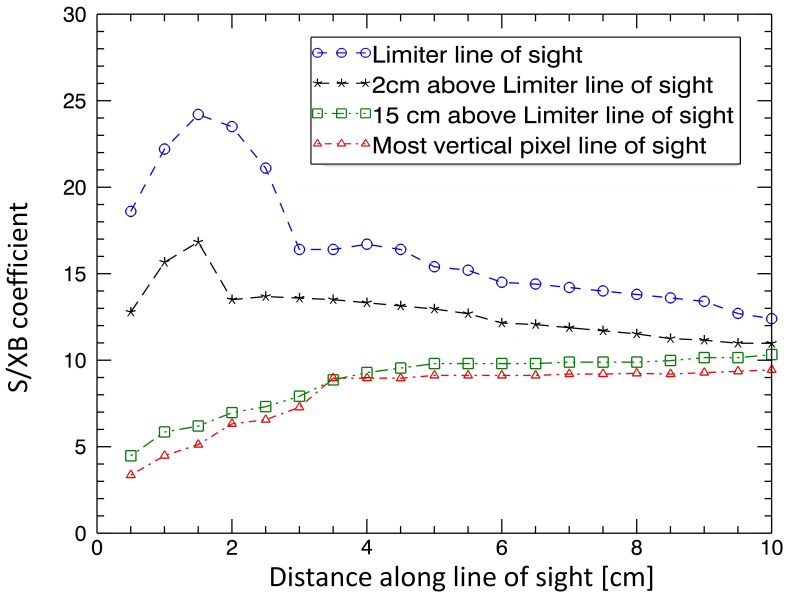

Figure 2.24: A sampling of S/XB coefficients in a 400 kA QSH Plasma. The corresponding effective S/XB coefficients is calculated along the line for the first 10 cm of distance from the wall to the camera.

in the cells; this produces an effective conversion factor for each camera per configuration. The plasma edge, where the largest populations of molecular deuterium reside, influence the calculation the most. Cameras with more perpendicular angles onto the limiting surfaces tend to have slightly lower effective S/XB coefficients; this is a geometric effect of the viewing angle. A table of effective conversion coefficients for the full images is shown in Table 2.3. These conversion factors allow for the camera source distributions to be converted from a photon flux to a particle flux. An absolute calibration mapping for the system is thus generated.

	Camera 1	Camera 2	Camera 3	Camera 4	Camera 5
400 kA QSH	25.9	24.2	24.4	25.2	24.3
500 kA QSH	29.7	27.8	28.0	28.9	27.9
200 kA MH	15.3	14.3	16.6	17.1	16.5
300 kA MH	17.2	16.1	16.3	16.8	16.2
400 kA MH	19.4	18.2	18.3	18.9	18.2
500 kA MH	24.6	23.3	23.5	24.3	23.4

	Camera 6	Camera 7	Camera 8	Camera 9
400 kA QSH	26.1	24.5	24.4	24.6
500 kA QSH	30.0	28.1	28.0	28.2
200 kA MH	17.8	16.7	16.6	16.7
300 kA MH	17.4	16.3	16.3	16.4
400 kA MH	19.6	18.4	18.3	18.5
500 kA MH	25.1	23.6	23.5	23.7

Table 2.3: Effective S/XB coefficients for each of BVCs

Chapter 3

Breaking symmetry in the MST edge

3.1 Helical deformation of the QSH edge

The QSH plasma edge of MST has been experimentally measured with Langmuir probes for the first time. Probe measurements of the QSH edge reveal that the kinetic plasma edge is helical. The T_e rises a factor of five from $\approx$ 10 to 50 eV and n_e rises from $\approx$ 0.5x10^{18} to 2.5x10^{18} m^{-3} when the core magnetic mode is aligned to the probe. These peaks are consistent at two measurement locations that differ by 75 toroidal degrees on the machine. A 1/5 helicity is seen of the pressure in the edge that matches the core magnetic mode is observed based on measurements.

In order to accurately model the MST boundary, notably in the QSH state, direct probing of the edge was required to obtain plasma parameters n_e and T_e, with the assumption that $n_e = n_i$. Triple tip Langmuir probes described in Section 2.2 were used to measure the edge electron temperature and density of QSH plasmas. The probes were inserted at $\phi = 30$ / $\theta = 15$ and at $\phi = 90$ / $\theta = 90$. A cartoon is drawn in Figure 3.1 where the probe locations are highlighted on MST. This cartoon is overlaid on a set of V3Fit flux surfaces. In order to account for the Shafranov shift of the plasma, MH plasmas were made at the start of the day. The probes were advanced inwards in 0.1 cm steps until an ion saturation current was measured. For probe 1 (30/15), this location was 1.3 cm from the wall, essentially what was defined by the outboard belt limiter, to be the last closed flux surface (LCFS). Measurements from probe one were also made at 1.8 cm from the wall to obtain data inside the LCFS. Probe 2 had to be inserted to 2.6 cm before a signal was detected. Similarly, measurements were made at this location and at 3.1 cm from the wall to obtain data at the LCFS and 0.5 cm inside the LCFS.

Probe data is collected at two depths, the LCFS and 0.5 cm inside the LCFS. A lock angle is calculated as the relative angle between the probe head and the helical mode. A lock angle of 0 implies the QSH core magnetic mode is aligned radially in front of the probe

head. As the probes are stationary, the QSH state is rotated by altering the lock angle of the MST active feedback system, enabling a phase scan of the QSH edge. Measurements were made every 10 degrees in the phase scan of the QSH edge. The resulting data from probe measurements is shown in Figures 3.2 and 3.3. In these Figures, the plotted data points are offset by -3 degrees if representing the quantity 0.5 cm inside the LCFS and +3 degrees if representing the quantity on the LCFS to reduce overlap and improve clarity. The bias voltage used in the probe experiments was 200V, well beyond the expected value

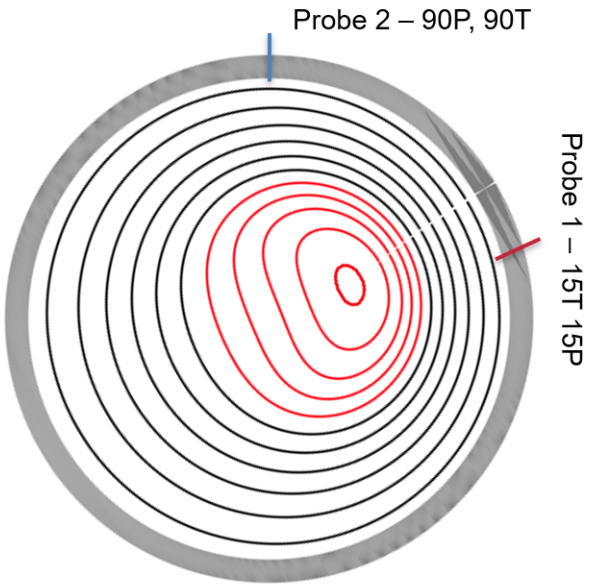

Figure 3.1: A cartoon of the probe locations on MST overlaid on V3Fit flux surfaces for a QSH plasma. Helical flux surfaces are shown in red. The flux surfaces are compressed outboard due to the Shafranov shift of the plasma. In order to reach the confined plasma with the vertical probe insertion to a greater depth than the probe near the limiter was needed.

of the edge electron temperature. It was difficult to obtain good quality QSH plasma with the probes further inserted due to boron impurity generation from plasma interaction with the probe housing causing a back transition out of the QSH state.

Electron temperature is measured in the MST edge by the Langmuir probes and shown in Figure 3.2. The relative lock angle is shown on the X-axis. Electron temperature shown in red, is 10 eV when measured 0.5 cm inside the LCFS, with the exception of a thermal peak that exists at 20-30 degrees. The value at 0 degrees is also slightly elevated. The

temperature data on the LCFS in blue peaks at 10 degrees misalignment between the probe and QSH mode. Temperatures are slightly colder on the LCFS than on inside the LCFS. The temperature on the LCFS is at a minimum around ±80-100 degrees when the core magnetic mode is perpendicular to the probe. The temperature peak on the LCFS is 8.2 times the average value of the other positions measured at this depth. The peak inside the LCFS is a factor of 5.4 above the average value of the other positions on this depth.

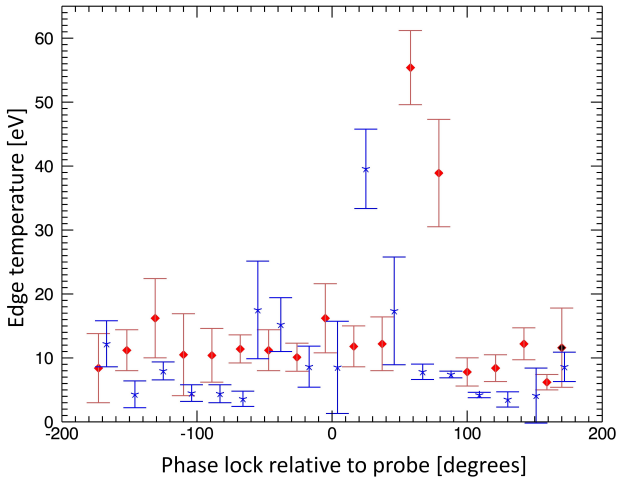

Figure 3.2: Edge electron temperatures measured by probes in QSH plasma. The x-axis is the phase the mode is locked relative to the probe, where 0 phase would indicate the mode is aligned to the diagnostic (red/diamond located at 0.5 cm past the limiter, and blue/star approximately sampling LCFS)

The electron density is measured in the MST edge by the Langmuir probes and shown in Figure 3.3. The relative lock angle is shown on the X-axis. The peak in the density profile is even more obvious than in the electron temperature data. Again, blue represents the data recorded on the LCFS, and red represents data from 0.5 cm inside the LCFS. When measuring density on the LCFS when the QSH mode is more than 20 degrees away from the probe head, J_{sat} is occasionally found to be at the noise level of the probe electronics. When the QSH mode is locked to the probe the density is peaked at $4.6\text{x}10^{17} m^{-3}$. When the probes were inserted 0.5 cm deeper into the plasma the density bulge widens.

Both temperature and density rise in the presence of the helical mode. When the mode is not locked at a probe location, the profiles are flat. This supports the idea that the edge structure is created due to proximity to the helical core. Probe spacing is sufficiently far apart that each samples a different 1/5th of the QSH mode as it is rotated through its locking positions supporting the hypothesis that the edge structure matches the core helicity. The

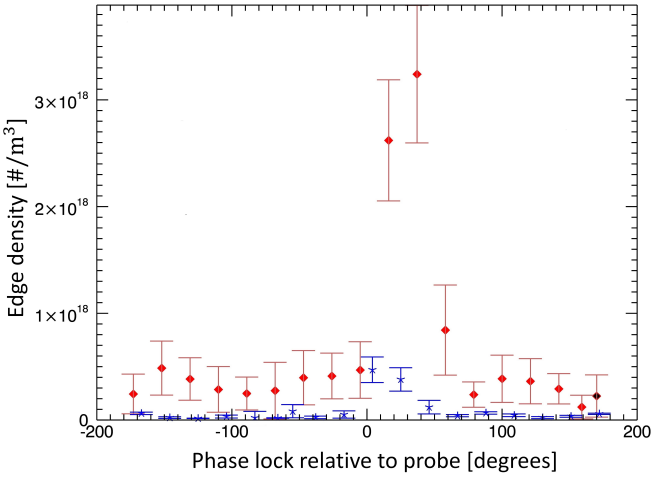

Figure 3.3: Edge particle density calculated from ion saturation currents on probes in QSH plasma. The x-axis is the phase the mode is locked relative to the probe, where 0 phase would indicate the mode is aligned to the diagnostic (red/diamond at 0.5 cm past the limiter, and blue/star approximately sampling LCFS

pressure of the plasma edge, that is the combination of n_e and T_e, is shown in Figure 3.4. The pressure has been converted to units of Pascals. The pressure on the probes is shown as a function of the magnetic mode phase lock relative to the probes' wall position. The pressure bulge is seen in the Figure as a factor of 5-10 higher plasma pressure when the core magnetic mode is aligned near the probes. A small phase shift is seen in the plot, with peak pressure at the LCFS occurring at 15 poloidal degrees relative to the mode aligned to the probe. At the measurement point 0.5 cm inside the LCFS the location of the pressure peak shifts to 20-30 poloidal degrees misaligned to the probe head. In terms of toroidal degrees this mismatch to the probe head is only 3-6 degrees. Pressure in the helical edge bulge is found to be 10-20 times larger than pressure measured at the same depths into the plasma when the mode is aligned away from the probes. The pressure measurements are not sinusoidal, suggesting that the helical core is causing a perturbation of the flux surface at the edge, resulting in hotter more dense plasma coming in contact with the limiter, producing the 5 "hot spots" seen in camera measurements of the PWI. Despite a slight phase shift, the pressure measurements suggests a helical plasma edge exists in QSH plasma which is phase aligned to the core magnetic structure.

Using the active feedback system of MST, a phase scan of the QSH plasma was performed by changing the locking position at the poloidal gap, effectivly rotating the plasma toroidally over the probes. The phase dialed in as the locking angle is measured relative to the poloidal

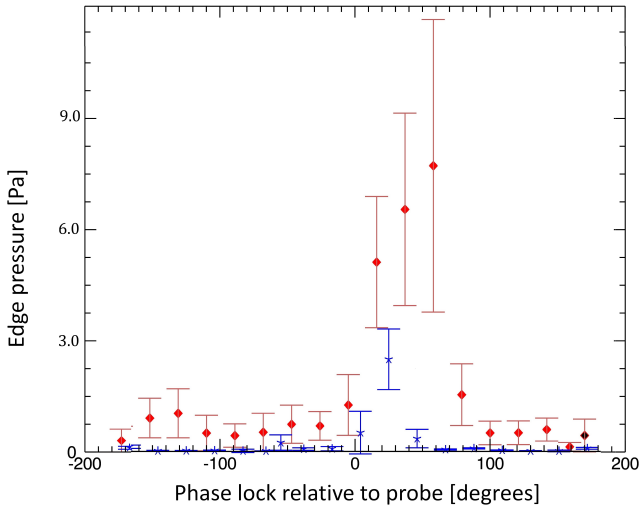

Figure 3.4: Pressure plotted as a product of the edge temperature and density. The x-axis is the phase the mode is locked relative to the probe, where 0 phase would indicate the mode is aligned to the diagnostic (red/diamond probe located at 0.5 cm past the limiter, and blue/star approximately sampling LCFS).

angle between the QSH 1/5 mode and a set of magnetic coils inside MST. The QSH mode is rotated a full poloidal cycle in these experiments. The QSH metric used to filter the data was a QSH quality (Eq. 2.9) of 8 or greater. This filter ensured that only strong QSH modes would be included in the data analysis. A full poloidal rotation of the mode as controlled by the active feedback would cover one of the five toroidal periods over a diagnostic. The RMP is typically applied from t=16 to t=20 ms, for some phases locking would be difficult as the mode would drift; if needed the lock time was extended at significantly lower amplitude for 2 ms to prevent drift.

Given that the two probe locations are sufficiently far apart, it is possible to construct a pressure surface in the edge. This is shown in Figure 3.5. This Figure is produced by assuming a 5-fold period structure, aligning the phase of the pressure peaks and replicating the data over a full toroidal and poloidal grid. Each probe intercepts a different 1/5 period of the QSH edge. Assuming a 1/5 symmetry allows the probe measurements of n_e and T_e to be extended to the full surface. The presence of this edge pressure bulge indicates that the core QSH mode is able to influence the edge structure, the exact mechanism of which is unclear. The best guess of the mechanism is flux surface deformation from the QSH transition. However the combination of the ability to orient the PWI by rotating the core QSH mode and the same helicity of the structures implies the two are linked. A higher plasma flux to the limiting surfaces is possible due to the higher plasma density in the

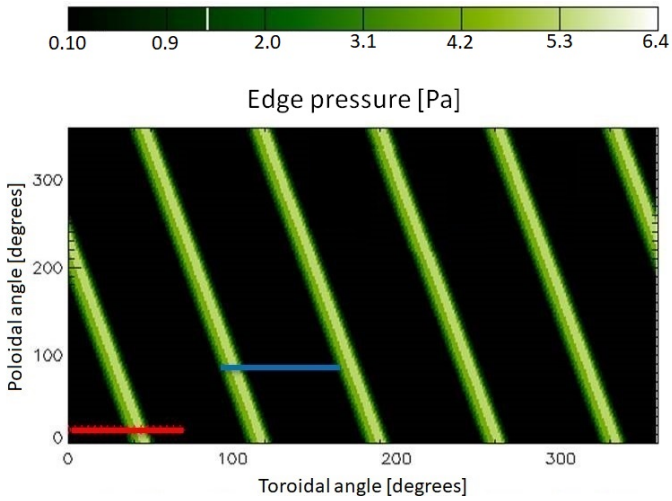

Figure 3.5: Edge pressure contours constructed based of the probe measurements, with a red bar representing the area scanned by probe 1 and blue bar for the area scanned by probe 2.

pressure bulge on the LCFS. In addition the PWI is more intense as the ions that impact the wall are higher energy. The helical plasma pressure at the edge also has implications for recycling and fueling discussed later this chapter.

The pressure surfaces are combined with V3Fit reconstructions allowing the helical pressure bulge to the plasma edge region to be represented in EIRENE models. V3Fit data for T_e and n_e extends from the center to r/a=0.94. Edge measurements were made at r/a=0.99 and 1.0. Probe measurements were appended to the V3Fit data and the intermediate data was created by a linear fit between r/a=0.94 and r/a=0.99. This combined data enables more accurate modeling of the plasma edge region. One such simulation this increases the accuracy of is the ionization of deuterium gas injected in fueling simulations discussed later in this chapter.

3.2 Properties of the QSH edge

3.2.1 Helical recycling in QSH plasmas

All measured MH plasmas show a nearly uniform distribution of plasma material interaction (PMI), both in regards of neutral recycling as well as impurity production. The rotation of the MH plasmas contributes to evenly distributing the PWI along the limiters, while the nature of the QSH plasma is to phase lock to the wall, either on its own or at as a consequence of the RMP system [24]. For the first time the magnitude of locked recycling sources are measured. The helical nature of the QSH plasma core is seen in a periodic

PWI pattern on the limiter. Despite the lower density of the QSH plasma, recycling fluxes are of similar magnitudes to MH plasmas. The deuterium source rate in the MH case is $3.8 \pm 0.3\text{x}10^{21} \frac{neutrals}{s}$ while in the QSH case it is $4.7 \pm 0.8\text{x}10^{21} \frac{neutrals}{s}$. The neutral source is 23% larger in QSH plasmas and maintains half the density as a MH plasmas. This implies either a change in recycling conditions or a decrease in the τ_p in the QSH case. Both cases are discussed below.

Images were taken of the MST edge and limiting surfaces with the boundary viewing camera system directly to obtain the D_α photon flux rate, and indirectly to obtain the neutral source rate. Knowing the photon flux Φ to the camera for a given pixel value enables the use of the $\frac{S}{XB}$ method (Section 2.3.4) in obtaining the recycling flux Γ. Camera imaging techniques measure most of the PWI interaction on the outboard limiter with near zero interaction on the inboard limiter. MST is operated in the QSH state by setting the magnetic field at the wall, $B(a)$, to be purely poloidal (F=0). Light integrated from the plasma is assumed to have been sourced at the outboard limiter, the dominant interaction site. This integration was treated as if all light in vertical slices was sourced from the central limiter element. That is, the assumption that all neutrals originate from the limiters is made. The photon fluxes measured by the full set of boundary viewing cameras around the outboard limiter is shown in Figure 3.6. This data compares the 400 kA MH plasma to its 400 kA QSH plasma counterpart. MH plasma are targeted at density of $1\text{x}10^{19}$ m^{-3} and QSH plasma at $0.5\text{x}10^{19}$ m^{-3}; nominal operating parameters for each. Data is only collected from the I_p flattop period when the plasma is in a quasi-steady state. QSH data is collected over the many phases of naturally locked MST plasma and shifted so that the first peak is centered on $\phi = 0$. The 1/5 periodicity is clearly seen in recycling flux observations of the outboard limiter, appearing as 5 peaks in the plot. The largest peak at near $\phi = 0$ exists due to an additional contribution from interaction with the poloidal gap tiles. The width of the PWI is 30 toroidal degrees in good agreement with, if not smaller than the extent of the edge pressure structure measured by probes (section 3.1). The MH state measurements are uniform around the machine with minimal variation. The decrease in the non-localized interaction that is the reduction of PWI where the helical bulge is not present supports the idea that the PWI is being reshaped by the helical state into a 3D structure.

The persistence of a QSH discharge is defined as the percent of the current flattop period a discharge has a QSH quality of Q>8 (from Equation 2.9). This condition defines that 80% of the magnetic energy is concentrated in the m/n=1/5 magnetic mode, is a sufficiently strong filter that all discharges that qualify exhibit the expected behavior of the QSH state. Discharges with Q>8 lock naturally or are able to be locked with the RMP, have a "bean shaped" magnetic core when the flux surfaces are reconstructed and produce a periodic

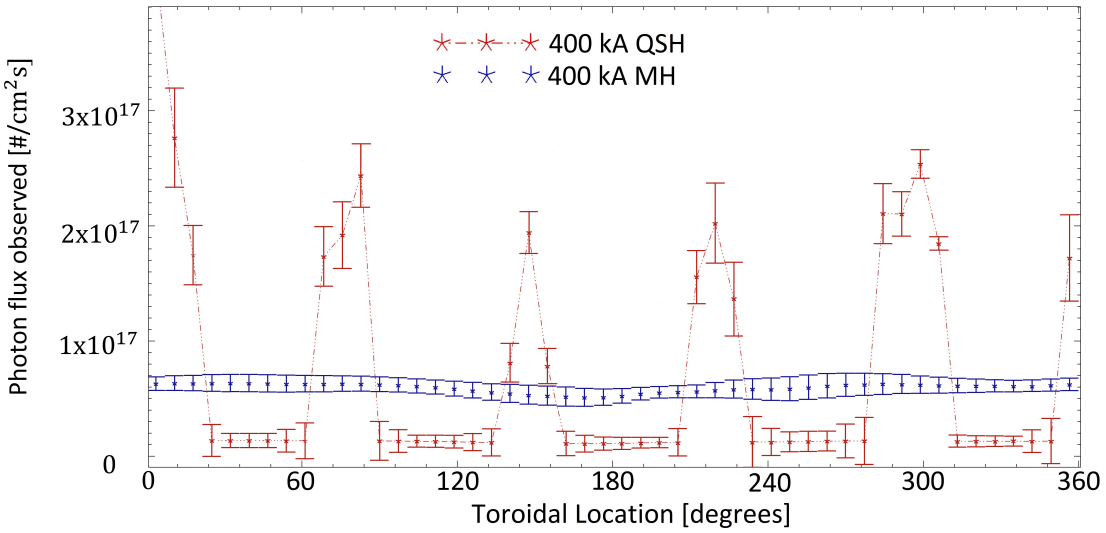

Figure 3.6: D_α photon flux as a proxy for recycling on limiters in MST in QSH (red) and MH (blue). The transition from an axisymmetric to helical RFP restructures the PWI to match the core helicity, in this case, 5 periods.

PWI on the limiter. The average of the recycling fluxes measured at the wall locations aligned and anti-aligned to the helical mode are compared over the flattop period of the discharges. A trend is seen that the discharges which stay longer in the QSH period have on average a brighter hot spot created by the locked mode and darker emission from the rest of the observed limiter. This data is shown in Figure 3.7. The rise in photon flux for locked QSH with persistence implies that the longer the QSH state exists, the more concentrated the localization becomes. The photon flux becomes more consistent frame to frame the longer the plasma stays in a single state. This suggests high-quality QSH leads to more consistent, controllable recycling from an engineering point of view. Future RFPs can then be optimized for either high-quality QSH, or high-quality MH RFPs, as the transient states between the two lead to increased variability in plasma-wall interaction.

3.2.2 Recycling properties of the QSH edge

The localization of the recycling source in QSH plasma prompted the question about the PWI conditions during localized plasma bombardment of the limiter. Experiments were conducted in MST by inserting the probes to the limiter, computing the ion flux onto the probes, and then comparing to the calculated recycling flux coming off the limiter after the probe was retracted. The recycling flux was determined by the D_α emission and

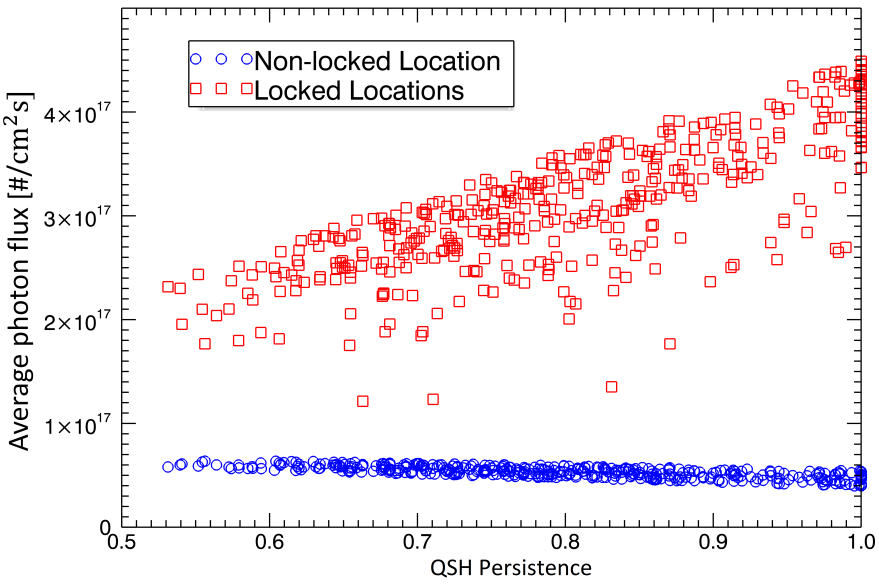

Figure 3.7: Wall recycling as measured by D_α photon flux decreases linearly, and localized locked limiter emission increases with QSH persistence.

S/XB method with the conversion factor based on probe measured plasma parameters. These measurements were during a phase scan of the QSH mode to determine if recycling conditions vary with the magnetic mode. It was found that the recycling was reduced from $90 \pm 10\%$ when the mode was not locked over the measured region to $68 \pm 4\%$ when the magnetic mode and pressure bulge were locked near the measurement region.

The probe used for this experiment was 15 poloidal degrees above the limiter or about 2.5 cm above the limiter. The plasma flux onto the probe is calculated as the product of the ion density and ion sound speed:

$$\Gamma_i = n_i * c_s \tag{3.1}$$

Otherwise stated this is the ion saturation current (Eq. 2.14) per probe area, divided by the electron charge. The results of the recycling experiment are shown in Figure 3.8.

The recycling is near unity when the edge pressure bulge is far from the probes as might be expected. The pressure bulge aligning to the probe causes a drop in the recycling observed. The measured particle flux to the limiters increases while the photon flux of D_α light remains approximately constant. In addition electron temperatures are measured. Ions are assumed to have a temperature proportional to the electron temperature in MST. Hotter ions have increased likelihood to embed themselves into the graphite limiters rather

than collide on the surface. Confinement times, τ_p, are sensitive to changes in the recycling coefficient.

The recycling was found to be high when the pressure bulge was not locked to the measuring probe. The recycling averaged R=0.9, with R=1 being within the standard error of the measurement. The region of locked PWI averaged .75 with a minimum of R=0.68. Recycling coefficients were calculated by comparing the ion flux from probe measurements to the recycling flux based on camera measurements. Error was lower in the locked case to around $\pm$0.04. The change in effective recycling is due to ion fluxes to the limiter surfaces increasing more than light emission in the presence of the pressure bulge. Higher ion fluxes to the limiters occur while the mode is locked to the edge, and while photon emission also rises in the presence of the QSH mode, the ion flux increases by a factor of 10-15, based on probe measurements of ion saturation current, while the cameras see a light intensity jump of a factor 7-10. The change in recycling coefficient can decrease the effective confinement time, τ_p^*, by a factor of 5. The effective particle confinement time,τ_p^* as shown in Equation 2.4 is strongly influenced by recycling. Taking the derivative with respect to recycling one finds

$$\frac{d\tau_p^*}{dR} = \frac{\tau_p}{(1-R)^2} \tag{3.2}$$

When R is close to 1, small changes in R produce large changes in the effective particle confinement time, τ_p^*. Gas injection experiments described in the next section are conducted to measure τ_p^*. The increasing of R from 0.75 to 0.95 increases τ_p^* by 5. What is physically happening is that as recycling approaches unity the number of cycles a particle makes in Figure 2.1 gets increasing large, leading to the effective confinement time being longer.

The change in recycling coefficient in the presence of the pressure bulge helps explain why the QSH neutral source is larger despite maintaining a lower plasma density. With reduced recycling in the pressure bulge region, more neutral particles are required to sustain the QSH plasma density.

Some potential explanations are now offered. The first case to be considered is that hotter plasma particles are less likely to cause recycling on a surface with the recycling coefficient trending away from unity towards lower values starting at 20 eV [77] [70]. Another explanation could be that the wall is locally being depleted of the deuterium reserve. Graphite has a storage capacity of about $5x10^{19}$ H per m^2 [3]. The area of the wall where PWI occurs in MH plasma is the whole limiter. The extent of the limiter is approximately 12 m (outboard circumference of MST) by 0.04 m (circumference of a 1.27 cm graphite half-round limiter tile). Having the full outboard limiter is the plasma-wetted surface leads to a larger capacity for neutrals to be used as part of wall fueling. Taking the

full area of the limiter and diving by total neutral source rate as measured by the BVCs (Section 3.3.1) estimates a wall depletion time for MH plasmas to be approximately 34 ms. This time is a third of the longest MST discharges, and it is quite reasonable to assume the ions incident on the wall will neutralize and replenish this fuel source.

The localized PWI occurs over each localized limiter "hot spot" (high neutral source) in a QSH discharge has an area of 0.15 m by 0.04 m. If one calculates the wall capacity assuming a fully loaded wall, and the whole neutral source required to sustain the plasma is from an area that represented wall tiles for each QSH hot spot, the wall reservoir would deplete in 0.32 ms if no replacement occurs. This is a worst case scenario, from Figure 3.6 the D_α light shows that recycling occurs over the whole outboard limiter, not just in the localized region. About half the total recycling occurs in the five QSH "hot spots" and the remainder of the neutral source is distributed over the rest of the limiter. Replacement of the deuterium is very likely to occur, so with the ions that knock off a deuterium neutral neutralizing on the graphite limiter themselves. It is therefore suggested that the recycling coefficient decreases when the edge pressure bulge is locked to the wall as the neutral recycling flux is limited by the availability of neutrals on the wall material, while the flux of the ions incident on the wall is determined by the plasma density and confinement of the QSH mode.

3.2.3 Phase dependence of deuterium injection

The ability to inject deuterium into a helical plasma was measured by perturbation gas injection experiments and a dependence of the effective particle confinement time on the alignment of gas source and QSH phase was found. A single injection valve was used on MST to insert a known quantity of deuterium during the QSH period. This gas valve was located at $(180\Phi, -135\theta)$. The orientation of the QSH mode was either aligned, anti-aligned, or perpendicular to the gas valve to determine the effects of plasma alignment on an injection of neutrals into QSH plasma. The smallest gas injection quantity in MST, limited by the piezoelectric valve, is 1.25×10^{19} particles over 5 ms. For these gas injection experiments , 3.75×10^{19} particles were injected during the QSH period. This was the largest amount that could be reliably injected without the plasma dithering back to an MH state. MST's interferometer was used to measure the line averaged density of the plasma in response to gas injection. The procedure described in Section 2.1.3 is used to identify the total fueling uptake, fueling efficiency, and particle confinement time for this gas injection.

The results of gas fueling in the QSH state are shown in Figure 3.9. Here the fueling efficiency is shown as a function of the locked mode relative to the gas injection valve. A phase of 0 degrees implied the gas was injected directly into the edge pressure bulge, while

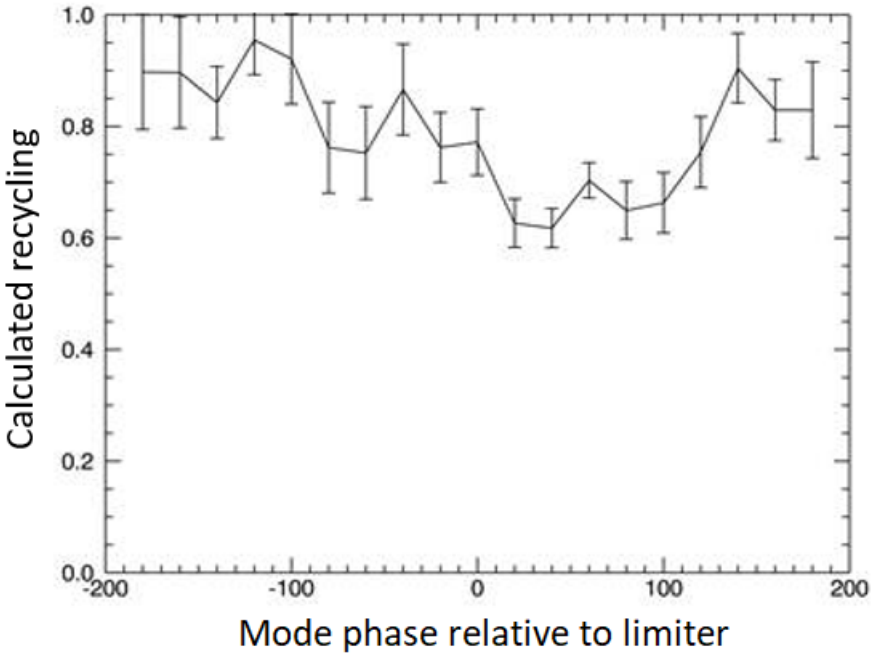

Figure 3.8: The recycling coefficient in 400-425 kA QSH plasma versus mode location in MST. The recycling coefficient decreases if the helical mode is locked near the limiter.

a phase of -180 degrees implies the bulge was poloidally opposite the gas injection valve. Error in this plot is calculated as the standard error of the density measurements, phase was assumed to be prescribed and exactly locked. Fueling efficiency of deuterium gas injected into QSH is 60% to 70% depending on the phase. The maximum fueling efficiency is seen when the mode is locked at a gas injection valve location. As the mode is locked further away from the gas injection valve, the mean fueling efficiency drops. QSH plasmas will most readily uptake fuel when gas is injected into the edge pressure bulge. This is a direct consequence of the gas injected into a region of higher temperature and density being more directly ionized and confined before the neutrals are lost to pumping or the wall. Using the probe data to compare the ionization cross-section, the $\langle \sigma v \rangle_{ei}$ increases from $0.9\text{x}10^{-14}\frac{m^3}{s}$ to $2.8\text{x}10^{-14}\frac{m^3}{s}$ in the extreme edge based on AMJUEL tabulated data[68]. An EIRENE simulation of fueling is presented later in Chapter 4 with an extended discussion of edge temperature and density effects on fueling.

τ_p^* was found to vary with respect to the phase, being significantly longer when injected gas is anti-aligned to the QSH mode. In all cases total density decays to the nominal pre-injection level after a short time. The measurements of τ_p^* vs QSH phase are shown in Figure 3.10.

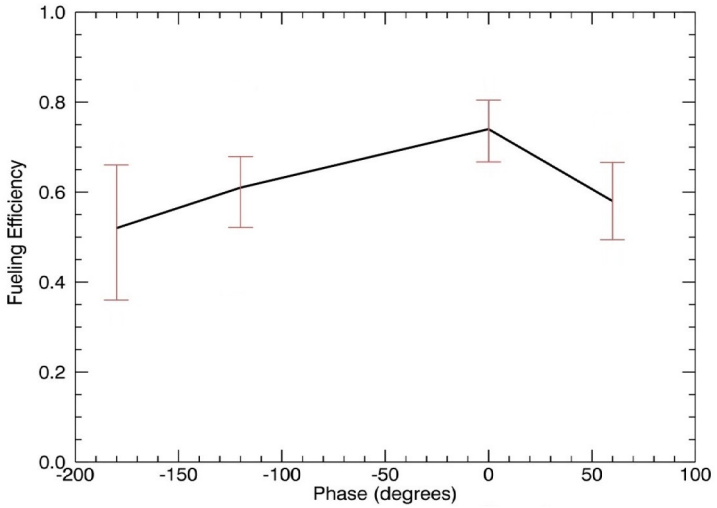

Figure 3.9: Experimental fueling efficiency measured. A phase of 0 degrees represents the QSH mode aligned in front of the gas injection valve. While the mode is aligned to the gas valve, greater fuel uptake occurs. Error bars represent the standard error of the data set.

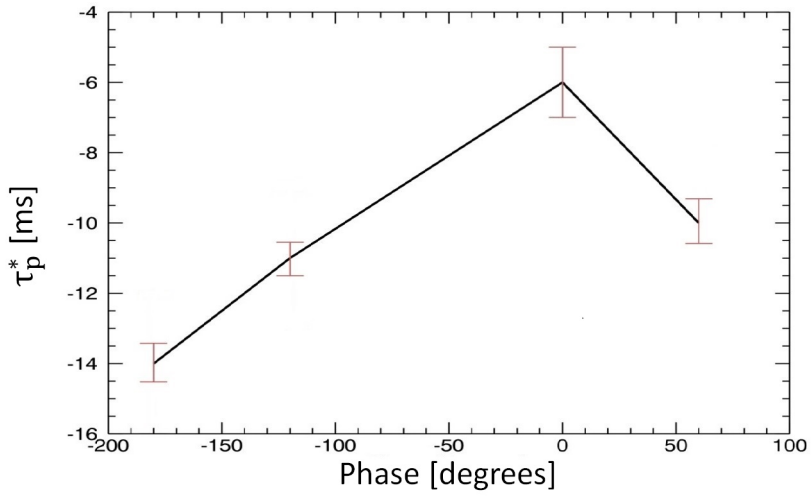

Figure 3.10: Effective confinement time as a function of the phase between the QSH mode and a valve injecting gas into the QSH plasma is measured. A phase of 0 represents the QSH mode aligned to the valve. A lower absolute value represents an increased decay rate. This rapid decay occurs when the mode is aligned to the gas injection valve, implying that the edge pressure bulge will rapidly expel plasma particles compared to the regions where the pressure bulge does not exist. Error bars represent the standard error of the data set.

The τ_p^* is calculated by observing the density decay method described in 2.1.3 The gas injected into the plasma remains longer in the system when it is injected away from the pressure bulge. A lower absolute value of τ_p^* represents a more rapid decay back to the density levels sustained by recycling, where here the negative sense of τ_p^* is a decay time constant. When the gas valve is aligned to the edge pressure bulge (0 degrees on the Figure), the additional amount of neutrals is ionized more readily. This is seen as increased fueling efficiency (Figure 3.9). These results suggest the life cycle of deuterium, recycling on the walls, is much shorter when the recycling source is near the edge pressure bulge. This has implications for the plasma energy budget, as will be discussed later in Chapter 4 with the modeling results.

The effectiveness of wall fueling was also investigated. Experiments were performed in which MST underwent 30 minutes of pulsed-discharge cleaning (PDC), then gas injection experiments were repeated at various phases. The results of these experiments are shown in Figure 3.11. In the Figure, the red horizontal lines represent the average τ_p^* from when the walls were assumed to be saturated. Four separate cleaning cycles were used. After each round of cleaning the τ_p^* were on the order of 1 ms, showing that clean walls effectively pumped deuterium , that is the wall recycling was low. This is evident in rounds 1 and 3, and to a lesser extent in round 2. The particle confinement times started at around half the average from the previous gas injection experiments, and decreased to 2.1 ms, then immediately jumped to a nominal value of around 9 ms. This is within the error bars of the previous experiments. This set of experiments implies that MST's walls saturate with neutral particles rapidly after deuterium plasmas are discharged.

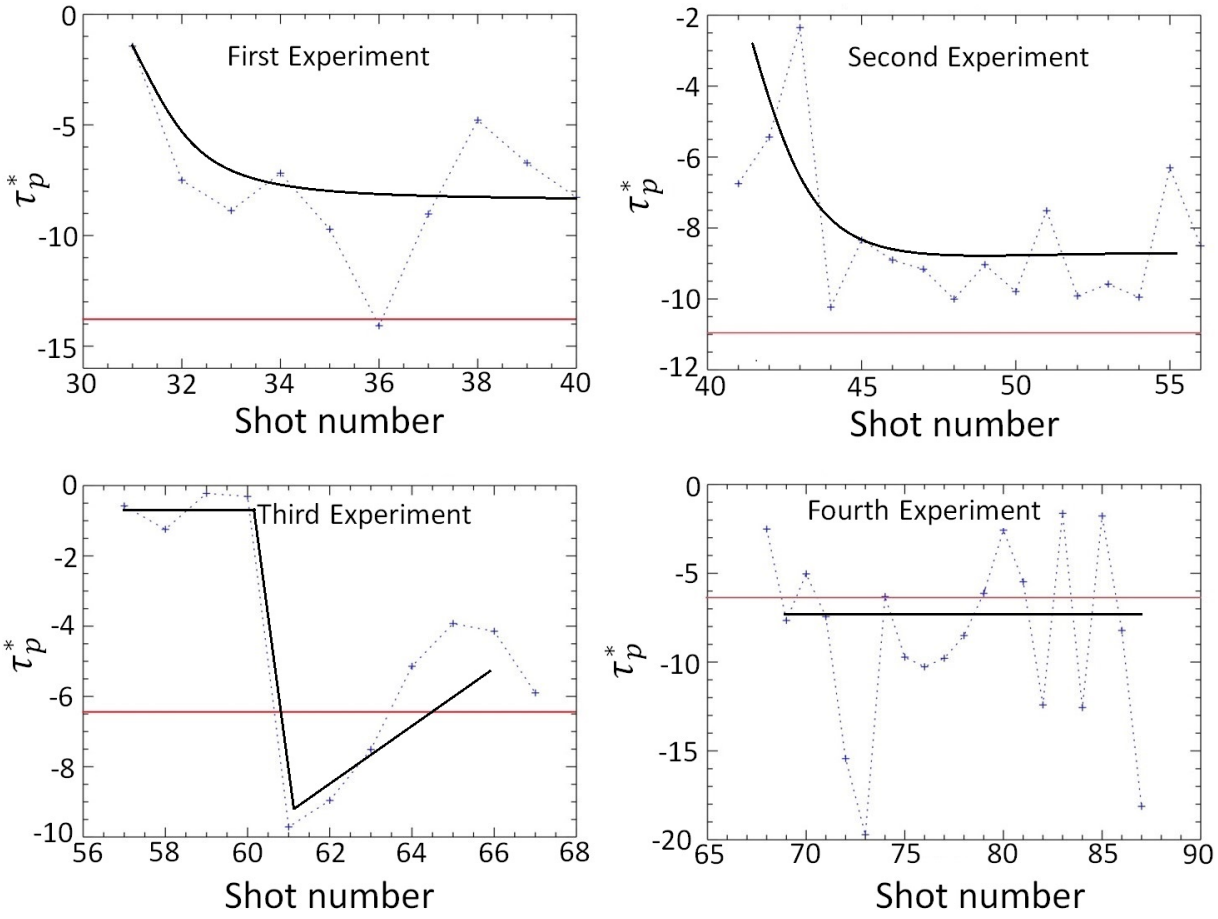

Figure 3.11: The walls of MST become rapidly saturated with deuterium during normal plasma operation. Only after 3-6 discharges from cleaning do recycling levels return to nominal values as depicted by the red horizontal lines. Black lines are added to guide the eye to the trend of the data in each plot.

3.3 General survey of the plasma boundary

3.3.1 Neutral source spatial distribution in MH plasma

The investigation of the recycling fluxes discussed before is now followed up with a more general survey of the plasma edge properties in the configurations in question for this thesis. The general properties discussed in this Section will be the source spatial distribution in both MH and QSH plasmas, the effect of reversal parameter, F, on recycling rates in the RFP, an impurity generation in MST, and bolomteric power measurements in MH and QSH plasmas.

In MH plasmas, the degree of symmetry in PWI increases with increasing plasma current. For each camera view, a reference image was prepared where toroidally localized features are identified, enabling the extent of the limiter viewed by the cameras to be identified. The data images then have a region of interest drawn about the outboard limiter, and this region is sliced toroidally. An image with an overlaid region of interest over the outboard limiter's local emission is shown in Figure 3.12. In this image, a sample of the high toroidal angle area of MST is shown, from 270 to 360 toroidal, left to right over the image. The red region is generated by fitting a box around the brightest pixels of the image. The light blue ellipsoid is done by best fitting an ellipse to the contours of the image boundary. The red region is identified as the limiter for classification and data handling, and the light blue region is taken to be the observed outboard area. The samples observe the poloidal gap region but are representative of the process from any of the views. A ripple band-like pattern can be seen in the 200 kA case. The toroidal distribution of photon flux at four time steps from within a single discharge is shown in Figure 3.13. At lower currents a structure exists with rotating peaks and troughs in the amount of light emitted near the limiter.

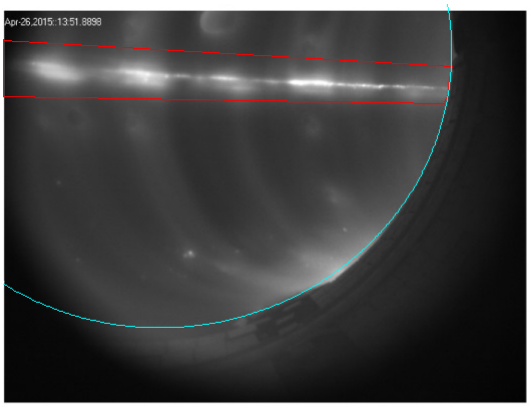

Figure 3.12: D_α filtered image from camera 1, looking past the poloidal gap to the 270-360T region in a 200 kA plasma discharge (1150426036:30ms). Overlaid on the image are two regions of interest used to slice up the image for processing. Inside the blue circle is the full plasma observed in the image, inside the red box is a zone of "limiter emission". The red region of interest is further divided into toroidal slices.

The 200 kA MH data in Figure 3.13 is from a single discharge, this spatial distribution has significant peaks with a peak-to-peak distance of $12\pm2°$. This structure of peaks and troughs changing position between images is often observed in low current MH plasma. When averaging the data between shots, this trend is washed out, as the peaks rotate, and every image captures them at a different time. The 500 kA MH data in Figure 3.14 is from discharge 1140811080. Unlike at lower currents the spatial location of peaks does not

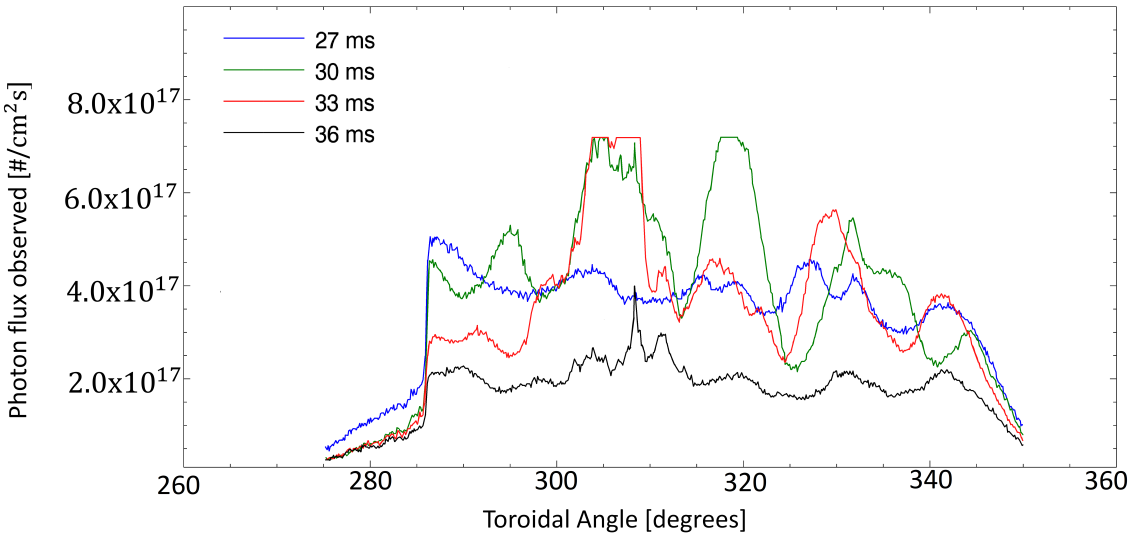

Figure 3.13: D_α emission for 200 kA plasma from a single camera view; discharge 1150426036:30ms. Clipping in the image is due to a momentary saturation of the pixels.

change with time. A single peak location around 295° is seen. This spike is caused by a nearby porthole. With the exception of the peak the rest of the data from 310° to 350° is flat in spatial distribution within images and the image to image variation is also small with the exception of the 30 ms trace which has a 20-50% rise. The uniformity between the 27, 33, 36 ms frames are characteristic of the plasma flattop of a high current MH plasma.

These plasmas were all rotating MH plasmas at high current, so plasma locking to a location is likely to not influence the PWI. The peaked location in the frames may be a consequence of a break in the edge symmetry by diagnostic portholes. At this location MST has two standard diagnostic ports just above and below the limiter every 15° toroidal degrees from 300° to 345°, but noting within 30° poloidal of the limiter from 300° to 270°.

Higher currents result in lower D_α fluxes measured. The reduced D_α fluxes measured is indicative of improved confinement with higher plasma current, consistent with past results [81]. There is also a breaking in the symmetry, caused by the poloidal gap. At this location increased intensity is observed in D_α light measured. The trend in MST is that the overall D_α emission slightly decreases as the toroidal angle from the gap increases. The overall magnitude of symmetry breaking is approximately a factor of 2, more substantial at lower currents. This binned data is later used, when calibrated to provide absolute values of recycling sources, for EIRENE simulations for MH plasmas. The time traces of recycling

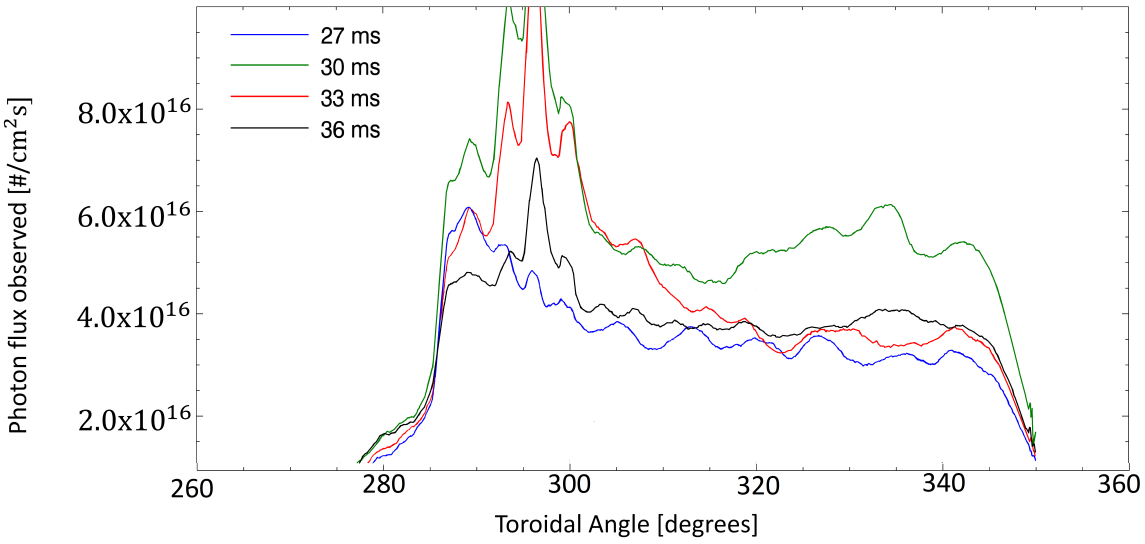

Figure 3.14: D_α emission for 500 kA plasma, discharge 1140811080:30ms. Emission peaks and troughs do not change relative location, single camera view.

around MST for 200 and 400 kA MH plasmas are shown in Figures 3.15 and 3.16. Photon emission decreasing with discharge length is seen in both cases. The decrease occurs as no fuel is injected into the plasma beyond the initial startup fueling, and some for softening the termination. The recycling can vary around MST by up to a factor of two but is often more uniform, and less peaked. The most significant difference is between the views looking at the poloidal gap and those looking far from the poloidal gap.

The data is more readily usable when examining just the I_p flattop period when plasma conditions are steady. The photon flux spatial distribution about the machine is presented in Figure 3.17. This data is presented as 1σ confidence intervals for Φ. This confidence interval is calculated as:

$$\bar{x} - z\frac{\sigma}{\sqrt{n}}; \bar{x} + z\frac{\sigma}{\sqrt{n}} \tag{3.3}$$

Where $\bar{x}$ is the mean of data collected at a given location, z is a statistical function chosen for a given confidence level in this case z=1.645 for 90% confidence in the data range. σ is the sample standard deviation, and n is the number of sample points collected. Data is represented this way to show the consistency in measurements over a range of plasma currents for MH plasma. The mean of this data forms the source rates for MH plasma in EIRENE. In addition, this Figure includes the variation of the photon flux due to changes in plasma current. The lower current plasma produces both a higher photon flux and higher

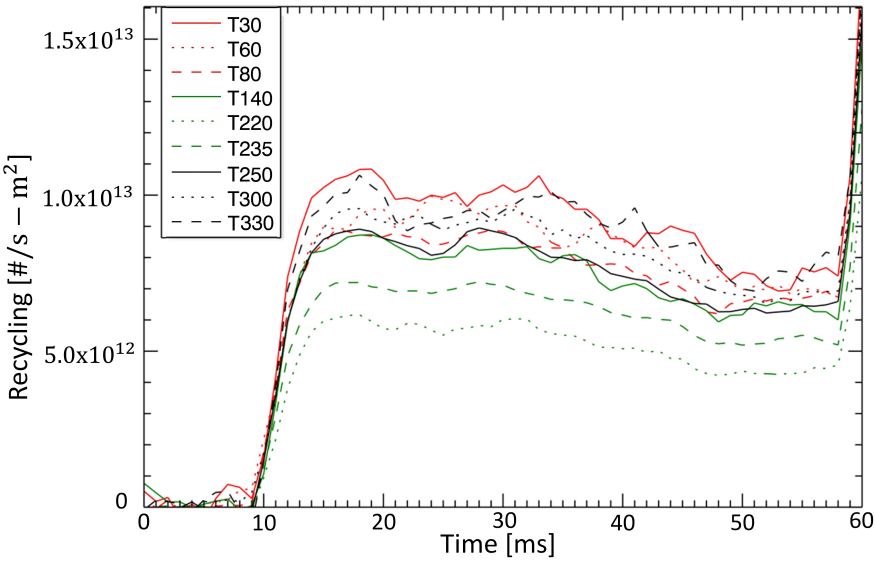

Figure 3.15: The average recycling flux from a 200-kA standard discharge, showing small toroidal variation. Plasma flattop exists from around 20 to 40 ms, then the current decreases until the discharge is terminated resulting in the peak flux at the end of the trace.

recycling flux, as well as larger shot-to-shot variation.

Low current plasmas have a greater standard deviation in photon fluxes measured. This is a frame to frame variation in low current plasma from the motion of the rotating PWI. In MH plasma, the location of the maxima and minima recycling regions diminishes, becoming uniform when summed over many discharges. Higher current plasma creates a uniform PWI. Peaks in the PWI are no longer observed.

3.3.2 Dependence on reversal parameter

The reversal parameter, $F = \frac{B_T(a)}{\langle B_T \rangle}$ was investigated as a control parameter for edge phenomena. The reversal parameter is a measure of the twisting of the magnetic field at the edge. In standard (F=-0.2) or deep reversal (F<-0.2), the magnetic spectrum is broad. MH plasma composes this section of parameter space. The spectrum narrows as F approaches 0, where the spontaneous transition to QSH readily occurs. Island chains exist on the reversal surface. As the reversal surface is driven deeper by adjusting the edge toroidal magnetic field, these island chains move deeper into the plasma [78] [79]. An F-scan was done over reversal parameters from -0.3 to 0.0 on MST to study how this parameter affects total recycling in the edge of MH plasma. The same image analysis routine from the last section

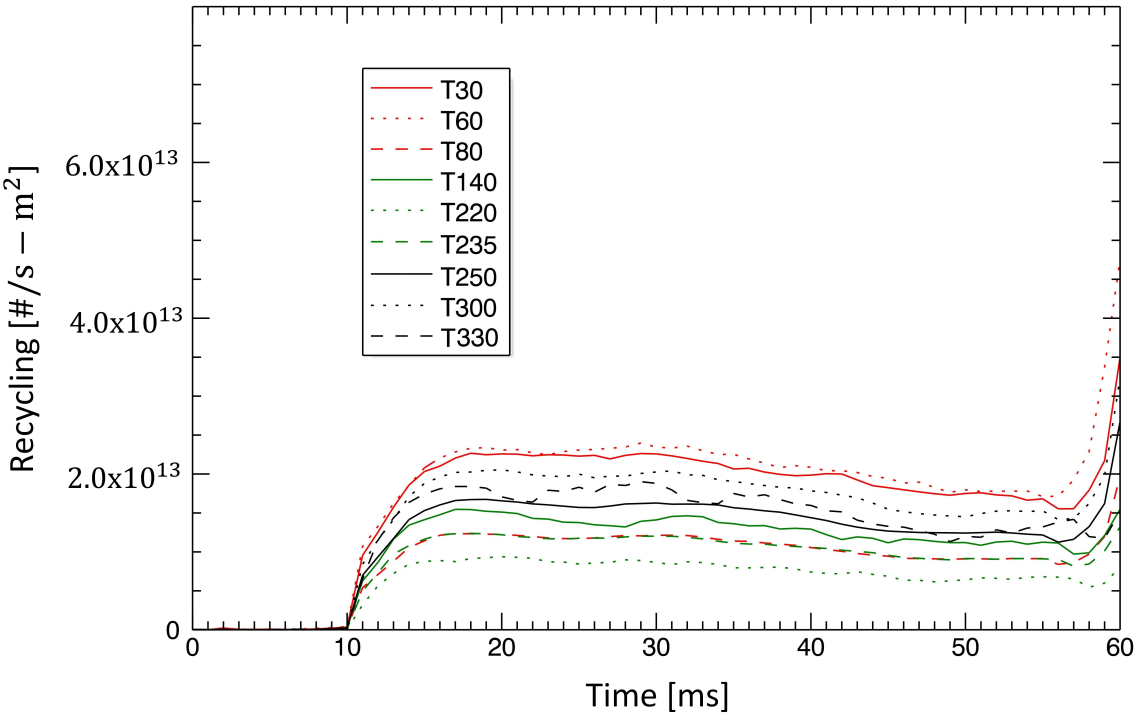

Figure 3.16: The average recycling flux during a 400-kA standard discharge, showing small toroidal variation.

is used. A graphical summary of the results is presented in Figure 3.18. Each data point represents the mean and standard deviation of the average photon flux during the flattop period of MST discharges. These experiments are performed between 200 kA and 500 kA with images used from when the plasma current was with in 10% of the target plasma current. The camera frame rate enables no more than 5 similar images to be collected from a single discharge. Two hundred discharges were used for each current level.

The maximum photon flux is observed at F=-0.2 in all cases. At deeper reversal, the plasma experiences higher confinement, but also stronger sawteeth [80]. These sawteeth expel core plasma and flatten the temperature profile briefly. It may be that the fewer, larger, sawteeth are not captured by the cameras effectively for deeply reversed plasma. The fact that the photon flux is most intense at F=-0.2 can be explained in terms of the plasma temperature. Previous studies examining core confinement showed that electron temperature is largest at F=-0.2. As the F values moves away from F=-0.2 the temperature is found to decrease [81]. The electron temperature also scales positively with plasma current as shown previously in Table 1.1. The highest temperature (and plasma currents)

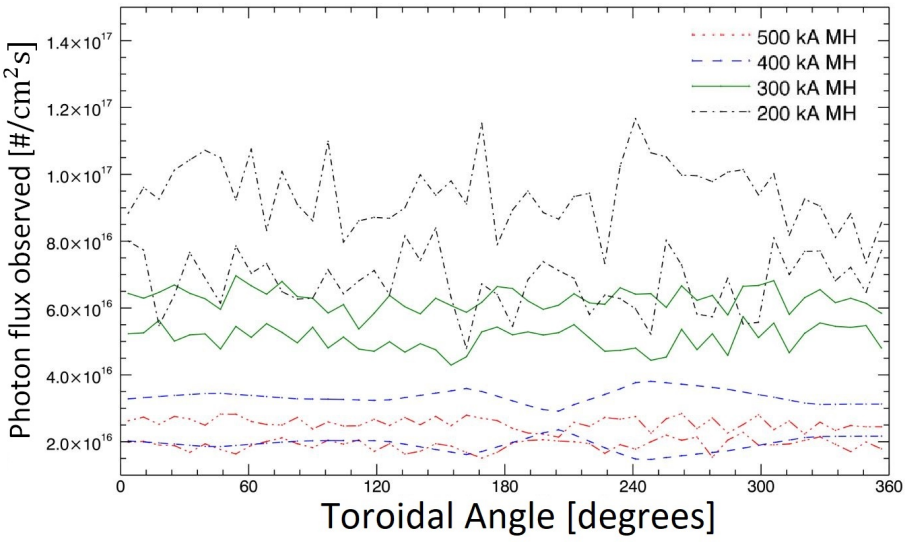

Figure 3.17: The photon flux observed for MH plasma decreases with plasma current. Each current is plotted as a set of two traces representing the mean plus one standard deviation and the mean minus one standard deviation for the observed angle. The flux tends to decrease as these higher current discharges are more uniform in the recycling and PWI.

produce the lowest photon fluxes measured. The drive for edge recycling in MST is the location of the reversal surface in MH plasma. As the reversal surface is moved away from the wall the photon flux slowly rises. The size of the islands is kept small by the shear of the q-profile. The usual size of the (0,n) island on MST is on the order of a 1.0-2.0 cm. The ion gyroradius can extend this distance another 0.5-1.0 cm for a total potential distance where the limiter is still connected to the reversal surface of 3cm. The reversal surface at F=-0.2 is located at 4.2 cm beyond the limiter (at r=46.5 based on MSTFit q-profile zero crossings). This implies the largest volume of plasma is connected to the wall when F=-0.2. So, the plasma that is connected to the wall is increasing as F is decreased until the point where the reversal surface and its associated island disconnects when observed photon flux reaches their minimum levels. The F=0 parameter is an outlier at higher currents, with a steeper decrease between F=0 and F=-0.05 when compared to 200 and 300 kA. At higher currents, these plasmas tend to evolve naturally into the QSH state. The data presented for the 400 and 500 kA F=0 points was not filtered with respect to QSH or MH magnetic structure and contained both kinds of plasma, as well as shots which flipped between the two states. If it were not for F=-0.2 plasma producing routinely hotter electrons in MST plasma, it might be advantageous to operate MST regularly at shallower or deeper reversal

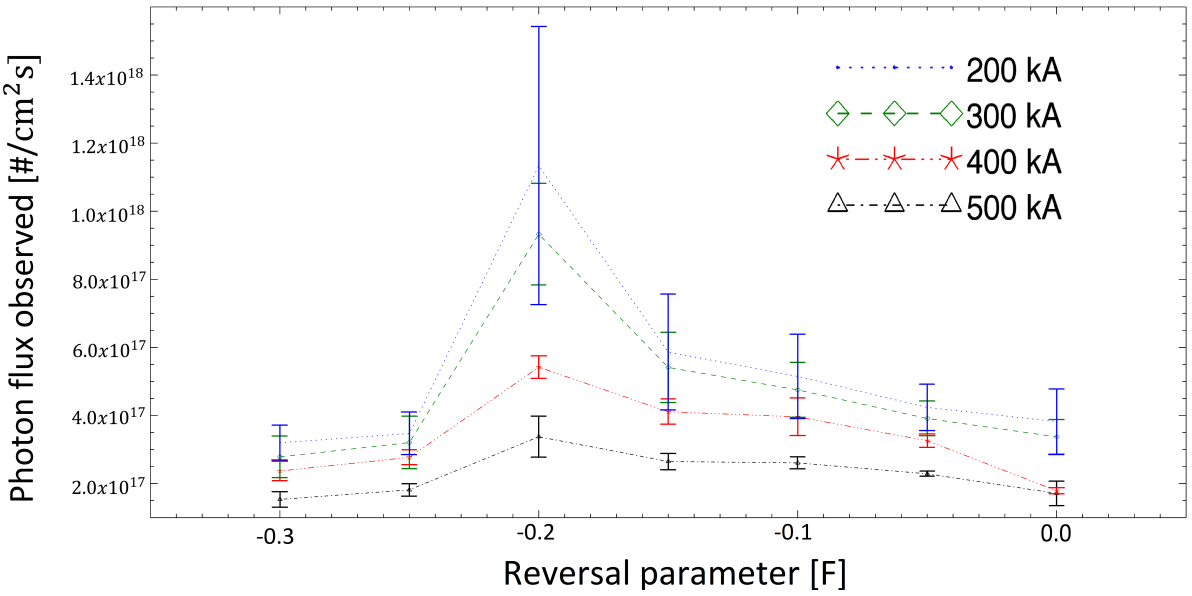

Figure 3.18: Photon flux observed on the limiters of MH plasma as the reversal parameter is scanned. Peak emission is at F=-0.2 and falls off either direction.

to minimize the PWI and maintain a cleaner machine.

3.3.3 Impurity content

One of the original goals of the BVCs was to be an impurity monitoring system on MST. A survey of impurities in MST was conducted with the BVCs. The suspected impurities were carbon, from the limiter blocks, oxygen, from water vapor in the vacuum chamber, boron, from probe housing erosion; and aluminum from the interior vacuum vessel. There were three goals of the impurity surveys. First was to evaluate if the cameras could measure the impurity content in MST. Second was to identify the impurity production locations on the plasma-facing surfaces. Third was to determine what fraction of visible light results from emission by deuterium. While surveying the plasma multiple emission lines may overlap, which can cause confusion in some cases. When a line was observed in the filtered survey, the element was identified by searching for other lines from different charge states of that atom. For example, CIII overlaps with AlII. When light was observed in the 464 nm bandpass filter, it was identified as carbon because of the presence of the CV line near 494 nm, while no other lines that could be attributed to aluminum states were observed.

The relative magnitude of the impurities was also identified. Filtered camera images

were taken with the BVCs and image intensity was corrected for transmission loss of the bandpass filters as described in Section 2.2.4. Due to relatively low content and short integration times, observation of higher charge state impurities was inconsistent. Frequently camera images filtered in light other than the major deuterium lines of 656.3 nm and 486.1 nm resulted in no data above the noise level of the camera. However, some emission from impurities were observed, such as CIII.

The composition of visible emission from MST plasma was analyzed. The plasma emission observed is primarily deuterium from the D_α line. Some oxygen emission is observed during plasma startup. This is caused by the PWI releasing gettered oxygen. The oxygen signal is not detectable beyond the plasma formation period. CIII is observed throughout the discharge. The breakdown of the light seen within the BVCs view is shown in Figure 3.19 for a 200 kA MH plasma. The data in the Figure are plotted on a log scale; otherwise, impurity light sources would be too low to be seen in detail. Error bars are not shown on the impurity species or D_α for ease of viewing. Typical errors for most impurity signals were 20-30% of the mean measurement. Comparing the trace of the visible photon counts seen in the camera to the D_α counts it is obvious that almost all of the light observable in the visible spectrum is produced by deuterium as D_α and D_β. Carbon light makes up 1-3% of the total light observed. Other impurities were found to be below the noise level of the camera detector. The 500 kA data for D_α,D_β, and D_γ lines indicate a higher plasma temperature based on the increased ratio between D_β line and the other lines. This data highlights the use of the BVCs as a survey system for MST plasmas. While the capability to monitor carbon sources exist, the spatial resolution, one of the BVCs strengths, would need to be traded for longer integration time even to begin to measure other impurities.

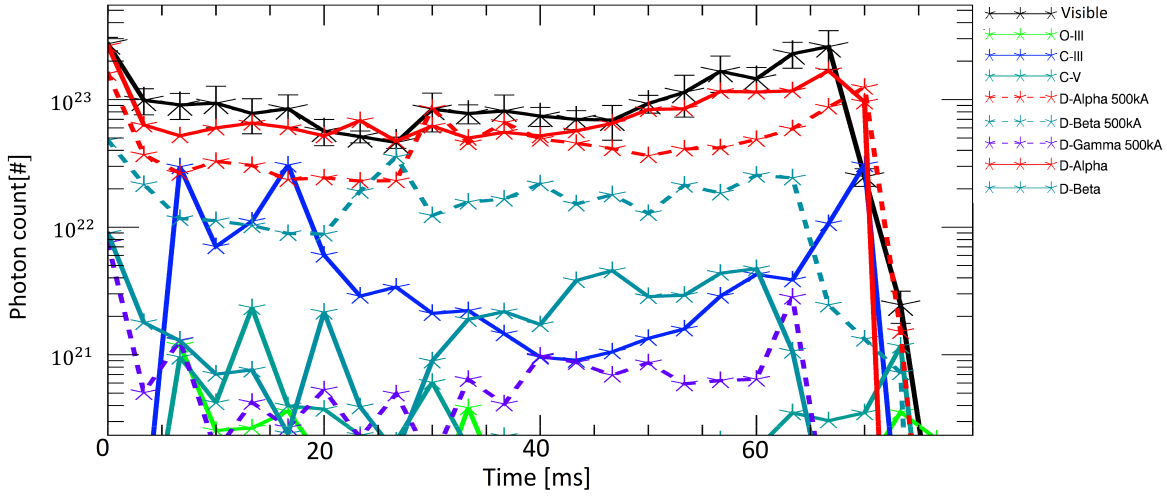

Figure 3.19: The boundary viewing camera used as a survey spectrometer. Data is taken over many discharges looking at the poloidal gap. Error bars for the visible are present, error bars for other impurity species are on order of 20-50% and have been removed to prevent clutter. The data in the Figure are plotted on a log scale.

3.4 Bolometer observation of plasma edge

Radiative power flux measurements were made with a set of bolometers. The system consists of four bolometers mounted on the exterior vacuum vessel described in 2.2.7. Bolometers are mounted to observe chords that intersect just above or below the limiters by 2 cm. A phase scan was performed using the MST active feedback system to lock the QSH mode at a given angle for a set of shots recording the power levels observed by the bolometers. After collecting 20 discharges per shot, the phase of the QSH mode was rotated and data collection repeated. Data was collected every 20 poloidal degrees for a full period of the QSH mode. The results of bolometer observation of 400 kA QSH plasmas are shown in Figure 3.20. The Figure panels are labeled with the bolometer locations in terms of MST machine coordinates ϕ, θ. The bolometers at $\phi = 30, \theta = -15$ (a), and $\phi = 30, \theta = 165$ (c) are located on the outboard and inboard of the machine respectively, observing slightly off the midplane. The bolometer at $\phi = 120, \theta = 105$ (b) measures a chord of plasma 15 degrees off-vertical. The bolometer at $\phi = 300, \theta = 135$ (d) views a chord that runs 45 degrees to the vertical. The data is adjusted such that the QSH locking phase shown in the Figure is 0 when the locked mode would be locked in front of the bolometers.

The outboard and inboard bolometers have clear peaks shown in subfigure (a) and (c).

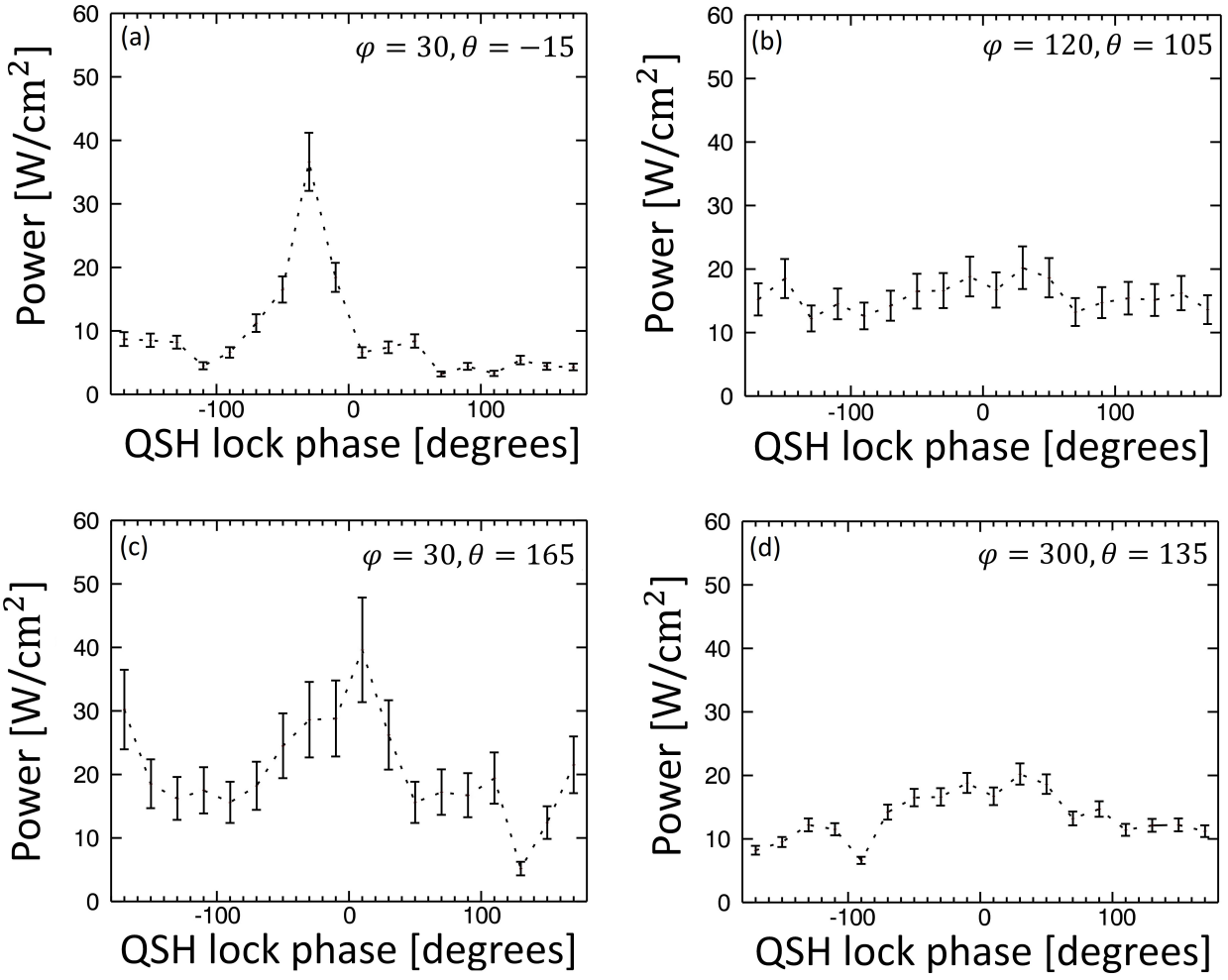

Figure 3.20: Bolometer observations of the 400 kA QSH edge along four different chords measure the total power seen by the bolometer, both photon and neutral particle, as a function of the mode relative locking phase.

The outboard bolometer has a peak shifted at -40 from the locking angle, as well as slightly elevated power levels detected in the 0-30 region compares to the 30-180 region. This large peak in P measured is from PWI on the gap limiter located at -30 degrees relative to the detector location providing an additional recycling surface for neutral generation. The signal is weakest at ± 100 degrees, when the mode is perpendicular to this detector. A factor of 2 increase is measured when the mode is locked opposite the bolometer, on the inboard limiter. The inboard bolometer measures increased power flux both when the mode is aligned to the bolometer, and when the mode is opposite the bolometer, locked 180 degrees away on the outbaord. Again this detector sees a minimum in power flux when the mode is perpendicular to the detector. The detectors at $\phi = 120, \theta = 105$ and $\phi = 300, \theta = 135$ have

less well defined peaks. The data collected by the near-vertical bolometer is essentially flat when the standard error of the measurements is considered. Peak values at 0 degree locking angle and minimums at $\pm$100 when the mode is perpendicular are seen by the two detectors. Without a strong neutral source from PWI this bolometer observes small values of the power flux as the mode is rotated.

The energy losses from the neutrals, like the plasma pressure, mimic the QSH core magnetic structure. It is evident in Figure 3.20 (a) and (c) that the chords across the midplane measure peaks when the QSH mode is locked near the bolometer. Vertical chords (b) and (d) are flat. This implies increased plasma neutral interaction in the midplane when the mode is locked outboard, but not inboard or otherwise. These measurements imply that the plasma-neutral losses are concentrated in the plasma edge pressure bulge, but must have some spread over the plasma volume in order for the vertical detector to be measuring a signal.

Experiments were also performed to measure the radiated power fluxes of MH plasmas. As MH plasmas rotate the phase is rapidly changing. As a result the value presented is the phase of the rotating m/n=1/5 mode at the time of peak current. The power fluxes collected are instantaneous measurements of the power seen at peak current in a MH plasma rather than multiple shot averaged values as the QSH data was. The data was collected with the same four bolometers as before, inboard (a), outboard (c), vertical (b) and 45-degree angled (d) and is presented in Figure 3.21. Bolometer power levels measured by the outboard detector are consistent. The other bolometers have larger spreads in the observed power fluxes. All bolometers occasionally measure lower power levels, sometimes 0. No dependence on phase is observed as is expected for a rotating mode. Power flux in MH plasmas is independent of the m/n=1/5 mode phase. There is no structure in the radiation distribution of MH plasmas, while a strong structure linked to the core magnetic mode is seen in QSH plasmas.

The plasma edge of MH plasma is, on average, symmetric with no noticeable poloidal or toroidal dependency. This is supported by both camera measurements of recycling fluxes and bolometer measurement of neutral power fluxes. Bolometer measurements add additional evidence to support that the plasma edge of the QSH plasma is indeed 3-D with both poloidal and toroidal asymmetry. Bolometers see that the largest power fluxes are see when the QSH mode is locked close to the outboard limiter. This is seen by both inboard and outboard bolometers looking across the midplane. While the QSH mode is locked inboard, a small increase to the power measured is observed. Bolometer that look vertically through the plasma do not observe significant changes in power measured in either MH or QSH case as these bolometers do not measure near the primary locations of PWI.

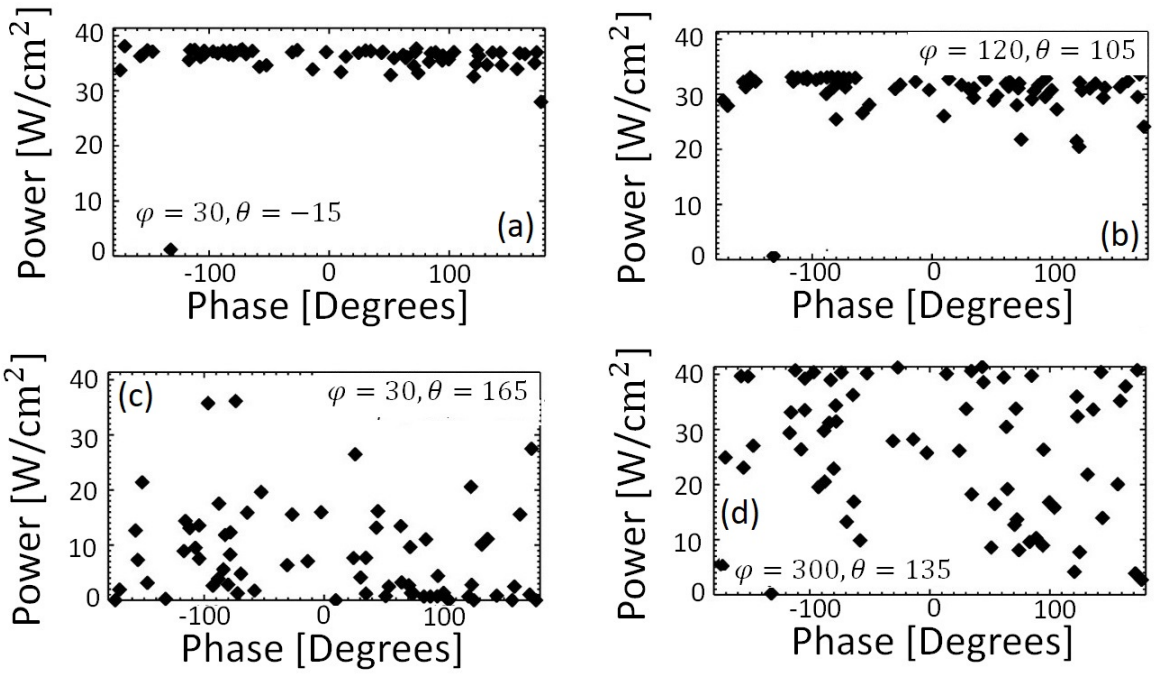

Figure 3.21: Bolometer observations of the 400 kA MH edge along four different chords measure the power losses. Both photon and neutral particle power losses are measured. Results are displayed as a function of QSH phase.

Chapter 4

Numerical analysis of the 3D neutral particle distribution and associated power losses

The EIRENE code is used to model the MST edge and reconstruct the 3D neutral distribution. Plasma backgrounds are created utilizing the edge data measured from probe experiments. Neutral sources are defined by converting photon fluxes measured by the Boundary Viewing Cameras (BVCs) into recycling fluxes, which in turn depend on plasma parameters in the edge. A procedure was developed to adjust the EIRENE models to maximize agreement between generated synthetic images or synthetic line integrated signals and experimental data. In the model, recycling on surfaces as well as the distribution of the neutral source were used as free parameters. Once the model is tuned to produce synthetic signals that agree with experimental measurements, the neutral density profile and the plasma-neutral interactions are examined in detail.

4.1 Plasma backgrounds in the model

The code V3Fit, together with measurements, is used to create 3D equilibrium reconstructions based on well-diagnosed plasma discharges. The reconstructions are used as a Quasi-Single Helicity (QSH) plasma background. A 1/5 symmetry in the magnetic structure is enforced in these reconstructions by zeroing out other magnetic modes to produce a pure helical structure. The data at the edge of these reconstructions tends to be axisymmetric due to the ideal conducting boundary conditions in V3Fit. This data is shown in Figure 4.1, which is composed of four plots, showing electron temperature and density in two cross sections of a QSH plasma, 0 and 36 degrees. These cross sections are chosen as they represent an inboard and outboard lock. B_r is forced to 0 at the edge, a consequence of the conducting boundary which forces the flux surfaces at the edge in V3Fit to be circular. Consequently the temperature and density in the edge is circular and uniform.

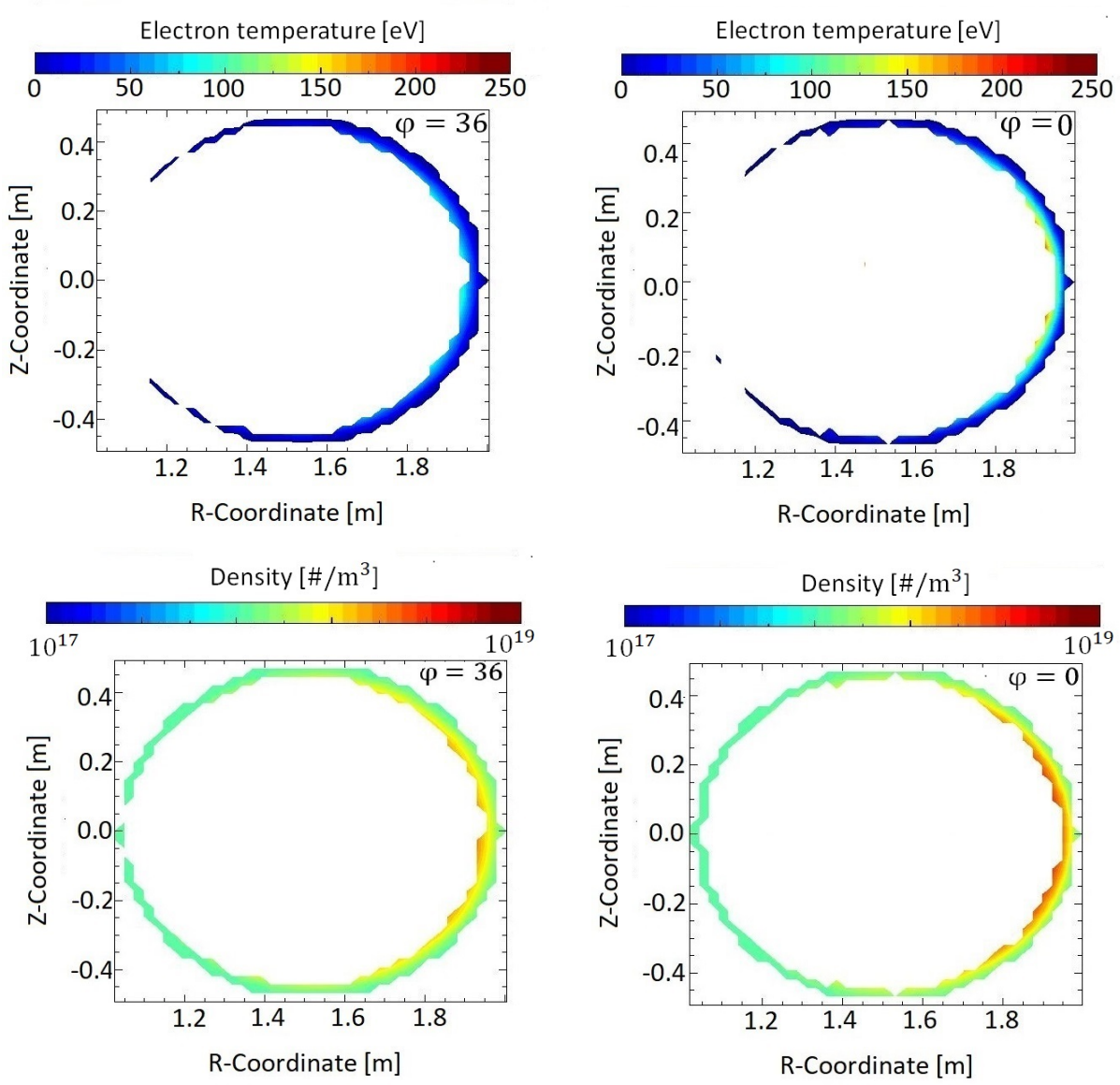

Figure 4.1: Plasma background fields from V3Fit for 400 kA QSH are shown. The x-axis the R coordinate and the y-axis the Z coordinate in MST. Plasma density and temperature cross-sections are shown for the locked mode cross-section as well as the anti-locked mode cross-section. The plasmas represented in the right two plots are locked outboard (right), and the plasmas represented by the left two plots are locked inboard (left). The edge values are uniform around the machine poloidally as well as toroidally at the two cross-sections shown which represent the two extremes of the QSH mode.

The default V3Fit data does not have the helical deformation observed by the Langmuir probe discussed in Chapter 3. The central data points have been removed for clarity, and data from r/a>0.94 is shown. Due to the Shafranov shift, the flux surfaces are shifted outboard slightly. Visually, data is lost on the inboard side when filtering on data at r/a > 0.94 . The parameters on the outer edge of these plasmas are uniform both poloidally and toroidally at approximately 40 eV and $3.8\text{x}10^{17} m^{-3}$. There is no dependence on the orientation of the QSH mode in this data; the edge in front of the limiter is the same temperature and density regardless of the QSH locking angle.

Therefore V3Fit reconstructions were augmented by appending and blending the probe data into the edge of the V3Fit data. Probe data replaced V3Fit data in the outermost 2 radial rings. In order to obtain a smoother temperature and density profile in the edge, the region from r/a=0.95 to the outermost cell is altered to produce a linear fit between the r/a=0.95 and the edge cell. The plasma temperature is shown in Figures 4.2 and 4.3. Plasma density is shown in Figure 4.4. The corrected V3Fit background cross-sections are shown in Figures 4.3 and 4.4. These full background Figures are useful to understand what interactions can be expected between the neutrals and bulk plasma. Detailed edge measurements which have been incorporated into the model are shown in Figure 4.2. In this Figure where central data is omitted, the boundary is at r/a=0.94 to highlight the region where V3Fit and edge data are blended together. This Figure highlights the edge region, where neutrals are sourced. Examining this Figure highlights how plasma-neutral interactions can change with edge conditions.

The edge data is most easily seen in Figure 4.2, where the central data is removed. The outboard edge starts at 58 eV and quickly rises to over 100 eV in less than 2cm as shown in Figure 4.2 (a). On the inboard side, a cold 20 eV plasma exists in the region 3 cm from the wall. The mode is locked inboard, and the edge plasma is symmetric about the machine at 25-35 eV as shown in Figure 4.2 (b). This uniformity in the edge arises because when the mode is locked inboard the Shafranov shift of the plasma keeps the core mode from pushing up against the inboard limiter. When the mode is locked perpendicularly to a limiter, the poloidal dependence on edge temperature is seen in the lower outboard corner as shown in Figure 4.2 (c). This region has temperatures at 50-80 eV while the upper-inboard region is below 40 eV. Plasma in front of the limiter is 40 eV. When the QSH helix is locked close to the limiter the neutrals encounter a hot dense edge. Similarly, in the locked case, the neutrals will encounter plasma of 140-200 eV after traveling 2.5-5 cm. As the neutral source is predominantly the outboard limiter this leads to strong dependence on the mode phase. Charge exchange does not differ by more than a factor of 3 between 10 eV and 100 eV, while the breakdown and ionization of neutral deuterium changes dramatically.

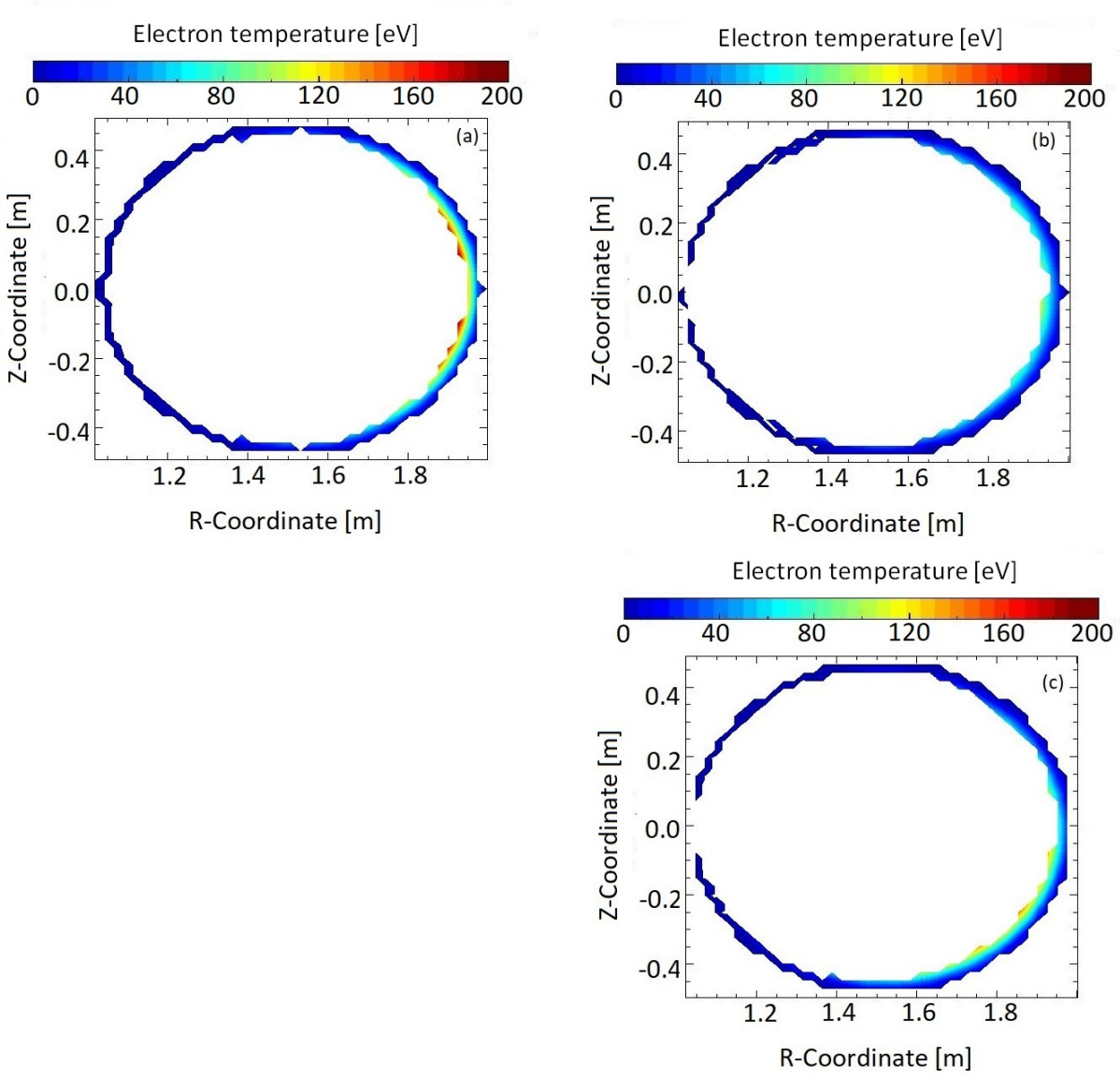

Figure 4.2: Combined electron temperature backgrounds of V3Fit and probe data for QSH plasma with only edge data shown to highlight probe results. Three separate toroidal slices are shown, representing (a) an outboard lock $\phi = 0$, (b) an inboard lock $\phi = 36$, and (c) a perpendicular lock $\phi = 50$.

At 10 eV it is 100x more likely for a neutral molecule to be broken down into two atoms of deuterium than dissociatively ionize. At 100 eV these two methods of breaking down molecular deuterium have approximately the same reaction rates. As molecular neutrals break down into a neutral and an ion, the ion becomes magnetized and the penetration of the fuel into the plasma is decreased. As most neutrals are generated as molecules from the PWI of the helical bulge and the limiter, dissociation ionization is the most common process in the QSH plasma. This will limit the penetration of neutrals through the edge plasma.

The nominal 400 kA QSH temperature data used in EIRENE is shown in Figure 4.3. Cross-sections of the mode are shown in the locked, anti-locked, and a downward perpendicular locked position, each relative to the outboard limiter. The temperature data in this Figure has a poloidal dependence. The highest-temperature region of the helical QSH core exists at r/a=0.69-0.77 when locked outboard. The outboard locked case (a) creates an interesting scenario. Neutral particles generated from PWI on the limiter can reach 400 eV plasma within a few mean free paths. EIRENE recalculates the mean free path of neutrals each time a new cell is entered to determine the chance of interaction within the new cell. Two temperature breakpoints are worth examining to understand which reactions are likely to occur when modeling neutral atom transport. Examining the reaction rate coefficients at these temperature breakpoints inform which reactions are occurring in which region. The first, T_e=80 eV is the point when $\langle \sigma v \rangle_{CX}$ is closest to $\langle \sigma v \rangle_{ionization}$ at $3x10^{-14}$ and $2x10^{-14}$ m^3s^{-1} respectively. The second, T_e=400 eV is the threshold where charge exchange reactions become 5 times more likely than an ionization event. At these high temperatures, charge exchange should dominate ionization losses for atomic deuterium. Furthermore molecular deuterium over the entire temperature range (1 eV-1 keV) is most likely to ionize by the $e^- + D_2 \rightarrow 2e^- + D_2^+$ reaction first, and then D_2^+ molecule will be broken into D and D^+ by future collisions. When the mode is not locked to the outboard limiter, the plasma is colder than 200 eV in the region swept by the neutral mean free path for neutrals sourced on the outboard limiter. While substantially colder, the reactions the neutrals will undergo do not change significantly as the neutrals interact with different phases of QSH with respect to the bulk plasma temperature. Examining the reaction rate coefficients suggest atomic deuterium in the edge is most likely to undergo charge exchange reactions. Most neutrals entering this edge will be in molecular form. The neutral molecules are most likely to first be ionized before being dissociated based on the reaction rate coefficients.

Density also controls the rate of plasma-neutral interactions, with higher density increasing the reaction rate. The effects of using probe measurements for edge density produce larger shifts in the V3Fit dataset than the probe T_e measurements. The plasma density in the

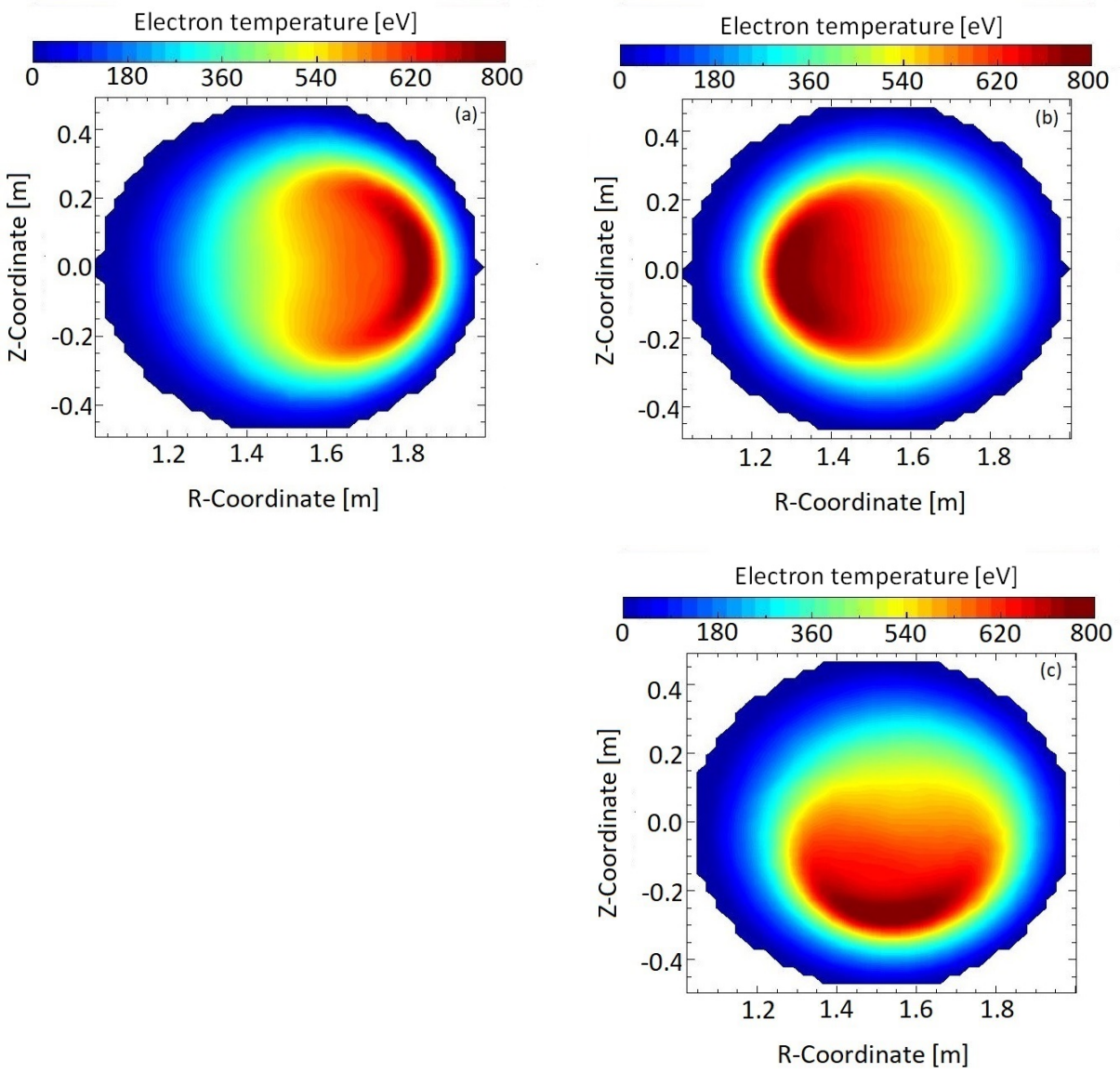

Figure 4.3: Combined electron temperature backgrounds of V3Fit and probe data for QSH plasma. Three separate toroidal slices are shown, representing (a) an outboard lock $\phi = 0$, (b) an inboard lock $\phi = 36$, and (c) a perpendicular lock $\phi = 50$. Probe data is used to form the edge plasma data.

locked, anti-locked, and perpendicular locked cases is shown in Figure 4.4. In the outboard locked case shown in Figure 4.4 (a), the density in the edge is the same magnitude as the density 10 cm inside the plasma on the inboard side, highlighting a shift of the plasma towards the outboard limiter. This proximity of higher density in the edge increases the reaction rate of plasma-neutral interactions. This causes a compression effect. Neutrals do not penetrate as far in the high-density plasma but remain very close to the source region. In Figure 4.4 (b) an inboard lock is shown . The inboard edge has a higher density than the surrounding plasma. This is a consequence of extending the probe measurements around the machine with a perfect m/n=1/5 helicity. The edge density of the perpendicular locked cross-section is shown in Figure 4.4 (c) . The edge density in both the perpendicular and anti-locked cross-sections is eight times less on the limiter than when the mode is locked outboard. The bulk plasma has essentially a uniform density inside $r/a < 0.8$, however the helical core "bean" structure has increased density. The neutrals that still remain uncharged after transport through the edge will experience little variation in the core plasma. The neutrals, sourced primarily from the outboard limiter, will interact with different plasma density depending on the phase of the mode. The neutral source is strongest when the mode is locked outboard. This leads the region of largest plasma-neutral interaction to be immediately off the outboard limiter in QSH plasmas. It will also be shown that this pressure bulge acts as shield for the helical core plasma, strongly scattering and ionizing neutrals in the plasma edge, before they reach the hot helical core plasma.

These plasma backgrounds represent the canonical 400 kA QSH discharge in reconstructions, using the average of the probe data. The mean distance to ionization varies, but if simulated using the 400 kA QSH edge parameters, values between 5.4 and 10.2 cm are obtained depending on the phase of the mode and initial direction of the neutral. These values are an order of magnitude larger than the initial first-order estimate of the ionization length scale in Section 1.1.1. Some additional effects are modeled in EIRENE and the situation is not quite the same. Earlier the estimate of an ionization length was made at 2.4 mm. One major difference is in the initial calculation the neutral was computed as an atom, while in EIRENE the neutrals are sourced as molecules released by recycling. In the dissociation of the molecule, the neutral atoms can be accelerated increasing the distance traveled before ionization. The shortest ionization lengths occur when the neutrals fly directly into the edge pressure bulge. Longest paths are obtained when neutrals are sourced on the limiter when the mode is anti-aligned and the neutral has an initial trajectory within 15° of the positive Z direction. The plasma-neutral reaction rates are strongly dependent on the phase of the QSH mode in the edge, but vary weakly in the bulk plasma. Reconstructions of 425 and 500 kA QSH plasmas were also performed. The higher current

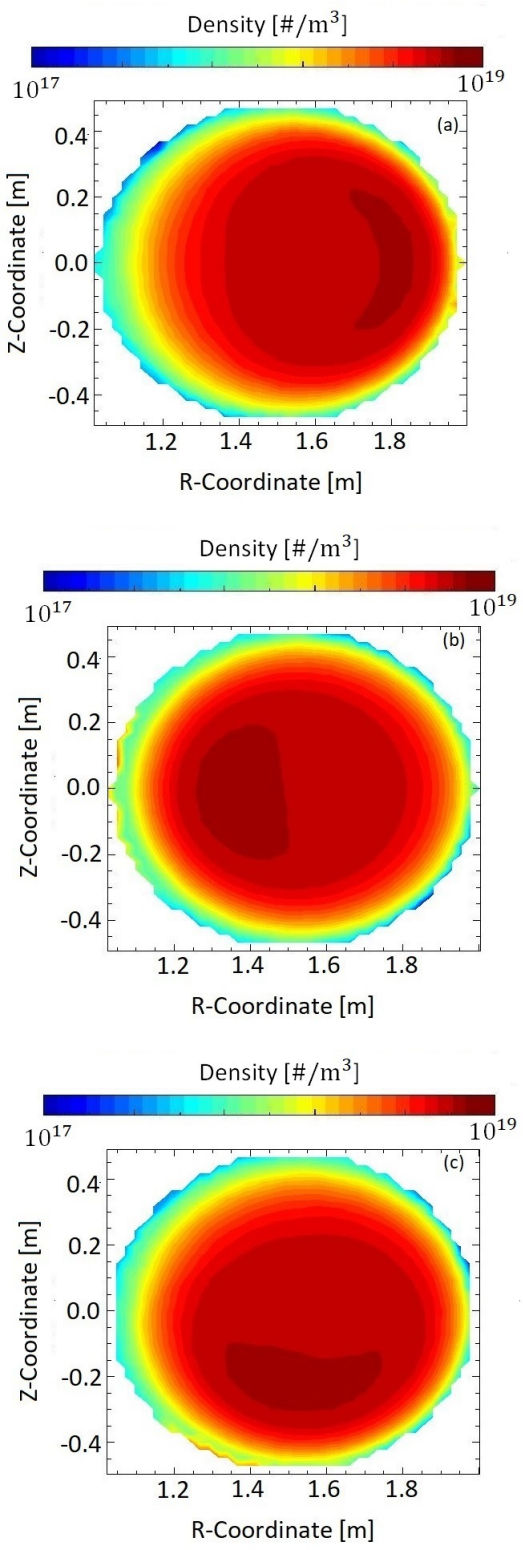

Figure 4.4: Combined plasma density backgrounds of V3Fit and probe data for QSH plasma. Three separate toroidal slices are shown, representing (a) an outboard lock $\phi = 0$, (b) an inboard lock $\phi = 36$, and (c) a perpendicular lock $\phi = 50$. Probe data is used to form the edge plasma data.

reconstructions have the same trends and general shapes as the cross-sections presented above.

4.2 Neutral sources in the model

With the plasma model established, the neutral source was left to be defined in the model before the interaction of the two could be studied. The neutral particle source distribution needed to be defined. The magnitude was established by camera measurements. Two methods are used to adjust the distribution of the neutral particles. The first is the recycling coefficient (R), which changes the magnitude of the main neutral sink in the model. The second adjustable parameter was the source ratio (SR) a term developed to redistribute some neutral particles to a uniform wall source, rather than have all sourced particles to be generated on the limiter surfaces. Scanning the recycling coefficient would alter the overall magnitude of the neutral population in the plasma, and the source ratio would alter the neutral source distribution, relaxing the assumption that all the neutrals are created by PWI with the outboard limiter made when processing camera images. These two parameters are scanned in conjunction with a synthetic camera module developed for EIRENE. The synthetic camera image can at each value of R and SR be compared to an experimental image allowing the model to be tuned to obtain maximum agreement with the experiment. The parameter scan found that the model is optimized when 5% of the neutrals are uniformly sourced and 95% are created on the limiter (SR=0.05) and the recycling coefficient for the vacuum vessel was set to R=0.93.

While examining the plasma backgrounds informs what reactions might occur and where in the plasma, the neutral source will determine where neutrals are physically sourced and the initial distribution. The neutral source was experimentally determined by camera measurements of the photon flux. Photon fluxes measured by the cameras, presented in Chapter 3, are converted from a photon flux to a neutral source by the S/XB method described in Section 2.3.4. This data determines the magnitude and distribution of the total neutral source in the model for given plasma parameters. Three material sources of neutrals are implemented in the EIRENE simulation in addition to volumetric recombination. The first is a segmented ring source that represents the outboard limiter of MST where PWI is seen. Each of the 50 segments of the ring has a point source rate based on camera observations, and the S/XB calculated using data collected by the Langmuir probes. The second source established in EIRENE is a uniform surface source to represent wall recycling. A third possible source used only in QSH discharges was the poloidal gap limiter, modeled as a surface source for a 5 cm long by 4 cm surface of the limiter tile. Neutrals in

the simulation were sourced relative to the surface normal with a cosine distribution. The cosine distribution is a good approximation for the angular distribution seen in experiments where graphite tiles release H_2 while under H^+ bombardment [83], [84] and should be appropriate for graphite tiles that release D_2 while under D^+ bombardment as is the case in MST. Lastly, recombination was allowed to occur in the bulk plasma. EIRENE would calculate the volumetric recombination based on ADAS data files. Volumetric recombination also produced photons. These photons can be tracked and tallied over surfaces, with given efficiencies, to produce synthetic diagnostic responses.

4.2.1 Modeling the recycling coefficient

Much of the vacuum vessel interior is aluminum coated with a graphite dust, and other material properties inside MST were not well known. Graphite dust has been found coating the vessel wall of MST during maintenance vents. It is believed to be deposited from many years of erosion of the graphite limiters. In order to work around this information deficiency the EIRENE model was tuned by adjusting the recycling (R) coefficient. Recycling on the vessel wall was stepped in EIRENE simulations from an R=0.75 to R=0.90, by 0.5 increments, and R=0.9 to 0.95 by 0.01 increments. The recycling parameter controls the synthetic image brightness in the simulation. As recycling is raised, a given neutral source rate creates a higher neutral density profile as fewer losses to material surfaces occur. The range of R=0.75 to R=0.95 is scanned over to reflect the range of recycling coefficients measured in the experiment (Figure 3.8). There is no data for aluminum in the material database used for surface erosion modeling in EIRENE [70]. The carbon database contains data for clean graphite. Modeling would still be required to correct for surface roughness. In addition the aluminum surfaces are coated with graphite dust in MST, this leads to a mixed material problem. Rather than model the wall in great detail, the same result can be achieved by changing the effective recycling coefficient to best match the intensity of synthetic images to the experimental image. This scan of the recycling coefficient effectively sets the loss rate of neutrals to material surfaces. Wall conditions are held at a constant surface temperature. The other possible loss mechanisms for neutrals are plasma-neutral interactions and pump-out by the vacuum system (Section 1.3). The results of this optimization process are shown in Figure 4.5.

The recycling rate was tuned using an axisymmetric MH plasma simulation at 200 kA. These plasmas were chosen as the test case for the recycling scan because the MH plasma has uniform recycling around the machine as compared to the QSH mode (Figure 3.6). This eliminated the effect of source distribution in the recycling scan. Select synthetic images from the recycling scan at values of R=0.75, 0.85, and 0.93 are presented in the

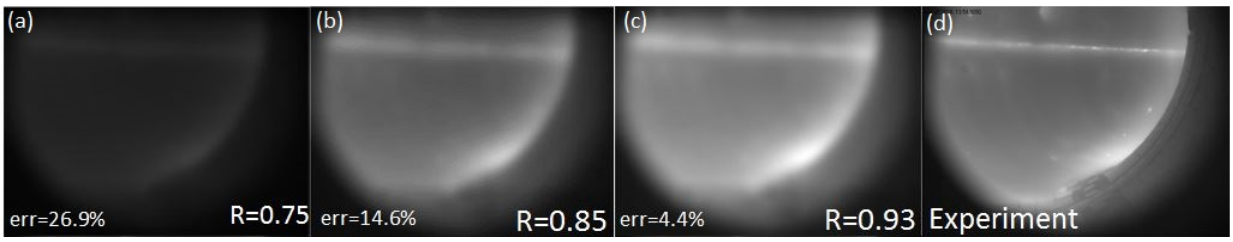

Figure 4.5: Comparison between synthetic and experimental images for an axisymmetric source standard plasma are generated by tuning the recycling coefficient to adjust overall image light levels.

Figure along with an experimental image for comparison. The value of R=0.93 optimizes the image intensity agreement with the experimental data. Error in image intensity of 4.4% is obtained. This error is calculated as the mean of the individual pixel errors or:

$$\sigma_{image} = (\frac{1}{N_i} * \sum_i \frac{I_{syn,i} - I_{exp,i}}{I_{exp,i}}) \tag{4.1}$$

where N_i is i-th non-zero pixel in the experimental image, σ is the image error, and I is the intensity of a pixel in either the synthetic or reference image. This calculation is performed by comparing all nine camera views generated from the EIRENE model for a given recycling coefficient and the equivalent images for experiment taken by the BVCs. In this computation, the error is calculated by the pixel-weighted difference in total photon intensity measured by the real and synthetic cameras. As the model was established based on on the axisymmetric plasma, 3D shaping effects are minimal. Selecting the recycling coefficient minimizes this error by tuning the model to match camera measurement of D_α photons. The experimentally measured source rates set a target and this procedure then adjusts the loss rate of neutrals through the recycling coefficient such that the model best agrees with experimental data.

In the leftmost image of Figure 4.5 (a), the error is largest, and recycling values are the lowest at R=0.75. At this low value of recycling, many neutrals are lost to the material surfaces. The D_α light is minimal. As recycling rises, neutrals cease being lost to the material surface and instead populate the plasma edge as in Figure 4.5 (b). Both the R=0.93 synthetic image, Figure 4.5 (c), and the experimental image, have a bright horizontal line over the limiter source and a less intense glow around the entire plasma edge suggesting the source distribution of the model is well matched to experiment. Both images have an increased brightness in the lower right region where light is being picked up along the curved center of MST. The synthetic image is more diffuse than the experimental image,

implying that in modeling the neutral particles are more scattered than in the experiment. Alternatively, the choice of cosine distribution for the launch angle may not be optimal. The synthetic image lacks the well defined limiter line of the real image. Another reason for the blur is that the EIRENE cell size is approximately as large as the space between line-of-sight endpoints on the wall, a finer resolution in EIRENE may reduce this blur. Despite these discrepancies, the total photon counts between the real and synthetic camera come to 4.4% agreement. Raising recycling further causes overpopulation of neutral particles and brighter images. The neutral population in the model has three depletion pathways: neutral interaction with the plasma, loss to vacuum pumping, or loss to material surfaces. As the model recycling coefficient approaches unity, neutrals lost to the material surface decrease and more plasma-neutral interaction occurs. Without as much neutral losses, the population increase causes the neutral excitation and photon emission levels to exceed experimental camera measurements..

Comparing the synthetic images from EIRENE with the experiment in this manner gives insight to the effective recycling in MST. Experimentally values of 0.65 to 1.0 are seen for QSH plasma, while calculating the MH recycling based on density decay measurements and confinement times predicted by MSTFit yields R=0.87$\pm$0.4. EIRENE is optimized with R=0.93, not far from the experimental calculations. Strong agreement between model and experiment can be obtained even with imperfect knowledge of the material conditions in a fusion device using this optimization procedure. This use of effective recycling coefficient also saves computational time as a model for surface roughness does not need to be invoked each time a neutral collides with a wall or limiter. Furthermore as the material conditions in MST change, for instance, the graphite dust is removed from the aluminum walls this effective recycling coefficient can be easily updated for future work.

The recycling coefficient establish by this modeling effort represents a moderately pumping wall situation. The recycling was shown earlier as a function of the local plasma edge conditions. The moderate pumping of the limiter surfaces have implication to longer pulse experiments performed on future RFPs in which some form of active fuel injection will be required to maintain discharges. In addition the 3-D plasma of the QSH plasma may be exploitable to create divertor-like scenarios for the RFP configuration.

4.2.2 Adjusting the source distribution to experimental conditions

Another assumption was made in analyzing the data: “All neutral particles were created by PWI on the limiter”. This assumption is relaxed by adjusting the source ratio (SR). Here the SR represents the particle sourcing between the limiter and wall components in MST,

changing SR changes how many neutrals are sourced in the uniform wall source compared to the outboard limiter source.

Scans were also performed to measure the influence of a second parameter, the source ratio (SR). A SR of 0.0 would correspond to the initial assumption of all neutrals originating on the limiter. As SR increases neutrals are increasingly sourced from a uniform wall distribution rather than the limiter distribution. There are two reasons why the SR is introduced. The first is that the assumption that all neutrals come from the limiter is extremely unrealistic. Even though a great majority will be produced by plasma impacts on the limiter, charge exchange neutrals or other particles still may recycle off the wall. The second is that MST has a number of diagnostic portholes in the vacuum vessel. The larger of these have their own limiter tiles for protection of diagnostics. One such porthole is seen in Figure 4.5, where in the experimental image at the center of the top a circular glow is seen above the limiter. This is a porthole for the FIR laser. Allowing for non-zero SR allows for these surfaces, not modeled in detail, to act as a neutral source in the model. Effectively the portholes are averaged together into the wall source.

A SR of 0.0 leads to synthetic images that are overall dark and overly bright near the source as seen in Figure 4.6. A 400 kA QSH plasma was chosen for the tuning data because these plasmas have the most peaked neutral source. The strongly localized 400 kA QSH source allows for the most contrast between the limiter source and the wall source. Choosing images where the light is strongly localized to the limiter increases the sensitivity in modeling the SR coefficient. In selecting plasmas where most of the neutrals are born at a single location, it becomes easier to differentiate the uniform wall source from the neutrals sourced on the toroidal limiter from the unlocked regions, aiding selection of SR. In order to compare the synthetic cameras accurately to the simulation, an upper limit to the photons the synthetic camera could measure was introduced to mimic the optical sensor saturation. The synthetic pixels are saturated in SR=0.0 simulations at 121% of the allowed photon collection limit. As the SR is raised, the light becomes more dispersed, the pixels that view the region of the strongest neutral source no longer saturate. The neutral source shifts from a peaked source to a joint limiter and wall source. The experimental image these data are compared to is shown in Figure 4.7, where the optimized agreement of the tuned model and the experimental data is shown.

Four synthetic images generated as part of the SR scan are presented in Figure 4.6. The total source rate in all the simulations is the same; it is only the distribution that is changing. SR=0.05 minimizes the image error. In the Figure all frames appear visually the same, but have total intensities that vary slightly. The left-most frame in the figure has a pure limiter source, and as such almost all excitation and radiation is emitted in the

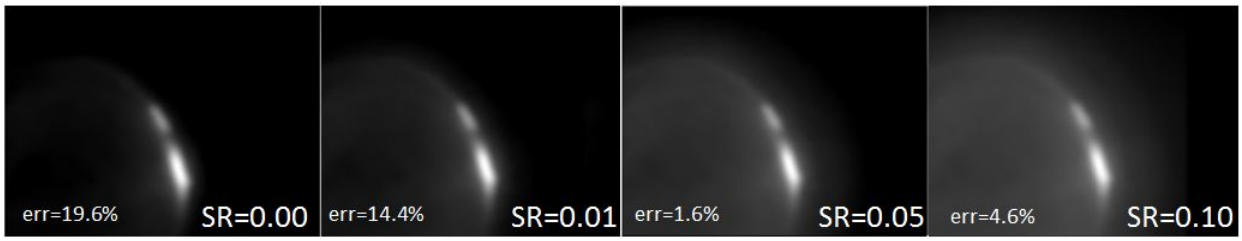

Figure 4.6: Comparison between synthetic images for an axisymmetric source standard plasma, tuning the source ratio (SR) to distribute the recycling source. An experimental image for reference may be found in Figure 4.7

edge in front of the limiter. As SR rises, light sources spread throughout the plasma, as a fraction of the neutrals is sourced from the full wall instead of the local limiter source. The simulated cameras begin to measure photons throughout the plasma volume as SR is raised. In scanning over SR in this way, the assumption that all neutrals are created by PWI with the limiter is relaxed.

Determining SR enables the model to account for more complex neutral distributions than just the outboard limiter. It also acts as a rough estimate of how much the plasma of MST is impacting surfaces other than the outboard limiter. Furthermore, this parameter can be updated or changed as needed in response to physical changes in MST. For instance, a large porthole for human entry into MST may be added in the future. Camera measurements can be redone and the new total neutral source can be calculated, adjusting SR in the procedure described here would allow for rapid updating the EIRENE model of MST to changes in the vacuum vessel.

With the EIRENE model tuned to SR=0.05 and R=0.93, the experimental library was searched for an image which maximized agreement to the synthetic image. The selected experimental image was taken when viewing a high quality (Q=9.2) QSH discharge (# 1180401096:36ms) and is shown in Figure 4.7. In this discharge, the QSH mode is locked outboard at the poloidal gap, and the plasma is a 421 kA, $0.6\text{x}10^{13}\text{cm}^{-3}$ discharge. The EIRENE simulation was run using the 400 kA QSH source distribution as described in Chapter 3. The minimum error between the synthetic image and library images is 1.6% when using Equation 4.1. Image error is calculated as the sum of pixel error divided by the number of pixels in the calculation. Only pixels that view the wall and limiter structures opposite the camera are used in the comparative analysis. Pixels in the source image that are at or below the noise level (2/255 bits) are not used in the calculation. This keeps the empty space which occupies the right $\frac{1}{3}$ of the imagine from influencing image agreement. Average error, sampled over all experimental and corresponding synthetic images, was found to be 16.4% for 400-430 kA QSH data. This error represents the average accuracy of

EIRENE to reproduce experiment-like images. The initial assumption that all neutrals are sourced from the limiter was restrictive but allowed for assessment of the total recycling values before the modeling work had begun. Rather than an optical and material analysis of the interior of MST, relaxing the SR and R parameters enabled the production of synthetic images with good agreement in both light distribution and image intensity to experimental observations. The capability to reproduce experiment-like images in EIRENE enables the modeling effort to move forward. The plasma-neutral losses over the full volume of MST cannot be measured. Having a model that produced on average 16.4% error in synthetic images is evidence that EIRENE is accurately modeling the plasma volume. If these images are in good agreement, the power loss predictions of the code should also reflect the reality of the experiment.

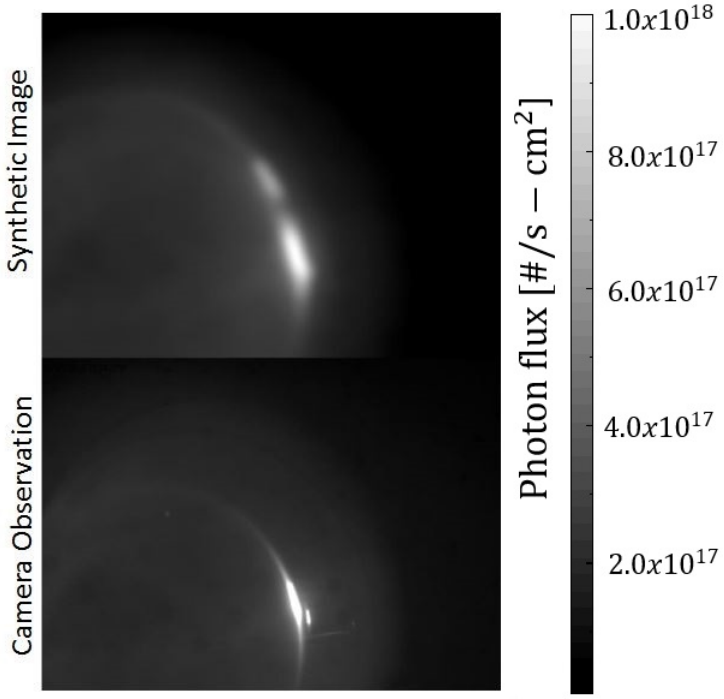

Figure 4.7: A synthetic image produced by the tuned EIRENE model and a real image from the image library. This is the best-case scenario which approximates the location and relative brightness between images. Other images chosen at random have worse agreement to the synthetic image.

4.3 Validation of the synthetic model

One additional test of validation for the EIRENE model was performed by comparing line integrated D_α signals in the model to the D_α array on MST. A synthetic line integrated D_α detector array is constructed in EIRENE. This synthetic diagnostic array can be compared to experimental measurements. Similar to the line of argument used above, if the synthetic and experimental D_α detectors agree well, confidence in the EIRENE model is increased. Furthermore as the D_α array is not used to determine the neutral source this test is completely independent, that is, tuning EIRENE to match camera images may have just produced a model that can match its input well, while the signal of the synthetic detector has no reason to correlate to the real D_α array unless the camera based EIRENE model accurately represents MST. In the Figures 4.8,4.9,4.10, the simulated D_α signal through 8 lines-of-sight is compared to the experimental averages of the D_α array over the same lines-of-sight. EIRENE is used to simulate three different plasma conditions, 400 kA QSH, 400 kA MH, and 200 kA MH. These cover both high and low I_p as well as both magnetic configurations.

The 400 kA QSH results are shown in Figure 4.8. The experimental data was recorded when the QSH mode was locked outboard by the MST active feedback system at the D_α array. This position is chosen to produce the largest neutral source in view of the detectors. The photon flux seen in EIRENE matches the general shape of the photon flux seen by the detectors. Largest values are outboard $(r/a{=}+1)$, with the minimum being located between r/a=-0.5 and 0. The most important region of agreement is the plasma edge, where neutral population is the largest.

Here EIRENE predicts eight times higher than the experimental measurement. The neutral density is indirectly represented by the line integrated value of D_α light. EIRENE simulations produce results that are consistently a factor of 2-8 higher than seen in the experiment. The EIRENE error bar in the edge is extremely low. The error in the EIRENE simulations is the statistical simulation error from the Monte-Carlo processes. It is low as 10,000,000 neutrals are used in the simulation. These data do not include the error in the camera photon flux measurements used to determine the source rate. Experimental error D_α is the standard error for the data set. The higher EIRENE prediction of D_α light in the MST edge implies the model may be over predicting neutral density by up to an order of magnitude. One other possibility is that the experimental detectors have a transmission loss not accounted for in the simulation. The D_α detectors were calibrated approximately a year and a half before this experiment was conducted. A decrease in transmission due to material deposition on the optics can reduce the experimental D_α signal. Another possible

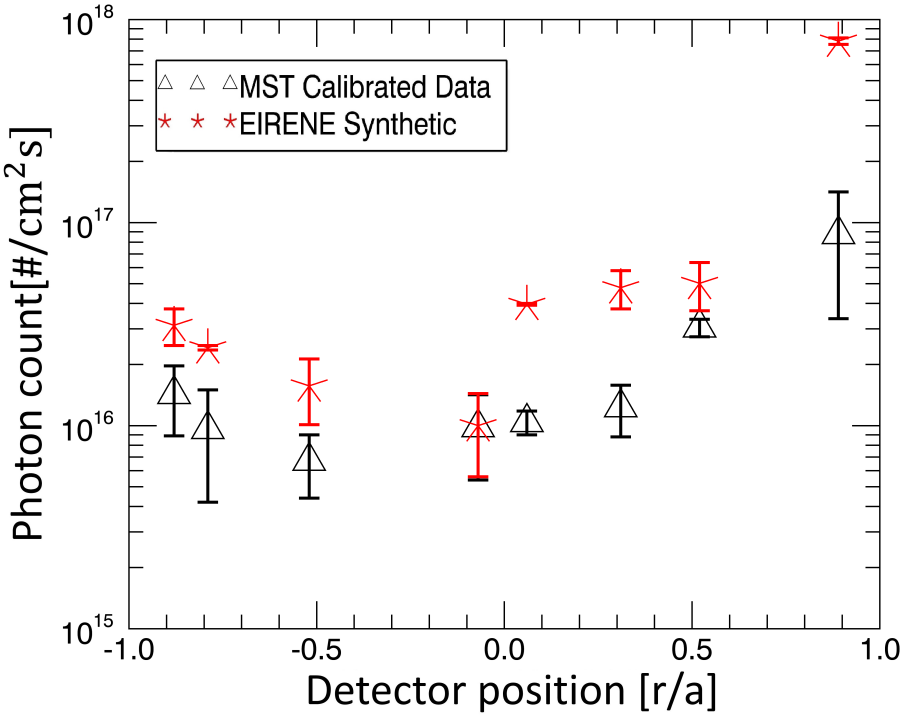

Figure 4.8: The comparison of D_α signals obtained from an average of experimental data to those from a tuned EIRENE model synthetic diagnostic. Agreement between 400 kA QSH plasma experiments and simulations is fair. Some simulated data overlaps experimental data, while at the edge simulation is predicting a few times higher than experiment.

explanation could be the model is over tuned.

MH plasma simulations were also conducted. D_α comparisons for a 400 kA plasma are shown in Figure 4.9. Again, the shape and minimum photon fluxes correspond well. In the standard plasma, the minimum D_α flux is in the central plasma as seen on the detector nearest r/a=0. In this case, the outboard data overlays well except for the outermost detector. Here EIRENE is a factor of eight higher. On the inboard side, EIRENE is consistently a factor of three higher than the experimental data. Both high current simulations are over predicting in the edge.

The last case examined is that of low current 200 kA MH. The results of the simulation overlaid with experimental data for 200 kA MH are shown in Figure 4.10. This simulation produces synthetic D_α signals with the strongest agreement between experiment and model. Agreement is better in the center of the plasma than the edge, with the observed photon fluxes being within the error bars of simulation and measurement, while the

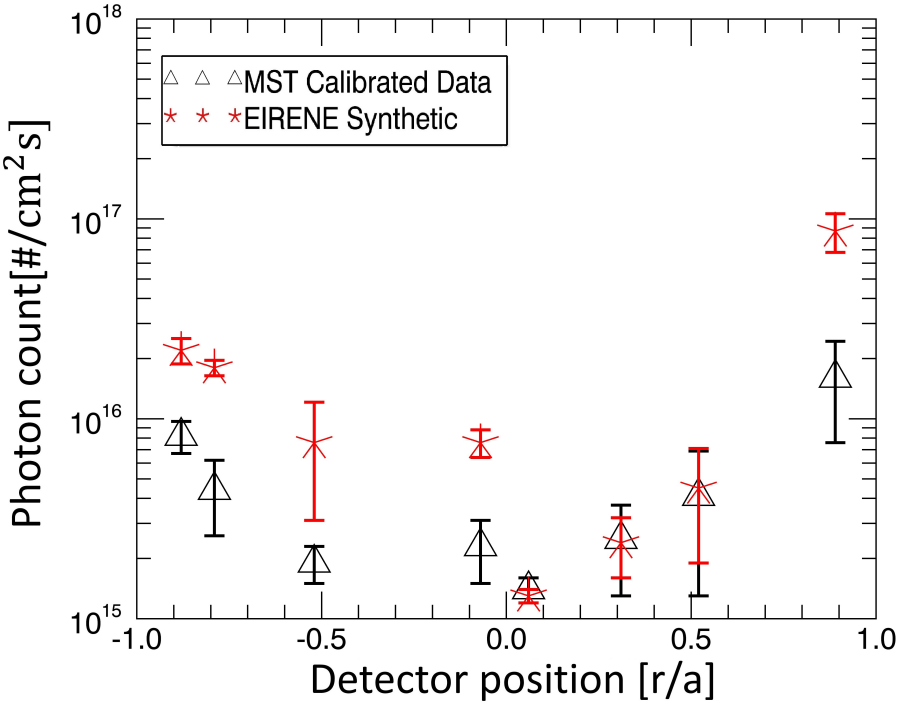

Figure 4.9: The comparison of D_α signals obtained from an average of experimental data to those from a tuned EIRENE model synthetic diagnostic for 400 kA MH plasma.

EIRENE edge values are factors of 2-3 higher than the experiment. Despite having a stronger neutral source than 400 kA MH plasmas, these plasmas produce lower D_α signal both in simulation and experiment. Low current plasmas do not produce as strong D_α signal as less recombination is occurring in the edge, this is seen by comparing the detectors at r/a=0.5 and r/a=-0.8. In the 200 kA case these signals are higher in both simulation and experiment. The D_α signal is slightly shifted from the outermost chords to mid-radius chords. This implies neutral particles penetrate deeper into lower current plasma.

This set of data justifies use of the EIRENE model for reconstruction of the neutral population in MST. The agreement between experiment and model is within a factor of 3 for 200 kA MH plasma and within an order of magnitude for 400 kA MH and QSH states. The model of MST, as implemented in the EIRENE framework, provides reasonable order of magnitude results in reconstructions of MH and QSH plasma. In addition, the consistency of the EIRENE implementation framework to predict higher data than the D_α array suggests that the D_α array optics may have reduced transmission from buildup on the lenses. The EIRENE implementation framework is capturing the transport physics of

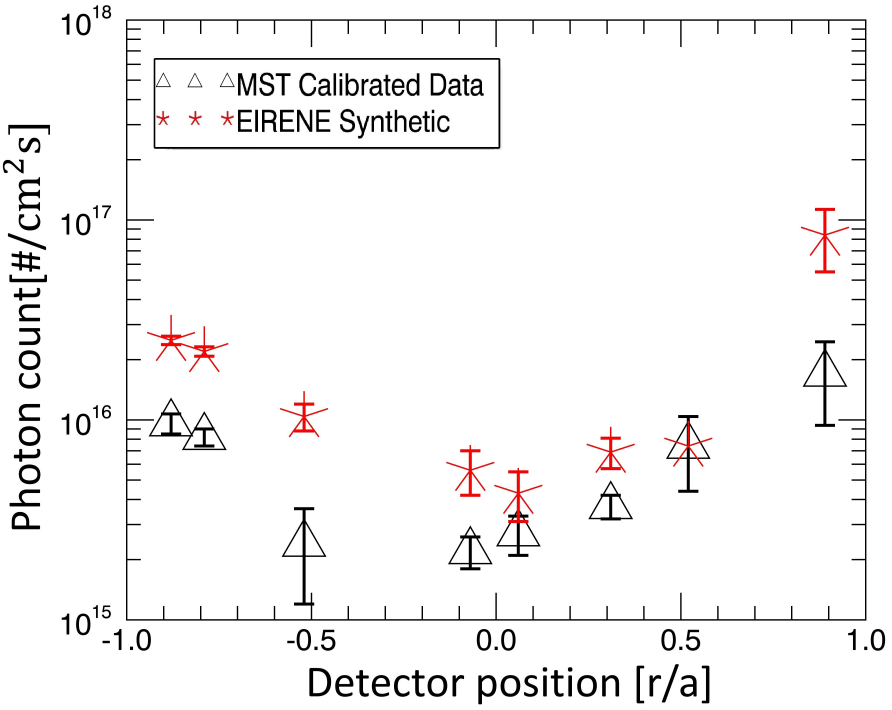

Figure 4.10: The comparison of D_α signals obtained from an average of experimental data to those from a tuned EIRENE model synthetic diagnostic for 200 kA MH plasma.

neutrals in MST well as shown by the agreement of the shape of the D_α profiles across the eight chords. Maxima and minima are found at the same locations in each of the 3 scenarios. If the transmission of detectors in the EIRENE simulation were decreased 56%, much stronger agreement could be obtained. Averaged between all detectors, the ratio of photon flux $\frac{\text{EIRENE}}{\text{Experiment}}$ would decrease from 1.86 at full transmission to 1.14 at 56%. Further reductions in transmission coefficient cause a mismatch as the simulation will begin to under-predict.

4.3.1 Temperature sensitivity of the edge

In order to assess the sensitivity of the measurements to change in edge parameters a scan of edge temperature was performed. In this scan the response of three simulated D_α detectors is compared as the edge temperature is changed a factor of 2 up (+100%) or down (-50%). The simulations are conducted for the case where the QSH bulge is locked outboard when toroidally aligned to the simulated detectors. T_0 is the nominal temperature of the QSH bulge at 50 eV on the last closed flux surface. Plasma temperature is adjusted

outside r/a=0.94. r/a of 0.94 is chosen as the boundary point as this is the furthest out V3Fit reconstructed data. The data at the outermost cells of the simulation from probe measurements on the LCFS was adjusted between 25 eV and 100 eV. A linear fit between r/a=0.94 and the outermost cell was used to populate the cells in the edge region. EIRENE simulations using this framework were conducted and the results are shown in Figure 4.11. The three detectors chosen are an edge detector at r/a=0.9, a mid-radius detector, at r/a=0.5 and a core detector at r/a=-0.1 The core detector has been adjusted by a factor of 100 to show the simulated photon fluxes in the same range. When examining the core detector changes in edge temperature alter the core measurements strongly if the edge is cooled, but only slightly if the edge is increased. The mid-radius measures approximately the same level of D_α emission, at the nominal and higher edge temperature values. This suggests the neutral population that enters the plasma is insensitive to the edge conditions. A small amount of neutrals penetrate the core and scale with the edge temperature. The detector with the line of sight at r/a=0.9 is strongly influenced by the edge temperature. Reducing the temperature by a factor of 2 causes a 2.8 increase in the photon flux observed. This is a consequence of the changing cross-sections in the edge and outer plasma region, with colder plasma raising the rate of excitation and lowering ionization. Doubling the edge temperature reduces the edge detector by a factor of 3. At lower than the nominal 50 eV T_e in the QSH pressure bulge these results suggest an increasing hollow neutral density profile may be possible. With higher temperature in the pressure bulge a slightly flatter profile occurs. These relative sensitivities to the edge temperature can be considered additional sources of error the EIRENE implementation framework does not capture. The framework assumes the mean of the probe and camera measurements is representative of the edge and the error in the probe measurements was not propagated to the model.

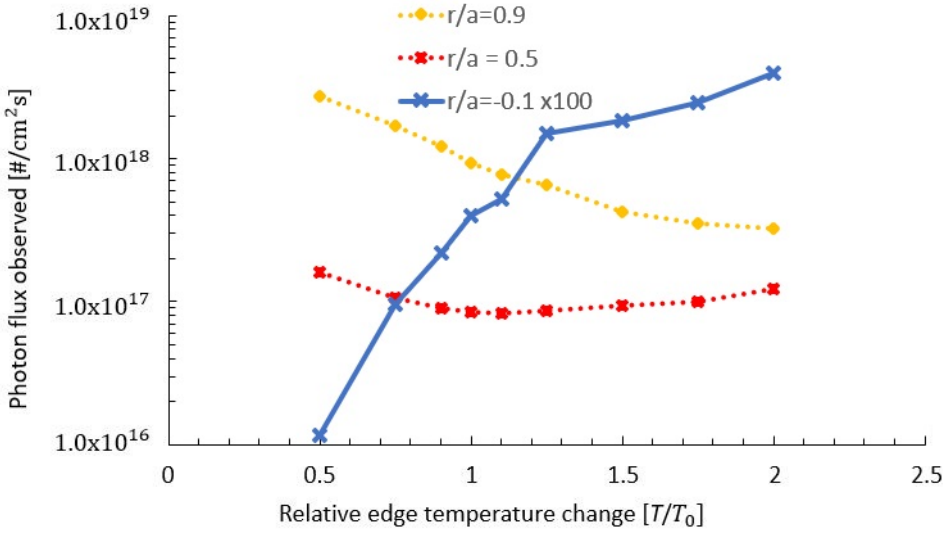

Figure 4.11: A scan of the sensitivity of the D_α detector measurements compared to changes in the modeled plasma temperature. Core measurements are scaled by 100 to be placed on the same plot.

4.4 Fully 3D neutral profile computations

With output of the EIRENE model matching experimental observations reasonably well the resulting neutral density predictions of EIRENE are examined. For the first time, 3D neutral density profiles for MST plasma under various conditions are produced. For the plasmas discussed in this section MH plasmas are 200 or 400 kA with n_e of $1x10^{19}$ m^{-3} and QSH plasmas are 400 or 500 kA with n_e of $0.5x10^{19}$ m^{-3}. The differences between neutral density profiles between these plasmas will be discussed in the following Sections. Generating these 3D neutral profiles will aid understanding of the neutral population in MST plasma and enable calculations of the plasma-neutral interactions.

During QSH, the source of neutrals is very localized as shown in Chapter 3. The corresponding neutral density profile is represented by a pair of cross-sections shown in Figure 4.12. Neutral density is shown at toroidal angles of ϕ=0 and ϕ=36 degrees. The neutral density is plotted on a log-scale. The neutral density is largest in the outboard edge varying one order of magnitude from 10^{11} to 10^{12} cm^{-3}, with the exception of the few cells just in front of the limiter where the value approaches the edge plasma density magnitude of $4x10^{12}cm^{-3}$. Neutral density drops off nearly 4 orders of magnitude from the edge into the core region. The core plasma is essentially fully ionized. A poloidal cross-section from the same EIRENE simulation where the QSH mode is inboard is presented in Figure 4.12(a). This cross-section is located 36 toroidal degrees (half a QSH period) away from

the data presented in Figure 4.12(b).

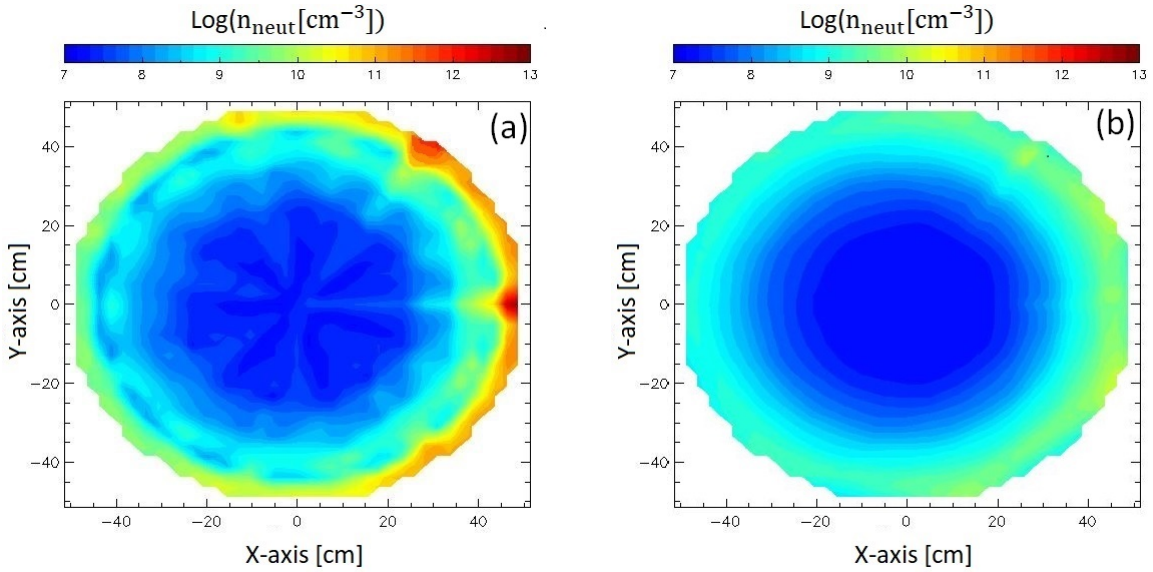

Figure 4.12: Neutral density is shown in poloidal cross-sections of QSH plasmas. Outboard is on the right in both plots. Figure(a) is of an outboard locked QSH mode. Figure(b) is the density cross-section for an inboard locked QSH mode. This cross section was generated by averaging three toroidal slices centered on $\phi = 0$ and $\phi = 36$.

Both QSH cross-sections are the average of three toroidal slices of data centered on either toroidal angle of ϕ=0 or ϕ=36 degrees. Averaging is such that these Figures are representative of a region of plasma where the QSH pressure bulge is locked to the wall (a). and of a region where QSH pressure bulge is far from the wall (b). Both Figures have increased neutral populations on the outboard region of the confinement volume. The neutral population is two orders of magnitude more dense in the case of the QSH mode-locked in front of the limiter with a peak edge value of 7.2x10^{12} cm^{-3} compared to the edge 36 toroidal degrees away where the peak edge neutral density is 5.2x10^{10} cm^{-3}. Neutral density in the center of the plasma is the same regardless of the phase of the QSH mode at around a few 10^7 to 10^8 cm^{-3}. The neutrals tend to spread more poloidally around the machine from their outboard limiter source than penetrate deeper into the plasma. This can be seen in both Figures by the broad region of relatively high neutral density that exists at r > 42 cm and over the poloidal region from approximately 60 degrees above or below the outboard limiter.

The distribution of the neutral population throughout the edge of the plasma is significant for two reasons. The first is that the plasma edge is populated with neutrals even though 95% of the source is located on the outboard limiter. Moreover the 30% of the

limiter that contacts the edge pressure bulge is the dominant source region. Despite this extreme localization of the source, the full plasma edge populates with neutrals. Neutrals are ionized efficiently in the MST core plasma.

This the low neutral density concentration in the core plasma region is unexpected. Franck-Condon pair production and charge exchange acceleration might be expected to transport neutrals into the center of MST. On investigation of charge exchange events it is found that 74% of these events lead to the neutral particle being lost to material surfaces rather than the fast neutral undergoing another collision event in the plasma. This contributes to the hollow core of the QSH neutral profiles. The neutrals that do exist inside the helical core structure of QSH plasma are "hot" neutrals. Average neutral temperature from r/a<0.5 is 230 eV. The neutral temperature in the edge (r/a>0.95) is less than 1 eV.

QSH toroidal cross-sections are shown in Figure 4.13 for 500 ka (a) and 400 kA (b) plasmas. In these Figures, the effect a 5-period localized neutral source has on the neutral density is highly evident from the peaked lobes on the edge of the plasma. The QSH neutral profiles modeled in Figure 4.13 have a neutral density with a 5-fold symmetry which reflects the source distribution. The data has been adjusted so that the first source peak occurs at $\phi = 0$. The QSH pressure bulge is outboard (positive) at $\phi = 0$ and inboard at $\phi = 36$. The five blue regions are the helical core. Neutral density is at a minimum in the helical core. These regions are both far from the primary neutral source, as well as hot with T_e ranging from 600-800 eV (Figure 4.3). The region of the helical core closest to the source still has a sizable neutral population of $3.3\text{x}10^{9}\text{cm}^{-3}$. The primary neutral sources on the limiter have a physical extent of about 10-30 degrees toroidally based on camera observations. This is three cells in the simulation in the toroidal direction. The source is extremely localized poloidally. The helical core of the plasma, however, is large relative to this. It has a poloidal width of 60 degrees based on V3Fit reconstructions and the pressure bulge. The average plasma temperature can be up to 75-80% of the temperature of the helical core structure, while the source rate off-hot spot may only be 4-6% of the peak source rate. As a result depletion of the neutral population by plasma-neutral interactions does not vary so much with the phase of the mode. The neutral source distribution is the strongest factor in determining what the neutral distribution looks like. The trajectory of a neutral particle entering the core plasma, that is where r/a <0.9, does not significantly effect the processes it will undergo. Neutrals that remain in the edge, r/a > 0.9, will transport around the plasma as seen in Figure 4.12.

At 500 kA (a), the neutral source becomes slightly less localized, but the average source strength increases by 20%. Neutral density in the edge peaks at $8.3\text{x}10^{12}\text{cm}^{-3}$ instead of $3.4\text{x}10^{12}\text{cm}^{-3}$ as at 400-kA (b). The edge lobes are less prominent at 400-kA (b). The edge

density is more uniform at 500 kA (b). The ratio of the peak density to the average neutral density at 10 cm is 7.1 at 400-kA (b), while it is 13.2 at 500-kA (a). This compares well to the ratios, of source peak source rate to average source rate, of 15.2 and 22.3 observed by the boundary viewing camera discussed in Section 3.2.

The neutral density for QSH plasmas, while not helical, has a definitive 3D shape. Each PWI hot spot generates a ring of neutrals which wrap poloidally around the plasma at each of the 5 toroidal locations. It may be that this setup has favorable implications on fueling. The phase dependence of ionization and confinement time of newly ionized particles was shown previously in Figures 3.9 and 3.10. Neutrals entering the region of the pressure bulge are very likely to be ionized and then shortly expelled back to the limiter to recycle. Neutrals that scatter and transport through the plasma edge then can enter the plasma at a location where the neutral fuel will be retained longer.

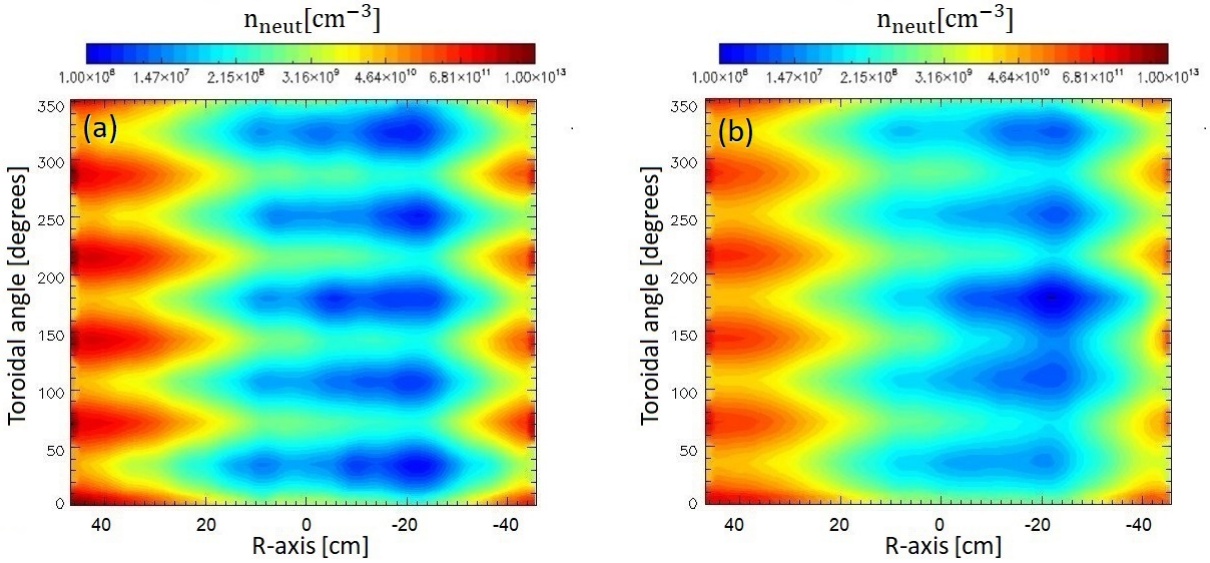

Figure 4.13: A toroidal cut in the neutral density profile for a 500 kA QSH RFP plasma is shown on the left. A toroidal cut in a 400 kA QSH RFP plasma showing poloidally averaged neutral density is shown on the right. The neutrals propagate out from the source region and are exposed and ionized. Dropoff is initially linear, where neutral molecules are being broken up in the edge, then exponential as atoms are being ionized. A 5-fold symmetry is seen in both cases.

When considering MH plasma, the neutral profiles still exhibit an outboard localization; however, they are nearly toroidally symmetric. The evolution from low current to high current plasma is shown in Figure 4.14. This Figure contains four current levels of MH plasma. The poloidal cross-sections have been averaged over the full extent of the simulation. The lowest current 200 kA case is shown in Figure 4.14 (a). This case has a

neutral source strength of $3.2x10^{20}\frac{\#}{s}$, the highest of the MH plasma. These plasmas also are the coldest, with a peak electron temperature of 270 eV and an edge temperature of 20 eV. The combination of a high neutral source rate and low plasma temperature allows for these plasmas to support a large neutral population which penetrates deeper into the plasma than any other case studied. The neutral density of up to $10^{11}cm^{-3}$ exists up to 5.7 cm from the limiter edge. $10^{11}cm^{-3}$ is chosen as a figure of merit for where a significant neutral population exists as this is 1% of the central plasma density and approximately 10% of the edge density of an MH plasma. The poloidal spread where neutrals are above $10^{11}cm^{-3}$ exists for 79.2 degrees around the exterior of the machine. A significant neutral population exists in approximately 9.1% of the confinement volume. The poloidal transport of neutrals from the limiter source is larger than the radial transport by 12 when examining the density decay lengths λ_D:

$$\lambda_D = \frac{dN/dx}{N} \tag{4.2}$$

where N is the neutral density and d/dx is a directional derivative taken either radially or poloidally. This is evaluated from the limiter cell to the point where the density has decayed an order of magnitude. The calculation is performed by starting in the cell just inside the plasma next to a limiter source. The distance in either a purely radial or purely poloidal direction is moved observing the neutral density. Once the neutral density has decreased by an order of magnitude the distance from the source is calculated. For radial distance the measurement is a straight line to the source from an interpolated (to find exactly where in the cell the density would be equal to 1/10 the neutral density in front of the source) point in the end cell. For the poloidal measurement the distance is calculated as an arc of radius 50.73 cm and angle is the poloidal distance needed to travel to reach 1/10 of the density at the source.

The radial decay for an order of magnitude is 5.6cm in 500 kA QSH plasma. The neutral density in the plasma has an up-down asymmetry due to the pump duct. When calculating the poloidal decay length, two options exist, to trace a path upwards or downwards from the outboard limiter. Choosing an initially upwards direction to the poloidal path leads to an arc of length 154 cm around the outer edge of the simulation before the density decays an order of magnitude. The alternative downward path would have a shorter decay length of 129 cm. Neutral particles with perpendicular trajectories to the wall have shorter lifetimes in the simulation. Particles that transport around the edge can move on nearly parallel trajectories to the wall and transport about the edge of the machine. The outboard to inboard ratio is not nearly as severe as in the QSH locked cases.

As the plasma current increases, there is an increase in ionization from increased

temperature. Density was held constant over all plasma currents. This was experimentally necessary as changing the density would also directly change the amount of PWI and recycling which would occur. The resulting neutral density is shown in Figure 4.14. The lowest plasma current case for 200 kA is shown in Figure 4.14 (a). Plasma current is increased to 300 kA and the results are shown in Figure 4.14 (b). At 300 kA (b) the neutral source has decreased to $2.8\text{x}10^{20}\frac{\#}{s}$ while the central T_e has risen to 310 eV. The neutral density is reduced to the value of $10^{11}cm^{-3}$ at 3.2 cm from the limiter in the radial direction and 72 degrees away from the limiter in the poloidal direction, representing a contraction to 4.7% of the confinement volume. The neutral population decreases as I_p is further raised. The edge temperature rises to 30 eV and the core plasma temperature becomes peaked at 355 and 400 eV respectively and the resulting neutral density is shown in Figures 4.14 (c) and (d).

Neutral density in these cases does not exceed $10^{11}cm^{-3}$ except the edge cells above and below the limiter. The neutral sources in these cases have dropped to $8.6\text{x}10^{19}\frac{\#}{s}$ and $7.6\text{x}10^{19}\frac{\#}{s}$ respectively. The hotter edge and lower neutral source rate prevent neutrals from building up beyond 10% of the edge density at higher current. The average value of the neutral density in MST drops from $\bar{n}_{200} = 4.8\text{x}10^{12}cm^{-3}$ to $\bar{n}_{500} = 8.6\text{x}10^{11}cm^{-3}$ as the current is raised from 200 kA to 500 kA. Neutral density in the central plasma region are similar in all cases, $10^{7}cm^{-3}$ - $10^{8}cm^{-3}$ and are 3-4 orders of magnitude lower than the edge.

A pair of toroidal cross-section of MH plasmas neutral density profiles at the midplane of the machine are shown in Figure 4.15 which highlight the degree of symmetry and the overall toroidal distribution of the neutral source when examining the averages of MH plasma. Inboard is a positive R-coordinate in the Figure. A 400 kA MH plasma is shown in Figure 4.15 (a). The outermost radial cells in front of the limiter source are uniform over the first 8 cm before a small deviation in the neutral density is observed. This oscillation around R=40 to R=35 cm is primarily the result of non-uniform wall sourcing, this non-uniform sourcing is larger at lower current plasmas, as discussed in Section 3.3.1. These variations extend the event to the core plasma; however, this variation is small and does not exist in cross-sections other than the mid-plane. If the plasma current and corresponding source are reduced to the 200 kA case, the resulting profile is shown in Figure 4.15 (b). Once again, the effect of a higher neutral source rate is observed with the edge, and average neutral density is higher than the higher current case. Some neutral penetration into the core plasma region exists in this cross-section particularity directly in front of the poloidal gap, ($\phi = 0$).

As the plasma current is increased the neutral population diminishes. This is a combi-

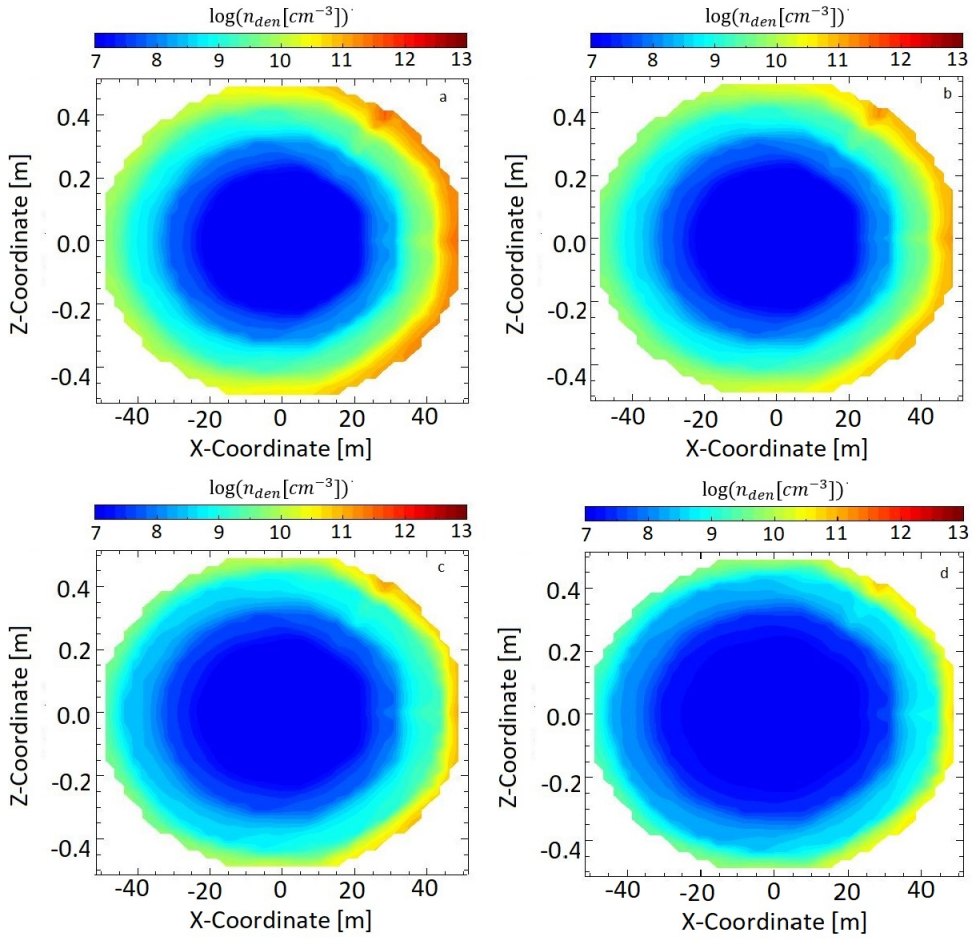

Figure 4.14: Neutral density in standard MH plasmas is plotted with increasing current from 200 kA (a), 300 kA (b), 400 kA (c) to 500 kA (d). Total neutral density and source rate is decreasing with increasing plasma current. These profiles are full toroidal averages around the machine.

nation of a decreasing neutral source as I_p increases as well as an overall warmer plasma which leads to increased reaction rates, notably faster ionization of molecular deuterium. Higher temperature plasmas ionize neutrals sooner limiting the extent they penetrate the plasma. Overall the degree of symmetry in the neutral profile is still high. Poloidal variation due to the outboard source is smaller than in QSH plasmas. In MH plasma the inboard and outboard differ by ~10. These data will be useful to future MST researchers who wish to more accurately model other diagnostics that depend on the neutral profiles.

When comparing the two cases of MH and QSH, there is a substantial difference to the shape of neutral density profiles in MST. Source localization from plasma-wall interaction causes this difference. Peak neutral density is higher in the QSH case by a factor of 3-5, while the average density is higher in the standard case, $\bar{n}_{QSH} = 7.3\text{x}10^{11}\text{cm}^{-3}$ compared

to $\bar{n}_{MH} = 2.8x10^{12}cm^{-3}$. The average density is driven strongly by the edge values as the density rapidly drops off further from the limiter source. The QSH average is further reduced by the small volume the localized neutral source creates relative to the full toroidal extent MH neutral profiles occupy.

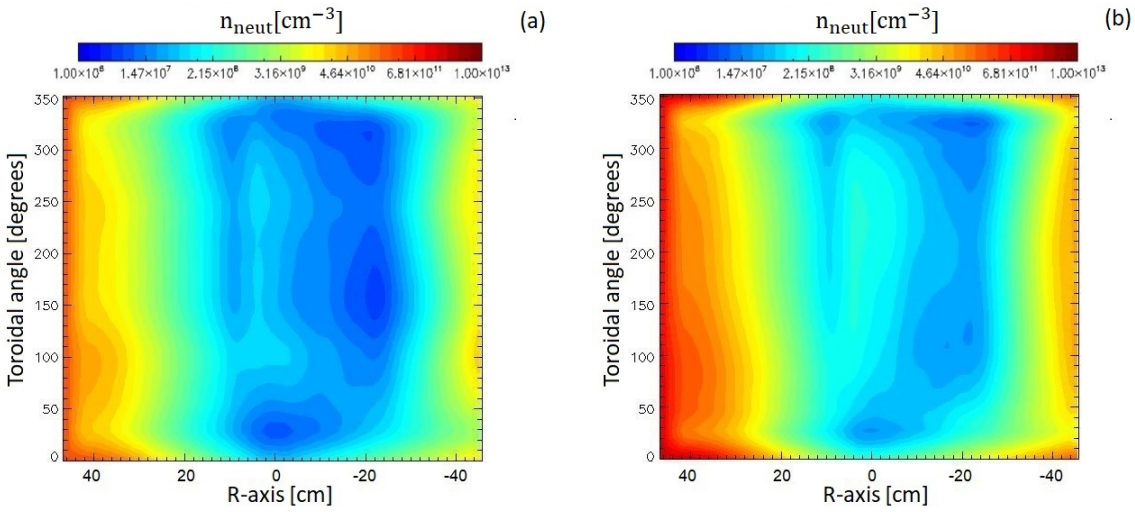

Figure 4.15: A toroidal cut in the neutral density profile for a 200 kA standard RFP plasma is plotted is plotted on the right. A toroidal cut in the neutral density profile for a 400 kA standard RFP plasma is plotted on the left. The break in asymmetry is due to enhanced recycling sources on the poloidal gap, ϕ=0. No helical or other periodic structure is observed in the MH reconstructions.

The plasma current appears to have a similar effect on the neutral density of the plasma depending on the configuration, QSH or MH. 200 kA standard plasmas exhibit significantly higher recycling than the 400 kA MH plasmas. Section 3.3 detailed this in terms of the camera observations of the edge. When modeling the neutral fluxes of the 200 as compared to 400 kA MH plasmas, the neutral density in the 200 kA case average rises to $\bar{n}_{MH} = 4.4x10^{12}cm^{-3}$, a 57 % rise over the 400-kA case. This trend is similar to the QSH cases, although the localization in QSH is stronger than in MH cases. An increase in QSH current to 500 kA from 400 kA causes $\bar{n}_{QSH}$ to fall to $5.7x10^{11}cm^{-3}$, a 22% decrease in the average neutral density nearly matching the 20% decrease in the source rate.

3D neutral profiles in MST have been produced for MH and QSH plasmas over a range of currents. In MH plasmas, the neutral population is toroidally symmetric. The bulk of the neutral population in MH plasmas is a cylinder thickest near the outboard limiter. At higher plasma currents this cylinder shrinks in thickness, owing to a reduced neutral source and hotter plasma. The QSH neutral population exhibits a 5-fold symmetry with a neutral ring that surrounds the plasma at each toroidal location of a PWI hot spot. It is the

neutral source which determines the shape of the QSH neutral population, as the neutrals are not magnetized. Plasma bulk plasma conditions do not vary significantly enough to create angular dependence of the neutral profile in QSH plasma.

4.5 Plasma-neutral losses

Now that fully 3D neutral profiles and plasma backgrounds were produced, the interaction of the neutrals at the edge was investigated with EIRENE. The primary goal of this work was to determine the extent that plasma-neutral interactions can act as an energy sink. The variation of plasma-neutral losses in QSH plasmas are evaluated with respect to the plasma edge density to determine the sensitivity to edge conditions. This section will discuss the method of assessing the plasma-neutral losses, compare the metrics used, and discuss the localization of these losses. This section will conclude with a summary on the fractional power losses for each of the plasma scenarios studied.

EIRENE is used to compute the plasma-neutral interactions. Tallies of the total energy exchanged between the plasma and the neutrals are kept as the simulation runs. EIRENE uses tabulated data from atomic databases to calculate an electron energy loss rate or ion energy loss rate in $\frac{W}{cm^3}$ where the loss rate is a function of local cell plasma parameters. The exact form of the terms being calculated is:

$$\langle \sigma v_e E_{loss} \rangle = \overline{E_{loss}} \langle \sigma v_e \rangle \tag{4.3}$$

where $\langle \sigma v_e \rangle$ is a reaction rate discussed in Chapter 1, E_{loss} is the energy losses per collision and the bar above E_{loss} represents an average energy lost per collision, a function of T_e and reaction. When dissociating molecules, the velocity distribution of the products is isotropic in the center of mass system and the dissociation energy shared between the products. When ionizing molecules and atoms, energy is removed from the plasma background in the simulation based on the appropriate electron impact event. Two main metrics are used to measure the plasma-neutral losses in this study. P_{ei}, the power loss from electron impact events, is the sum of all energy lost by electrons to any plasma-neutral interaction. The process of radiative and three-body recombination are both included in the P_{ei} tally. That is in radiative recombination, the photons produced count against the bulk electron energy balance. In three body recombination, the energy released from recombination can be given back to the plasma by adding to the 3rd body, the bulk plasma electron. The second metric is P_{cx} the power losses from charge exchange. While elastic collisions between neutrals and molecules are allowed to happen, the majority of the energy

exchanged between the bulk plasma ions and the test neutral particles will be in the form of charge exchange. The energy loss of the plasma ions is calculated as net kinetic energy exchanged during charge exchange reactions. The two terms constructed, P_{ei} and P_{cx}, represent the sum of the energy lost through the plasma-neutral interactions. EIRENE normalizes this value per particle of neutral source so in each case the total neutral source strength must be known to extract an absolute value.

4.5.1 QSH plasma-neutral losses

The sum of neutral-plasma power losses are investigated in 400 kA QSH plasmas. The absolute magnitude of the neutral source is known from the BVC measurements. An experiment is performed to examine how the neutral losses scale with plasma edge density. This experiment is designed to use the plasma edge density measured by the probes for three cases. Case (a) utilizes the lowest density measured by the probes in 400 kA QSH, case (b) uses the average density, that is is the nominal 400 kA QSH profile used in the rest of the work, and lastly case (c) uses the highest densities measured by the edge probes. Poloidal cross-sections of P_{ei} for these cases are shown in Figure 4.16. The ratio of the change in density between the Figures is approximately $0.2 : 1 : 2$. Each plot corresponds to one of the described density cases. The power losses are plotted on a log scale. In the low density case the plasma is losing energy to neutrals over most of the outboard 1/3 of the confinement volume. The losses are largest closest to the outboard limiter. A region of electron energy loss is seen on the inboard limiter as well. As the edge density increases to (b) the electron-neutral losses increase as well. When reaching the high density case of (c) the electron-neutral losses are compressed against the neutral source and throughout the outboard plasma edge. A screening effect of preventing the neutrals from ionizing in the core is seen as plasma density is increased. In addition the total neutral losses rise, while the source rate is kept constant.

The neutral interaction region is compressed into the colder edge plasma. Some implications of this compression are that neutral densities are higher in the edge as in case (b) or (c). The increase in electron energy losses comes both from the higher density of both the plasma and neutrals driving up plasma-neutral reactions, as well as a shift from ionization to excitation reactions as discussed earlier in Section 4.3.1. In cases (b) and (c) the neutrals excite and de-excite more frequently leading to more radiation losses. Molecular deuterium is more frequently radiating photons before being broken into atomic deuterium in the higher density edge.

The total losses over the full simulations increase from 498.2 ± 18.2 kW in the low-density case, to 626.2 ± 24.4 kW in the high density case. The mean value scenario has electron

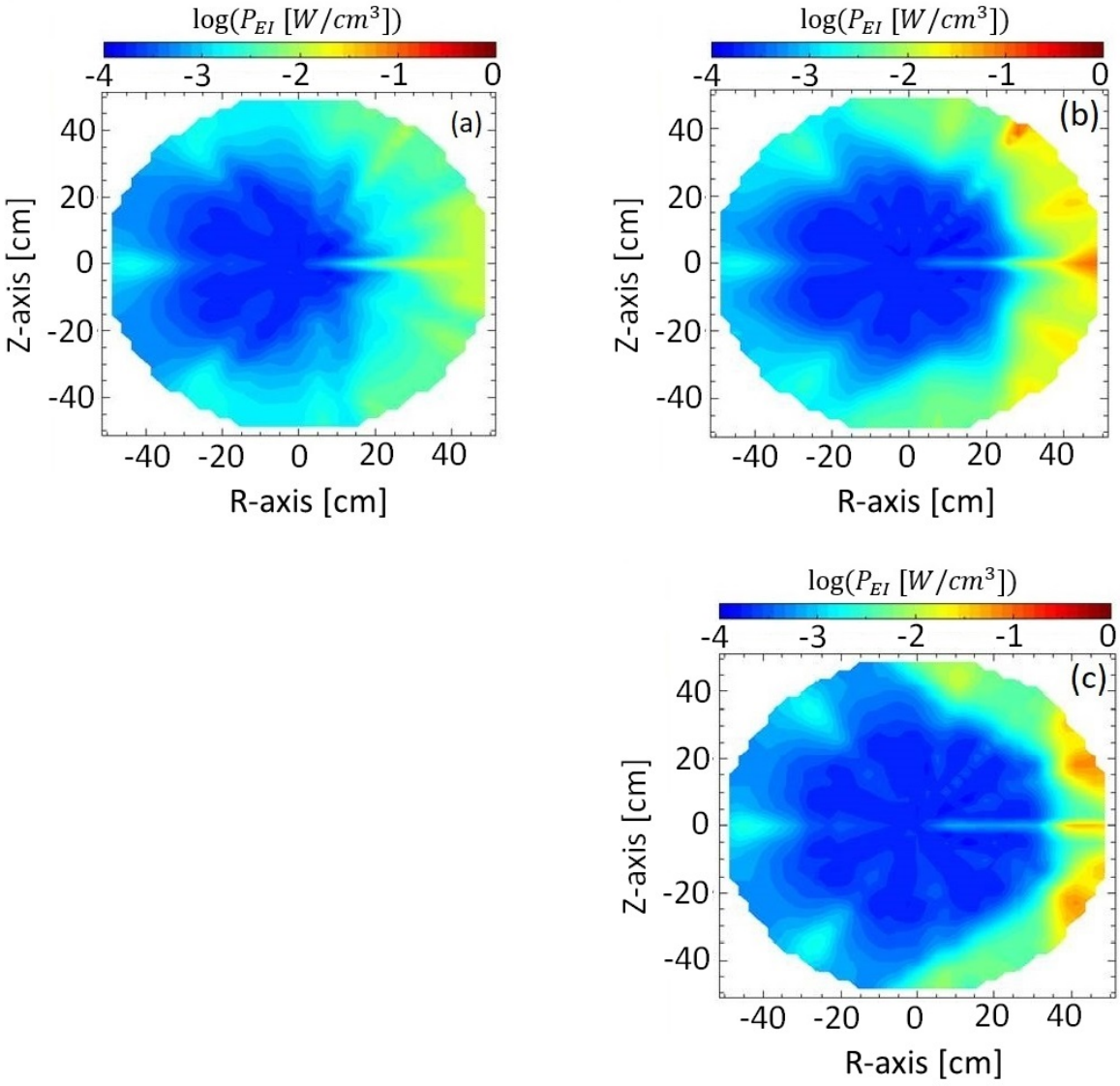

Figure 4.16: Electron excitation in a poloidal cross-section at $\phi = 0°$ of QSH plasma. Outboard is on the right, and the mode is locked towards the outboard midplane. Figure (a) has the lowest edge density of 1x10^{12} $\frac{\#}{cm^3}$, (b) has the average density measured by the measured by the probes of 2.4x10^{12} $\frac{\#}{cm^3}$, and (c) has the edge density of the upper bounds of 4.8x10^{12} $\frac{\#}{cm^3}$.

ionization loss of 589.1 $\pm$ 21.4 kW. While the total neutral power losses increase by only $\sim$ 20% over these density ranges the peak neutral power losses in the region just in front of the limiters rises from 0.006 $\frac{W}{cm^3}$ to 0.079 $\frac{W}{cm^3}$ slightly more than an order of magnitude increase. The errors reported here are statistical errors from EIRENE. As the edge density is raised in simulation the ability of neutrals to penetrate the plasma is reduced. The data from EIRENE is in agreement with the bolometer measurements presented in Figure 3.20 (b) which showed the radiation losses are 8.6 times stronger just in front of the outboard limiter with the mode present, than without.

The charge exchange losses are also computed in EIRENE and follow a similar trend to the electron ionization losses. In addition to P_{cx}, the frequency of charge exchange neutrals being re-ionized was also tallied. In simulations, the first 3000 charge-exchanged neutrals were tracked explicitly to observe how many re-ionize. According to simulation results, 28 $\pm$ 3% of the fast neutrals will re-ionize in the plasma. The error represents the standard error between all the cases. This data provides insight into the transport of charge exchange ions in MST. The likelihood that a fast charge exchange neutral will leave the plasma is three times greater than the likelihood of a collision in a 400 kA QSH plasma. The majority of charge exchange events will cause a neutral to leave the plasma and directly carry away and exhaust plasma energy. It is important to know where the neutrals are undergoing charge exchange and with what temperature ions they collide.

The charge exchange losses in QSH plasmas are shown with edge density at the lower, mean, and upper bounds of probe measurements in Figure 4.17. Here the charge exchange is shown on a logarithmic scale. As the density increases the charge exchange losses transition from a ring-shaped halo, Figure 4.17 (a), towards a partial ring, Figure 4.17 (b), then towards a localized region near the outboard edge, Figure 4.17 (c). In all figures the dominant region of charge exchange is a mid radius volume of plasma. At low density this ring is located at 22<r<38 cm. As the density increaes the ring is pushed out to 25<r<38 cm, and finally at the highest density observed the ring is located 35<r<46 cm. Increasing density expels the neutral population out of the core plasma region. In addition at the highest density cases, most charge exchange becomes localized to the outboard third of the plasma with a "hot spot" in front of the limiter.

The total power losses of the plasma to charge exchange are 262.4 $\pm$ 32.1 kW for the low-density case, 231.1 kW$\pm$26.6 kW for the average density case, and 211.11 $\pm$ 24.8 kW for the high-density case. The change in edge density from the lowest case to the highest case is a factor of 5. This change causes power losses to decrease by 23%, showing a very weak dependence on the edge density. The total volume of plasma effected by the density changes represents 6% of the total volume, however it drives 23% of the losses. While the

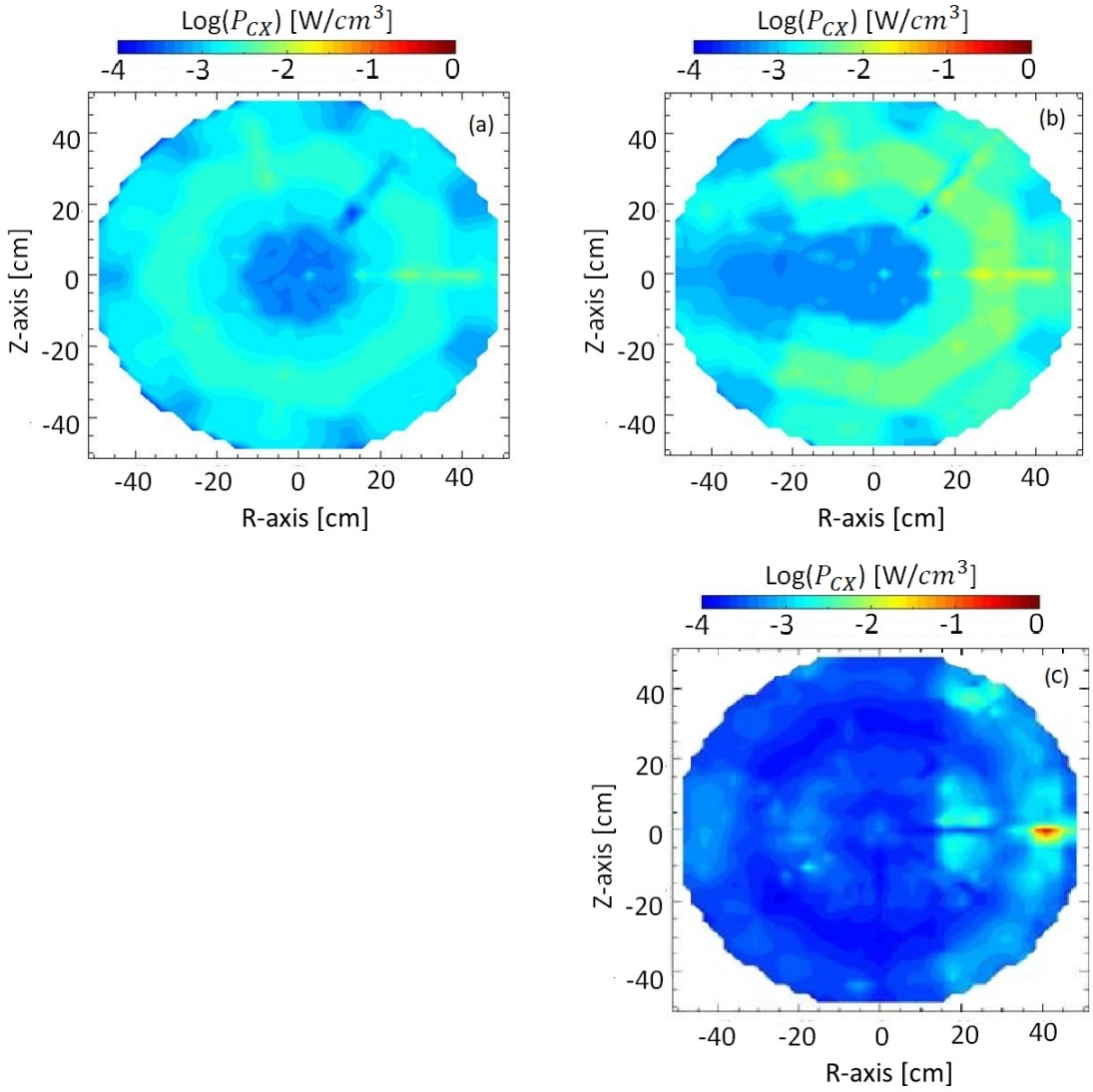

Figure 4.17: Charge exchange in a ϕ=0 degrees poloidal cross-section of QSH plasma. Outboard is on the right, and the mode is locked towards the outboard midplane. Note the log scale for power. The lowest edge density of $1x10^{12}\frac{\#}{cm^3}$ case is shown in (a). The results of the simulation using the average density measured by the measured by the probes of $2.4x10^{12}\frac{\#}{cm^3}$ is shown in (b). Lastly, the edge density of the upper bounds of $4.8x10^{12}\frac{\#}{cm^3}$ is shown in (c).

charge exchange energy loss does not strongly depend on the density, the density does compress the region where charge exchange is occurring. The decrease in P_{cx} with density also comes from the increase in P_{ei} with density as less neutrals are available to charge exchange as they have already become ionized after an electron impact event. The charge exchange cross-section increases slowly with plasma temperature, so neutrals that make it to the core region should be more likely to charge exchange. If any neutrals cross the core plasma region, CX reaction rates decrease as n_i and T_i fall off towards the opposite edge of the machine.

A summary plot for the relative change in the power losses with respect to the edge density is seen in Figure 4.18. This plot includes additional density values in between the mean and extremes, as well as the results of 500 kA plasma simulations. Charge exchange losses drop off very slowly with increasing edge density, while electron losses depend on the species the electrons interact with. Electron-atom losses drop off slowly similar to charge exchange, while electron-molecular losses rise with the edge density. The effect is seen in both at 400 and 500 kA QSH plasmas.

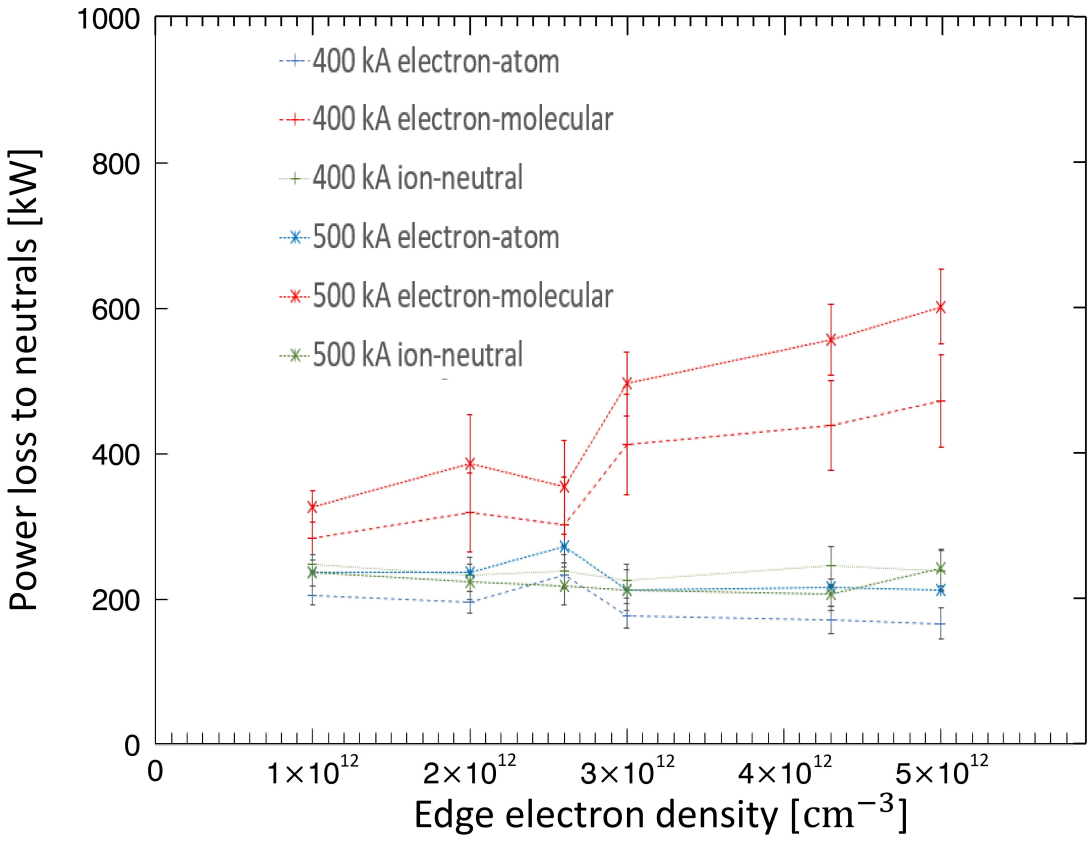

Figure 4.18: Density scaling of plasma-neutral losses is shown for QSH plasmas.

The total plasma neutral losses increase a factor of 1.6. P_{ei} and P_{cx} are weakly sensitive to the edge parameters. Overall in these cases studied in the density scan, 43% of neutral atoms or molecules launched from the limiter source had their first collision within 2 cm. A total of 88% of neutrals had their first interaction within 5 cm of the limiter, and 99.9% of the neutrals launched had experienced a collision by 12 cm into the plasma.

Additionally the power losses from plasma-neutral interactions are shown as either the electron-neutral or electron-molecular component in Figure 4.18. The largest sink for the plasma energy is in the plasma-molecular component at both 400 kA and 500 kA for QSH plasmas. This energy is used to excite, ionize and dissociate the neutrals. As the edge density increases, the overall neutral reaction rate increases in the plasma. Neutrals travel less far from the limiter or wall sources before collisions occur. With more collisions happening closer to the limiters the plasma the neutrals interact with is of slightly lower temperature. This effect causes more neutral molecules to experience multiple collisions before being dissociated and ionized.

While the increase of the edge density does not strongly increase P_{ei} it does significantly shape the locations of plasma-neutral losses. Increasing the edge density contributes a very small change to the total plasma density, but reshapes the locations of the plasma-neutral interactions. Edge density can be used to modulate the region of plasma-neutral interaction and energy losses in the helical core plasma can be minimized. Ionization and radiation losses are increased by this compression effect as the neutral particles recycle additional times before being lost, pumped, or ionized.

4.5.2 Effect of ion temperature on charge exchange

The sensitivity of neutral losses to the shape of the ion temperature profile is investigated. While the electron temperature is measured effectively by Thomson scattering in the core [91], the ion temperature profile is assumed to be at $\frac{2}{3}$ of the electron value for QSH plasmas. The default assumption of $T_i = \frac{2}{3}T_e$ is based on past measurements of ion and electron temperatures in MH MST plasmas, where $T_i = (0.5 - 0.66)T_e$ is common [92]. Knowledge of the T_i is needed for both the reaction rate of the charge exchange collisions, as well as the energy exchange in the charge exchange collisions. The influence of the ion temperature profile on the charge exchange was investigated by running simulations that forced the ion temperature profile to one of two extreme cases and compared to the default assumption of $T_i = \frac{2}{3}T_e$ to gain insight to how the ion temperature and its shape can influence plasma-neutral energy loses.

The first alternative case is a traditional MH axisymmetric profile. This first case is chosen to simulate conditions where the ions do not respond to the onset of QSH state

and would have the same energy and profiles as if the plasma was still axisymmetric. The MH ion temperature profile with QSH electron temperature profile represents a scenario where the ions are too slow or do not respond to the transformation to the QSH state. The second alternative case is a flat ion temperature profile. The flat ion temperature profile represents a possibility that ion and electron temperature are no longer directly linked as the plasma transitions to QSH. Ongoing work on MST suggests the ion temperature profile may be flatter in QSH then MH, so the profile chosen is the extreme version of this result, completely flat. The results are shown below in Figure 4.19 (a), no-ion response, and Figure 4.19 (b), flat ion profile. The QSH recycling source is unchanged. Neutrals are sourced in helical distribution based on experimental measurements of the QSH state discussed in Section 3.2.

The results of using a standard 400 kA MH ion temperature profile is shown in Figure 4.19 (a). By switching from the 400 kA QSH profile to this ion temperature profile, the peak T_i falls from nearly 400 eV to 220 eV. This brings the integrated charge exchange losses down to just 84 ± 6 kW for this plasma. The charge exchange interactions, in this case, are outboard localized mostly occurring near the localized neutral sources. The peak region of charge exchange losses occurs at 13 cm inside the plasma on the mid-plane. Compared to the previous QSH case, the power losses to charge exchange are 64% lower when utilizing a MH ion temperature profile.

Using a flat 300 eV ion temperature profile instead of a V3Fit reconstruction has a noticeable influence on the charge exchange losses. Results of EIRENE simulations using a flat ion temperature profile are shown in Figure 4.19 (b). Using this flat profile, P_{cx} remains closer to standard QSH simulations than to the alternative MH profile. With a flat ion temperature profile, the charge exchange losses begin to mirror the neutral density profile for the QSH plasma (compare to Figure 4.12). As the charge exchange losses begin to mirror the neutral density distribution this suggests that the helical temperature profiles can influence the shape of the charge exchange profiles. Small vertical asymmetry is seen due to the pumping of neutrals on the lower quarter of MST. The total charge exchange losses in this scenario are 172 ± 8 kW. The flat ion profile distributes the charge exchange losses over the greatest plasma volume of the cases studied.

4.5.3 MH plasma-neutral losses

MH plasma-neutral losses were modeled in the full plasma volume with EIRENE. The results of this section are used to contrast the 3D QSH state with the standard MH state. In addition, the evaluation of plasma-neutral losses in MH inform how the energy balance may be different between axisymmetrical and 3D states.

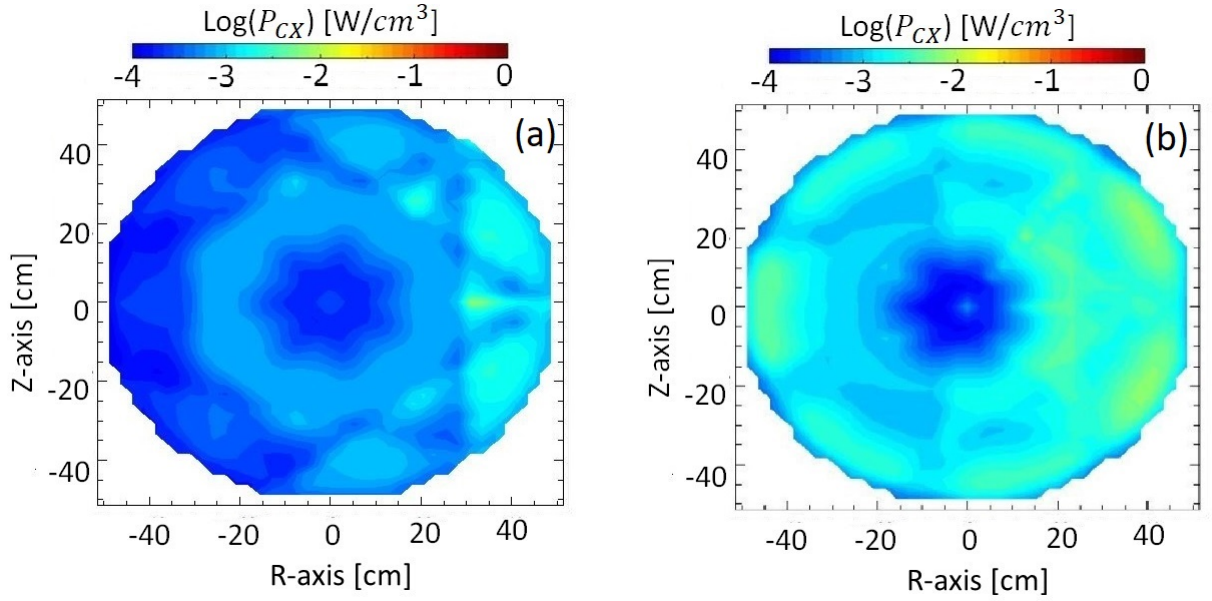

Figure 4.19: CX losses from a cross-section with mode-locked outboard, in a helically sourced plasma with a 400 kA MH ion temperature profile are shown on the left. CX losses are significantly reduced if the ions are not assumed to increase in temperature as electrons do during the QSH transition. Charge exchange losses in a QSH plasma with a flat ion temperature profile of 300 eV from r/a=0 to r/a=0.9, and then linear to 0 at the edge are shown on the right. This is the hypothetical case where the QSH transition flattens the ion temperature profile.

MH plasma-neutral interactions have a toroidally symmetric outboard localized profile for both electron and ion losses. 200 kA MH plasmas have the largest neutral populations in MST as shown in Figure 4.14. The electron-neutral losses of a 200 kA standard MH plasma are shown in Figure 4.20 (a). A toroidally averaged poloidal cross-section is shown in the Figure. Outboard is on the right side. The limiter neutral source still exhibits the small variation presented in Chapter 3. An inboard-outboard asymmetry is observed, with the greatest loss near the outboard limiter. The electron-neutral losses are almost negligible inside r/a=0.6. The plasma-neutral loss region occupies a large crescent of the outboard plasma, extending 90 degrees in either poloidal direction from the outboard. Losses from ionization of wall fueled and recycled neutrals are present in the first 3 cm of the edge. The average volumetric power loss in the edge (r/a>0.9) is 2.4 mW/cm^3. Electron neutral losses in the region of r/a<0.4 contribute less than 0.1% of the total power losses in 200 kA plasma. On average, 200 kA standard MH plasma produces electron-neutral losses of 234 ± 28 kW.

A 400 kA MH plasma is shown in Figure 4.20 (b), which is a toroidal average of the full MH simulation. With higher current, an increase in electron temperature causes the

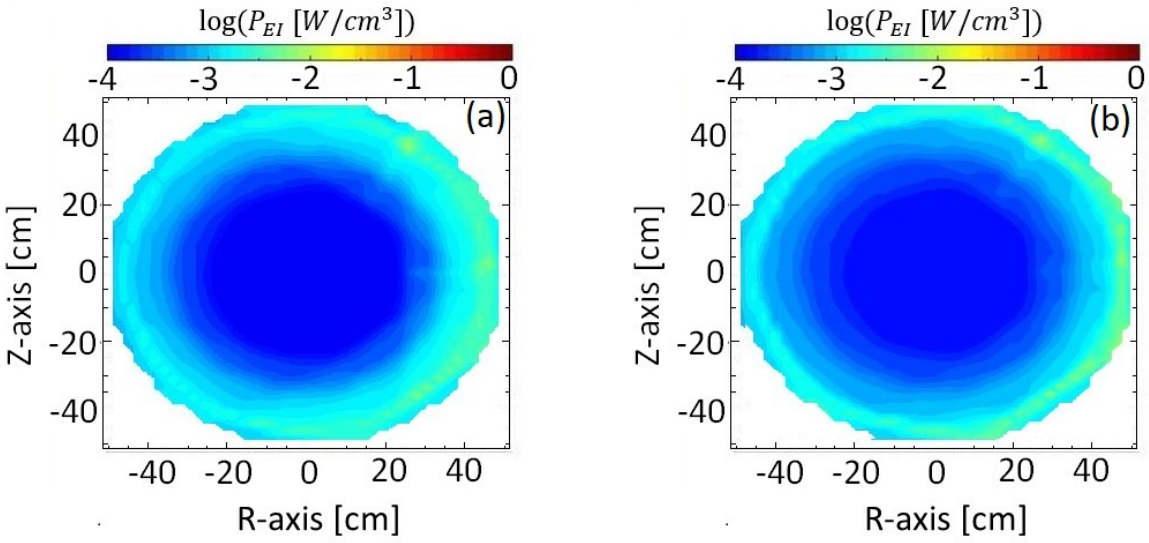

Figure 4.20: Toroidally averaged cross-section showing electron-neutral losses in a 200 kA standard plasma is shown on the left. Electron-neutral losses account for approximately 235 kW of exhaust power, a small fraction of the Ohmic input power. 400 kA standard plasma electron-neutral losses are shown on the right. Electron-neutral losses account for approximately 170 kW of exhaust power, a smaller fraction of the Ohmic input power than lower current cases.

ionization and electron impact losses to increase. The boundary of the region of interaction move outwards from r/a=0.4 to r/a=0.56 as the current was raised from 200 kA to 400 kA. The average volumetric power loss in the region of r/a>0.9 is 8.6 mW/cm^3, nearly three times higher than in the 200 kA case. The mean free path for ionization, λ_i , has decreased from 7.8 to 4.5 cm compared to the 200 kA case. The mean free path of ionization was calculated in EIRENE by sampling 10,000 neutral particles (atoms and molecules) randomly, and following the particles paths, noting the collisions that occur. Once an ionization event occurred the distance between the particles current location and the source was calculated. As many of the sample neutrals were molecules, each atom was tracked after dissociation. Particles that underwent a charge exchange or were lost to pumping or the material surfaces were rejected from the computation. The outboard half of the plasma volume has an order of magnitude more plasma-neutral energy loss than the inboard, primarily from the pirmary neutral source being outboard localized. The crescent-shaped region of ionization seen in the lower current case no longer exists due to the more rapid ionization of the neutrals in 400-kA plasmas. The 400 kA MH plasmas have total electron-neutral losses of 168 $\pm$ 17 kW.

The higher temperature of these plasmas keeps the ionization region in the edge. As

seen in the camera measurements (Section 3.3.1), the neutral source decreases with an increase in plasma current The neutral source in the 400 kA case is 3.5 ± 0.6 times less than the 200 kA case. Reduction of neutral source is the primary cause of the decrease in electron-neutral losses, which fall by a factor of 1.4 ± 0.1 The neutral source decreases more significantly than the electron ionization losses as the plasma current is raised. Several processes contribute to this behavior. The first is that much more direct ionization is occurring at a higher temperature, 48% of the neutral particles are ionized in the 400-kA simulation compared to 42% in 200 kA cases. Less excitation of neutrals is occurring in higher current plasmas. The fraction of neutrals excited by electron interactions falls from 35% in 200 kA to 28% in 400 kA. In higher current plasma, more charge exchange neutrals are lost to the wall, reducing the recycling population. With fewer neutrals in the edge undergoing multiple ionization and recombination events overall power losses are decreased.

Charge exchange losses evaluated for the MH case show an overall lower loss rate due to charge exchange than in QSH plasma. Charge exchange losses scale with I_p; in addition, the 400 kA MH case is compared relative to the 400 kA QSH case. The results of the 200 kA simulation are shown in Figure 4.21 (a). The charge exchange losses are plotted in a toroidally averaged cross-section. At 200 kA the ion temperature is peaked at 180 eV in the central plamsa and falls off to 20 eV in the edge region. These plasmas have the least amount of ion energy available for neutrals to remove by collisions. The primary region of charge exchange occurs on an annulus from r/a=0.62-0.84. There is an observable up-down asymmetry to this annulus. This is a result of a small up-down asymmetry in the neutral profile from increased neutral losses to pumping in the lower half of MST.

The results of the 400 kA simulation are shown in Figure 4.21 (b). Unlike the electron-neutral losses, the charge exchange losses increase with plasma current. This trend was also observed in the QSH cases. The energy losses by charge exchange in a 200 kA plasma are low at 82 ± 4kW; however, once the plasma current and corresponding plasma temperature are raised, charge exchange losses begin to exceed the electron losses. In MH plasma the central plasma temperature rises from 180 to 270 eV, and the edge temperature rises by 5 eV as well. The energy exchanged per charge exchange collision rose from an average of 26 eV to 74 eV. At 400 kA the charge exchange losses are 188 ± 16 kW, these losses further increase to 260 ± 34 kW at 500 kA.

4.5.4 Fractional power losses

Having established the absolute magnitude of the plasma-neutral losses for a variety of plasma conditions the relative contribution the neutrals made to the energy balance was

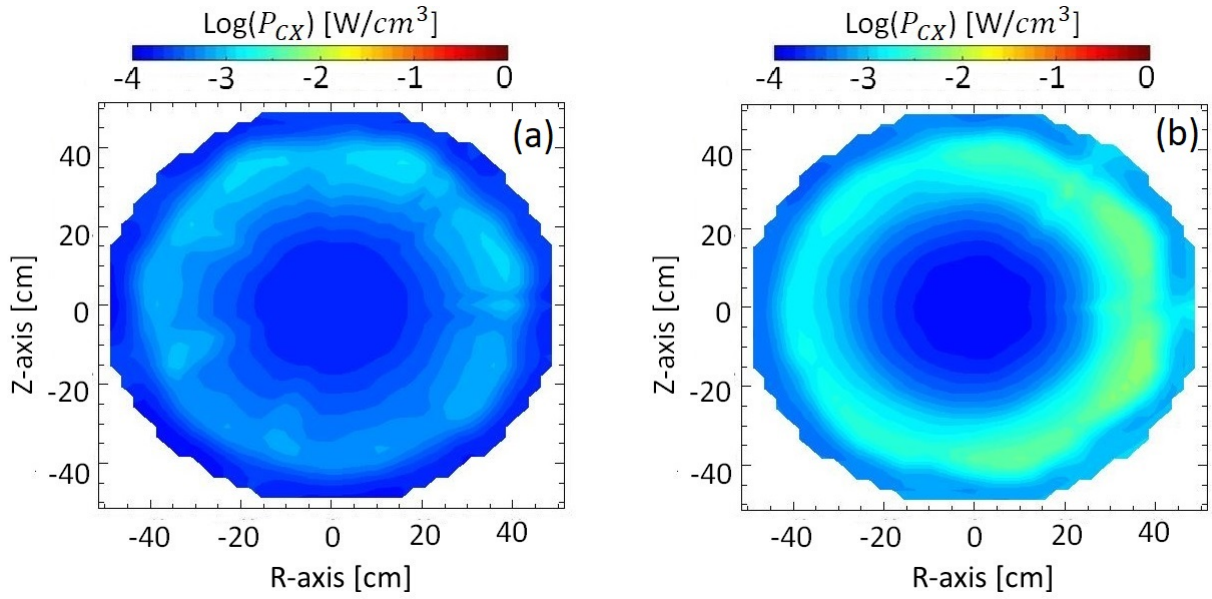

Figure 4.21: Toroidally averaged cross-section showing charge exchange losses in a 200 kA standard plasma are shown on the left. Charge exchange losses for 200 kA MH plasmas are small at 80 kW. Toroidally averaged cross-section showing charge exchange losses in a 400 kA standard plasma are shown on the right. Charge exchange losses peak in the mid-radius and total losses are 200 kW for 400 kA MH plasmas.

computed. In order to assess the fractional power loss caused by neutral particles in MST, the total Ohmic input power was measured. This Ohmic input power is the only source of input energy into MST and represents the upper limit for what may be exhausted from the system. Plasma discharges within 10% of a target value of 200, 300, 400, or 500 kA I_p, n_e of $0.9 - 1.1\text{x}10^{13}\frac{\#}{cm^3}$, and reversal parameter of F from -0.19 to -0.21 are selected to build the data set for the MH plasma regimes . The QSH discharges were similarly representative of MST helical discharges with target parameters of F=0, $n_e = 0.4 - 0.6\text{x}10^{13}\frac{\#}{cm^3}$ and within 10% of either 400 or 500 kA. Two hundred discharges per parameter set were collected. The Ohmic input power was calculated for the flattop average of these discharges when the plasmas are steady-state. The results of the Ohmic power analysis are shown in Figure 4.22. Ohmic input power is shown in two plots, one for MH and one for QSH with the same y-scale for comparison.

When examining the MH cases, input power rises slowly with plasma current as does variability in the input power. The variability is presented as the mean $\pm$ standard deviation on the Figures. One cause of the variability of the input power in MH plasmas was the presence of sawteeth during the flattop period. These events increase the input demand to sustain the plasma. They are short-lived and unpredictable. QSH plasmas have no

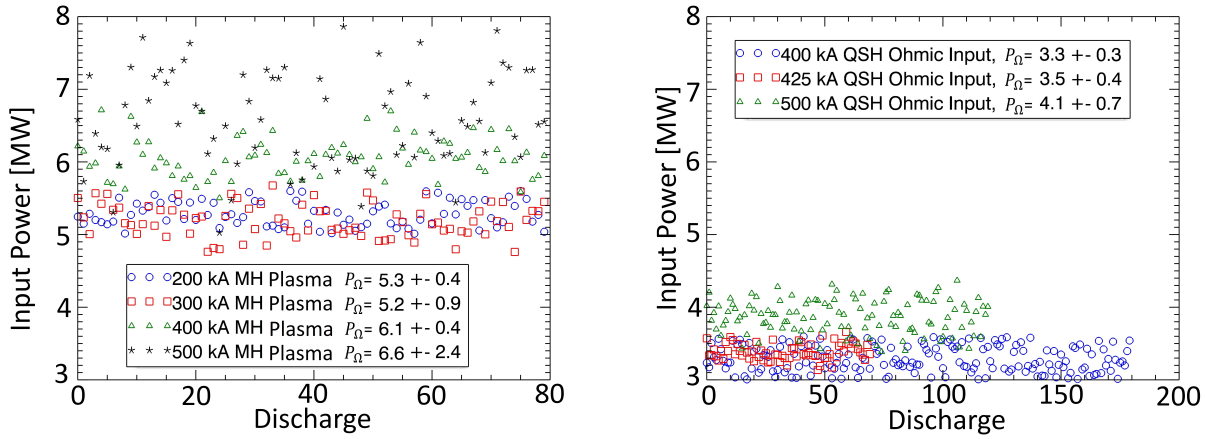

Figure 4.22: The ohmic input powers for MH and QSH discharges are shown. MH discharges are representative of 1x$10^{13}\frac{\#}{cm^3}$, F=-0.2 discharges, while the QSH discharges were conducted at 0.5x$10^{13}\frac{\#}{cm^3}$ and F=0. A larger variation of the input power occurs as plasma current is raised. QSH discharges overall require lower input power to sustain, reflective of their enhanced confinement.

sawteeth during their flat top, and this is reflected in the reduced variance of the QSH input power. Other sources of variation were controlled for in the selection of discharges. Discharges with density or current excursions were excluded from the data set. At any particular I_p the MH plasma requires approximately 60% more input power than a QSH plasma.

Total plasma-neutral losses between QSH and standard plasmas are of similar magnitude, with a factor of 3 difference between extreme cases. The energy losses discussed in this Chapter are summarized in Figure 4.23. Plasma-neutral losses are placed into two bins, P_{CX} and P_{EI}, in the figure. The electron impact (EI) losses are the sum of all electron collisions with neutral molecules and atoms, while charge exchange (CX) losses represent the sum of power lost from ion-neutral collisions. In both MH and QSH plasmas as I_p is increases there is a shift of the pathway for energy losses from electron impact collisions to charge exchange. Charge exchange losses are found to increase strongly with plasma current. Increasing the plasma current raises plasma T_e and T_i , which, in turn, allows for more energy to be lost per collision. The mean energy lost per charge exchange event is shown below in Table 4.1. A configuration number is used to label the different types of discharges in MST. Configurations 1-4 are MH, and 5 and 6 are QSH plasmas. The charge exchange losses per collision are larger in the higher current plasma, where the 500 kA plasma has 3x the average energy lost per charge exchange event as the 200 kA case. Electron-neutral losses decrease as I_p increases in standard plasmas. There are two effects

going on here, the neutral source is decreasing as I_p rises, and the plasma temperature is increasing. As I_p increases, the neutral source decreases, directly lowering the number of neutrals interacting with the plasma. The hotter plasma at higher I_p also have lower interaction rates which further drive down power losses. The increasing plasma temperature shifts the reaction rates to favor charge exchange.

Configuration #		Mean energy lost per charge exchange (eV)	EIRENE statistical) error (eV)
1	200 kA MH	26	5
2	300 kA MH	38	6
3	400 kA MH	53	6
4	500 kA MH	74	7
5	400 kA QSH	76	11
6	500 kA QSH	82	12

Table 4.1: EIRENE results for charge energy exchanged for charge exchange events.

Fractional power loss is chosen to compare the plasma-neutral losses between QSH and MH plasma. Neutral energy losses are normalized by the average input power used to sustain the RFP discharge. Neutrals provide a significant exhaust path in QSH plasmas, both from higher absolute values of energy lost to neutral interaction and from the lower input power of the QSH state. Power losses caused by plasma-neutral interactions in MST account for $19-29\%$ of the energy losses in QSH plasmas and 8% of energy losses in MH plasma, this is shown in Figure 4.24. In QSH plasma radiation losses to the wall surface amount to 13-21% of total power losses, peaking at 780 kW in 500 kA QSH plasmas. In MH plasma the radiation losses range from 3-9% peaking at 550 kW in 500 kA MH plasmas. In MH plasma, the neutral plasma losses are lower than the QSH plasma at all current levels. Both plasma configurations have comparable charge exchange losses at 400 kA and 500 kA. These plasmas have different edge and central T_i and n_i. In the QSH case as a result of higher edge density, charge exchange occurs in the edge region. In MH plasma, a lower edge density allows neutrals to transport deeper into the plasma where charge exchange occurs. The mean radius value in 400-500 kA MH plasma for charge exchange to occur is $r/a=0.64$, while in QSH the mean radius is $r/a=0.74$. This allows neutrals in MH plasma to access hotter plasma and remove more energy per collision.

The outboard locked source produces a halo or crescent region around the edge of the plasma in both MH and QSH where the bulk of charge exchange losses occur. Ion power losses rise with plasma current, a direct result of higher ion temperatures. Ion heating and temperature have been generally found to be larger at higher plasma currents. It is observed that regardless of the plasma current, while in an MH state, the plasma-neutral

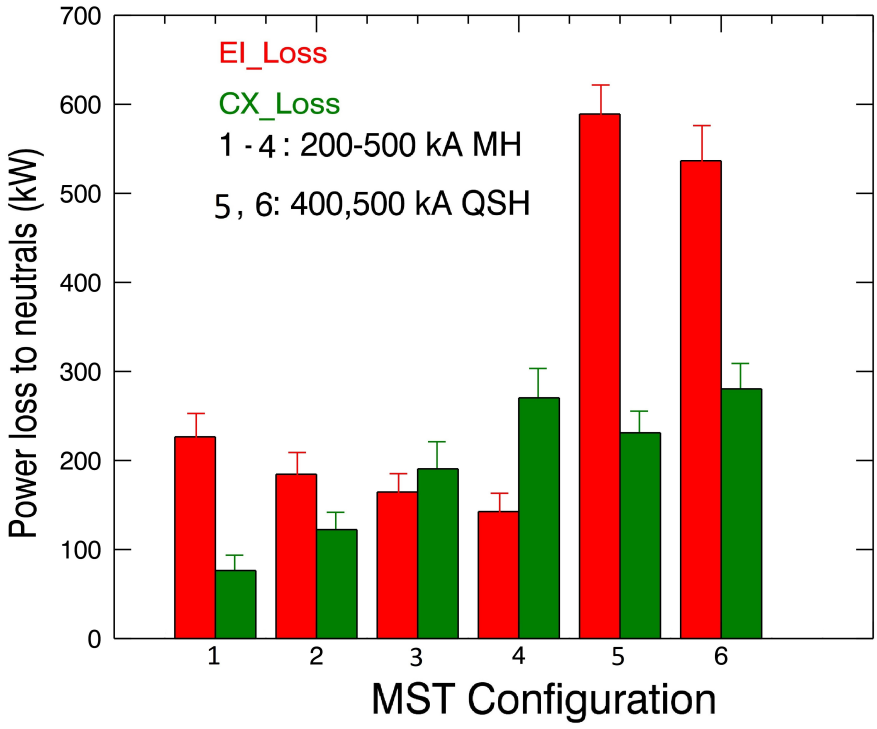

Figure 4.23: A summary of plasma-neutral losses by machine operation, in total power losses during the steady-state part of an MST discharge is shown. CX losses increase with the plasma current, while the QSH state has much more significant ionization losses due to increased recycling from a neutral cloud produced between a pressure bulge in the edge and the limiter.

losses are steady at 8% of the input power. There is no obvious physical reason for this behavior. In QSH plasma, the plasma-neutral interactions make up a more substantial loss of total plasma energy, with the maximum value occurring at 29% for 400 kA QSH plasma.

There is an additional current dependence for QSH plasma where the 500-kA plasma loses less relative energy to plasma-neutral interaction. In 500 kA QSH compared to 400 kA QSH the total input power is increased by 25%. The electron-neutral losses decrease by 10% while charge exchange losses increase 27%. As only two QSH plasma currents were modeled, it is difficult to predict how the data will trend with further increase in I_p. Only two plasma currents were modeled as the QSH operation range in MST is 400-500 kA. The extremes of this range were modeled. It would have been possible to collect and reconstruct data within this range. Attempting to form QSH plasmas at lower I_p would lead to less consistent QSH plasma, if any, as the likelihood of QSH scales with I_p. MST is nominally operated at or below 500 kA for operational and safety concerns.

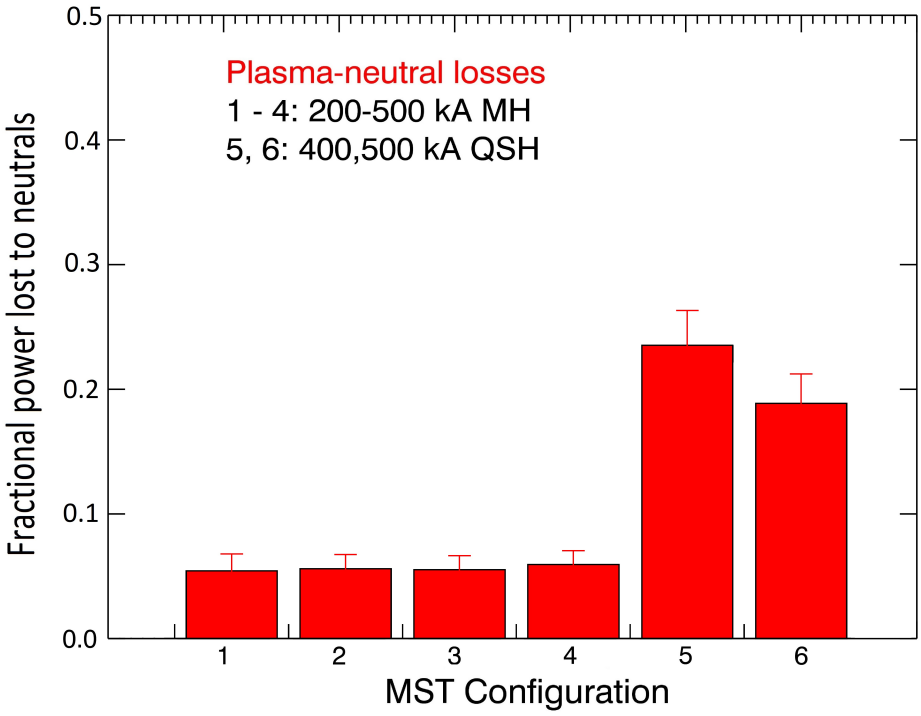

Figure 4.24: A summary of plasma-neutral losses by machine configuration. Neutral losses are relatively small during standard MH plasmas, however, due to more intense recycling and improved confinement in QSH plasma, the neutral loss terms rise to about 1/5 of total Ohmic power.

In summary, the question of the contribution neutral particles make on the power balance is answered. For a MH plasma the contribution is small and could be considered negligible in the overall power balance. However in a QSH plasma it is shown that the plasma-neutral interactions represent a significant exhaust pathway for plasma energy. One reason for the larger power losses in QSH plasma is a strong PWI that occurs from an edge pressure bulge contacting the limiter. This produces a strong localized recycling source for which the neutrals have direct access to a hot dense edge.

Chapter 5

Summary and Future Work

5.1 Summary and conclusion

The Madison Symmetric Torus (MST) reversed field pinch (RFP) has been operated for over 30 years, and in this time the focus has been on the physical processes determining confinement and transport in the plasma core domain. Previously, the contribution of the neutral particles to the energy balance was unknown in an RFP. After the systematic investigation of the plasma edge domain conducted for this thesis, the RFP energy balance is now more completely understood. Newly developed camera diagnostics, aided by first time probe measurements, informed 3D modeling of the MST plasma-neutral interactions. Neutral source distributions are quantified and the energy losses from plasma-neutral interaction are modeled based on direct input from relevant experimental measurements. When the plasma transitions to the quasi-single helicity (QSH) state the edge was found to become helical, with localized plasma-wall interaction (PWI) in contrast to the uniform PWI of MH plasmas.

The QSH edge plasma was directly characterized with Langmuir probes for the first time. An edge pressure bulge was found to be phase aligned with the core magnetic mode. These pressure bulges created localized PWI hot spots. Orientation of these 3D structures is possible with the MST active feedback system, enabling probe measurements of the 3D edge. Neutral particles, produced from PWI, have access to hot, dense plasma directly when this pressure bulge contacts the limiters. In QSH plasmas, the plasma-neutral losses become localized. Up to 50% of the total interactions occurred in the pressure bulge, even though it occupies only 5-8% of the edge. Control of this pressure bulge could enable future RFPs to be operated such that localized PWI units like divertors with active pumping can be implemented. This would allow to actively manipulate and control of the neutral source level in a RFP plasma.

The combination of interferometry measurements and phase control of the QSH mode

enabled fueling studies to be performed on the 3D edge. Particles are found to ionize most efficiently when injected directly into the helical edge pressure bulge. The pressure bulge quickly expelled these extra particles, leading to higher recycling and increased ionization losses. Neutrals repeatedly ionized and recombined after being expelled from the material surface. If gas was injected into other regions of the QSH plasma, the particles, while less likely to ionize, are retained longer in the plasma. Confinement times between gas injected directly into the pressure bulge (~6 ms) were half that of gas injected elsewhere in the edge (~12 ms). The particle source required to sustain a QSH plasma was greater for a given density than an MH plasma while higher plasma fluxes impacted the limiters localized by the edge pressure bulge.

A new camera system diagnostic, with high spatial resolution, was developed to measure the photon flux from over 85% of the MST edge. Camera measurements have enabled the systematic analysis of the MST edge in both an axisymmetric state and a 3D helical state. The magnitude of neutral particle fluxes produced in MST were measured in the range of Γ=0.5x10^{17} to 3.2x10^{20} $\frac{\#}{s}$ depending on I_p and the magnetic setup of the plasma. The highest recycling fluxes were observed in regions of the limiter adjacent to the QSH helical pressure bulge. The plasma facing components in MST have been measured to have a moderate pumping capability. The recycling coefficient was shown to have a phase dependency in QSH dipping down from a nominal value of 0.9 to 0.75 when the helical bulge was aligned to the limiter. Camera measurements revealed a highly 3D PWI pattern in QSH plasmas in contrast to a smooth PWI pattern in MH plasmas. In the future, these cameras could be used as a survey spectrometer for impurity monitoring on MST and may help with erosion studies.

Conversion of camera measured photon fluxes into recycling fluxes was accomplished by analysis of excitation and radiative decay for the D_α emission line. In order to obtain an accurate conversion between the photon flux and the corresponding neutral flux, modeling of the system in EIRENE produced an effective S/XB coefficient. Probe measurements of the edge data alone were insufficient to accurately interpret camera images. A synthetic image module was implemented into the model of MST for EIRENE. This enabled a closed-loop verification of the model by comparing the experimental images and D_α signals to the synthetic images and D_α signals produced by EIRENE. This method produced models which agreed with experiment to $10-60\%$. Strong agreement between model and experiment supported that the power losses predicted by EIRENE accurately represent the plasma behavior.

The power lost in plasma-neutral interactions depends on both the plasma conditions and neutral sources. In QSH plasma, fewer neutral particles need to be injected to sustain

the plasma density. The edge conditions influenced total power losses. For example, if edge density increased by a factor of 5, local plasma-neutral losses increased by an order of magnitude. Higher edge densities confined the neutral particles to the edge. Rather than ionize once and become part of the plasma they underwent multiple ionization and recycling events contributing to more energy loss. Charge exchange losses also were influenced by the ion temperature profiles. As these profiles are not directly measured, assumptions were made. It was assumed that $T_i \propto T_e$ and T_e was directly measured for both QSH and MH plasmas. In QSH plasmas, two other ion profiles were considered: a flat profile and a unaltered MH profile. These alternative cases provide insight to how the plasma-neutral losses may change if ions responded as strongly to the QSH transition as electrons. Regardless of the shape of the ion profile chosen, in QSH plasmas the neutral source distribution determined the locations of the plasma-neutral interactions, while the ion profiles only influenced the energy transferred in a charge exchange event. In MH plasmas, neutral power losses were small at 8% of the energy injected into the system. In QSH plasmas the neutral contribution was more significant, approaching 30% of the input power. Modeling results indicate that the increase in the fraction of plasma-neutral losses is a result of more excitations per neutral in the edge plasma.

The discoveries made in this work suggest that RFPs may be able to utilize self-organized 3D states to control the plasma-neutral interaction. The QSH state allows for RFP plasmas to be operated at higher levels of electron thermal confinement. This higher level of thermal confinement is accompanied by additional challenges in exhausting thermal energy and sustaining plasma density. The edge pressure bulge allows for the possibility to build plasma wall interaction components that steer the heat flux and control plasma neutral interaction such that the hot core is shielded from recycling neutrals. Reducing the neutral source by locking the QSH edge pressure bulge onto a low recycling material such as tungsten will reduce plasma-neutral losses by eliminating multiple ionization events for recycled fuel particles. A new method of fueling the plasma would then be required to sustain the plasma density. It was shown that gas injection fueling of the 3D plasma is phase dependent, with the fuel uptake higher when away from the edge pressure bulge. Deuterium pellets could be directly injected to the plasma axis, outside the helical core, where the neutrals would ionize a single time. Alternatively, the screening effect the pressure bulge has on recycling neutrals should be further studied. It may be possible to increase the screening effect to provide a boundary layer between the recycling source and the hot plasma core.

5.2 Future work

The most immediate question that arises from this work is the need to identify the mechanism that creates the edge pressure bulge. The EMC3-EIRENE code [72] would enable the study of the plasma response to a localized neutral source. EMC3-EIRENE was not used in this work because it is unable to handle the reversed field magnetic geometry of the RFP. However, the QSH plasma is almost always formed with F=0, non-reversed, in MST. By modeling the plasma response to the neutrals, further insights may be gained on feedback mechanisms that exist in the RFP edge. In addition, EMC3-EIRENE can support the modeling of the QSH plasma to impurity fluxes, such as carbon or aluminum. The impurity level in MST was found to be small when surveyed, but this may not always be the case. In the event an RFP is to be designed with a metal, such as tungsten, EMC3-EIRENE could be used for predictive modeling of the plasma edge. Synthetic image quality also is likely to be improved by using the fuly synthetic coupled plasma-neutral modeling in EMC3-EIRENE. Utilizing EMC3-EIRENE to capture the plasma response in the edge may lead to more realistic synthetic images.

The boundary viewing cameras are too slow to reliably capture some RFP events, such as sawtooth crashes. Another path for future work could be to develop a scheme for capturing fast irregular events on MST with the boundary viewing cameras. Even though the current camera system is limited to a maximum frame rate of 1 $\frac{\mathrm{frame}}{\mathrm{ms}}$, fast phenomena may still be captured if a proper trigger system is developed. The effects of sawteeth on the edge have been captured randomly at a frequency of about 3/1000 frames when observing standard plasmas. These sawteeth events cause a brief spike in the plasma-wall interaction. This research could inform the dynamics of sawteeth on the edge plasma, PWI, and particle balance. Pursuing this path of research would lead to understanding the temporal dynamics in the neutral particle balance in MH plasmas.

Fueling schemes could more extensively modeled. This work studied edge fueling in helical plasma exclusively. While it will likely be difficult to extend the edge fueling work to pulsed poloidal current drive (PPCD) discharges, the oscillating field current drive (OFCD) scheme [93], an attempt to drive current in MST for the prospect of long pulse operations, could be investigated. MST utilizes natural recycling for sustaining the discharge. In a future long-pulse RFP, the depletion of the wall inventory needs to be understood. The diagnostics and techniques developed in this work enable detailed study of the temporal dynamics of the wall as a particle reservoir. It would be interesting to develop fueling schemes for such long-pulse plasma, either QSH or OFCD, in greater detail. A long-pulse experiment will need to refuel during the shot. New sources of fuel will need to be injected

into the plasma. Other than wall and gas injection fueling, a pellet injector exists on MST. The pellet injector can be used to study the QSH or OFCD response to pellet fueling. The stability of QSH, with respect to a back transition occurring, could be studied as pellet fueling increases. Changing the source of neutrals to the core plasma may also radically change the neutral profiles, as well as plasma-neutral exhaust pathways. These would need to be reevaluated for pellet fueled plasma.

Bibliography

[1] J. Sarff, A. Almagri, J. Anderson, M. Borchardt, W. Cappechi, D. Carmody, K. Caspary, B. Chapman, D. D. Hartog, J. Duff, S. Eilerman, A. Falkowski, C. Forest, M. Galante, J. Goetz, D. Holly, J. Koliner, S. Kumar, J. Lee, D. Liu, K. McCollam, M. McGarry, V. Mirnov, L. Morton, S. Munaretto, M. Nornberg, P. Nonn, S. Oliva, E. Parke, M. Pueschel, J. Reusch, J. Sauppe, A. Seltzman, C. Sovinec, D. Stone, D. Theucks, M. Thomas, J. Triana, P. Terry, J. Waksman, G. Whelan, D. Brower, W. Ding, L. Lin, D. Demers, P. Fimognari, J. Titus, F. Auriemma, S. Cappello, P. Franz, P. Innocente, R. Lorenzini, E. Martines, B. Momo, P. Piovesan, M. Puiatti, M. Spolaore, D. Terranova, P. Zanca, V. Davydenko, P. Deichuli, A. Ivanov, S. Polosatkin, N. Stupishin, D. Spong, D. Craig, H. Stephens, R. Harvey, M. Cianciosa, J. Hanson, B. Breizman, M. Li, and L. Zheng, "Overview of results from the MST reversed field pinch experiment," *Nuclear Fusion*, vol. 55, no. 10, p. 104006, 2015.

[2] R. Lorenzini, E. Martines, P. Piovesan, D. Terranova, P. Zanca, M. Zuin, A. Alfier, D. Bonfiglio, F. Bonomo, A. Canton, S. Cappello, L. Carraro, R. Cavazzana, D. F. Escande, A. Fassina, P. Franz, M. Gobbin, P. Innocente, L. Marrelli, and H. Zohm, "Self-organized helical equilibria as a new paradigm for ohmically heated fusion plasmas," *Nature Physics*, vol. 5, pp. 570–574, 06 2009.

[3] P. C. Stangeby, *The Plasma Boundary of Magnetic Fusion Devices*. Bristol and Philadelphia: Institute of Physics Publishing, 1 ed., 2000.

[4] J. Wesson, *Tokamaks; 4th ed.* International series of monographs on physics, Oxford: Oxford Univ. Press, 2011.

[5] F. F. Chen and H. Torreblanca, *Introduction to Plasma Physics and Controlled Fusion, 2nd edition*. New York: Plenum Press, 1984.

[6] G. Fiksel, S. C. Prager, W. Shen, and M. R. Stoneking, "Measurement of magnetic fluctuation induced energy transport," *Phys. Rev. Lett.*, vol. 72, pp. 1028–1031, Feb 1994.

[7] H. Tsui, C. Ritz, G. Miller, J. Ingraham, C. Munson, K. Schoenberg, and P. Weber, "Fluctuations and transport in a reversed field pinch edge plasma," *Nuclear Fusion*, vol. 31, no. 12, p. 2371, 1991.

[8] E. Martines, V. Antoni, D. Desideri, G. Serianni, and L. Tramontin, "Energy flux driven by electrostatic turbulence in the RFX edge plasma," *Nuclear Fusion*, vol. 39, no. 5, p. 581, 1999.

[9] P. Scarin, N. Vianello, M. Agostini, G. Spizzo, M. Spolaore, M. Zuin, S. Cappello, L. Carraro, R. Cavazzana, G. D. Masi, E. Martines, M. Moresco, S. Munaretto, M. E. Puiatti, M. Valisa, and the RFX-mod Team, "Topology and transport in the edge region of RFX-mod helical regimes," *Nuclear Fusion*, vol. 51, no. 7, p. 073002, 2011.

[10] S. Hokin, "Particle and energy transport simulations of reversed field pinch plasmas," *Nuclear Fusion*, vol. 37, no. 11, p. 1615, 1997.

[11] D. Reiter, "The EIRENE code," 1992. Accessed June. 23, 2015.

[12] R. J. Groebner, M. A. Mahdavi, A. W. Leonard, T. H. Osborne, G. D. Porter, R. J. Colchin, and L. W. Owen, "The role of neutrals in high-mode (H-mode) pedestal formation," *Physics of Plasmas*, vol. 9, no. 5, pp. 2134–2140, 2002.

[13] F. Wagner, J. Baldzuhn, R. Brakel, R. Burhenn, V. Erckmann, T. Estrada, P. Grigull, H. J. Hartfuss, G. Herre, M. Hirsch, J. V. Hofmann, R. Jaenicke, A. Rudyj, U. Stroth, and A. Weller, "H-mode of W7-AS stellarator," *Plasma Physics and Controlled Fusion*, vol. 36, pp. A61–A74, jul 1994.

[14] G. Spizzo, G. Pucella, O. Tudisco, M. Zuin, M. Agostini, E. Alessi, F. Auriemma, W. Bin, P. Buratti, L. Carraro, R. Cavazzana, G. Ciaccio, G. D. Masi, B. Esposito, C. Galperti, S. Garavaglia, G. Granucci, M. Marinucci, L. Marrelli, E. Martines, C. Mazzotta, D. Minelli, A. Moro, M. Puiatti, P. Scarin, C. Sozzi, M. Spolaore, O. Schmitz, N. Vianello, and R. White, "Density limit studies in the tokamak and the reversed-field pinch," *Nuclear Fusion*, vol. 55, no. 4, p. 043007, 2015.

[15] R. N. Dexter, D. W. Kerst, T. W. Lovell, S. C. Prager, and J. C. Sprott, "The Madison Symmetric Torus," *Fusion Technology*, vol. 19, no. 1, pp. 131–139, 1991.

[16] P. Martin, the RFX team, B. Chapman, the MST team, P. Brunsell, J.-A. Malmberg, J. Drake, the EXTRAP T2R team, Y. Yagi, the TPE-RX team, R. White, C. Sovinec, C. Xiao, R. Nebel, and D. Schnack, "Overview of quasi-single helicity experiments in reversed field pinches," *Nuclear Fusion*, vol. 43, no. 12, p. 1855, 2003.

[17] T. D. Rempel, C. W. Spragins, S. C. Prager, S. Assadi, D. J. Den Hartog, and S. Hokin, "Edge electrostatic fluctuations and transport in a reversed-field pinch," *Phys. Rev. Lett.*, vol. 67, pp. 1438–1441, Sep 1991.

[18] R. M. Magee, D. J. Den Hartog, S. T. A. Kumar, A. F. Almagri, B. E. Chapman, G. Fiksel, V. V. Mirnov, E. D. Mezonlin, and J. B. Titus, "Anisotropic ion heating and tail generation during tearing mode magnetic reconnection in a high-temperature plasma," *Phys. Rev. Lett.*, vol. 107, p. 065005, Aug 2011.

[19] J. Sarff, A. Almagri, J. Anderson, M. Borchardt, D. Carmody, K. Caspary, B. Chapman, D. D. Hartog, J. Duff, S. Eilerman, A. Falkowski, C. Forest, J. Goetz, D. Holly, J.-H. Kim, J. King, J. Ko, J. Koliner, S. Kumar, J. Lee, D. Liu, R. Magee, K. McCollam, M. McGarry, V. Mirnov, M. Nornberg, P. Nonn, S. Oliva, E. Parke, J. Reusch, J. Sauppe, A. Seltzman, C. Sovinec, H. Stephens, D. Stone, D. Theucks, M. Thomas, J. Triana, P. Terry, J. Waksman, W. Bergerson, D. Brower, W. Ding, L. Lin, D. Demers, P. Fimognari, J. Titus, F. Auriemma, S. Cappello, P. Franz, P. Innocente, R. Lorenzini, E. Martines, B. Momo, P. Piovesan, M. Puiatti, M. Spolaore, D. Terranova, P. Zanca, V. Belykh, V. Davydenko, P. Deichuli, A. Ivanov, S. Polosatkin, N. Stupishin, D. Spong, D. Craig, R. Harvey, M. Cianciosa, and J. Hanson, "Overview of results from the MST reversed field pinch experiment," *Nuclear Fusion*, vol. 53, p. 104017, Sep 2013.

[20] J. P. Freidberg, *Ideal MHD*. Cambridge University Press, 2014.

[21] R. Robinson, D.C;King, "Factors influencing the period of improved stability in Zeta," *Plasma Physics and Controlled Nuclear Fusion*, vol. 44, no. 25, pp. 263–276, 1969.

[22] J. B. Taylor, "Relaxation of toroidal plasma and generation of reverse magnetic fields," *Phys. Rev. Lett.*, vol. 33, pp. 1139–1141, Nov 1974.

[23] S. Eilerman, *Ion runaway during magnetic reconnection in the reversed-field pinch*. PhD thesis, The University of Wisconsin - Madison, 2014.

[24] S. Munaretto, B. E. Chapman, D. J. Holly, M. D. Nornberg, R. J. Norval, D. J. D. Hartog, J. A. Goetz, and K. J. McCollam, "Control of 3d equilibria with resonant magnetic perturbations in MST," *Plasma Physics and Controlled Fusion*, vol. 57, no. 10, p. 104004, 2015.

[25] T. M. Biewer, C. B. Forest, J. K. Anderson, G. Fiksel, B. Hudson, S. C. Prager, J. S. Sarff, J. C. Wright, D. L. Brower, W. X. Ding, and S. D. Terry, "Electron heat transport measured in a stochastic magnetic field," *Phys. Rev. Lett.*, vol. 91, p. 045004, Jul 2003.

[26] K. A. Werley, C. Bathke, R. A. Krakowski, R. Miller, and J. N. DiMarco, "Plasma confinement requirements for compact RFP reactor (Titan) plasmas operated in a high-radiation mode," *Fusion Technology*, vol. 19, pp. 1266–1271, 05 1991.

[27] J. Freidberg, *Plasma Physics and Fusion Energy*. Cambridge University Press, 2008.

[28] K. Caspary, *Density and Beta Limits in the Madison Symmetric Torus Reversed-Field Pinch*. PhD thesis, University of Wisconsin - Madison, Madison, Wisconsin, March 2014.

[29] J. K. Anderson, *Measurement of the Electrical Resitivity Profile in the Madison Symmetric Torus*. PhD thesis, University of Wisconsin - Madison, Madison, Wisconsin, 2001.

[30] M. Gobbin, L. Marrelli, and R. B. White, "Numerical studies of transport mechanisms in RFX-mod low magnetic chaos regimes," *Plasma Physics and Controlled Fusion*, vol. 51, p. 065010, Apr 2009.

[31] R. Lorenzini, A. Alfier, F. Auriemma, A. Fassina, P. Franz, P. Innocente, D. Lopez-Bruna, E. Martines, B. Momo, G. Pereverzev, P. Piovesan, G. Spizzo, M. Spolaore, and D. Terranova, "On the energy transport in internal transport barriers of RFP plasmas," *Nuclear Fusion*, vol. 52, no. 6, p. 062004, 2012.

[32] R. N. Franklin, "The plasma–sheath boundary region," *Journal of Physics D: Applied Physics*, vol. 36, pp. R309–R320, Oct 2003.

[33] P. R. Brunsell, D. Yadikin, D. Gregoratto, R. Paccagnella, T. Bolzonella, M. Cavinato, M. Cecconello, J. R. Drake, A. Luchetta, G. Manduchi, G. Marchiori, L. Marrelli, P. Martin, A. Masiello, F. Milani, S. Ortolani, G. Spizzo, and P. Zanca, "Feedback stabilization of multiple resistive wall modes," *Phys. Rev. Lett.*, vol. 93, p. 225001, Nov 2004.

[34] J. Drake, P. Brunsell, D. Yadikin, M. Cecconello, J. Malmberg, D. Gregoratto, R. Paccagnella, T. Bolzonella, G. Manduchi, L. Marrelli, S. Ortolani, G. Spizzo, P. Zanca, A. Bondeson, and Y. Liu, "Experimental and theoretical studies of active control of resistive wall mode growth in the EXTRAP T2R reversed-field pinch," *Nuclear Fusion*, vol. 45, pp. 557–564, Jun 2005.

[35] R. Paccagnella, S. Ortolani, P. Zanca, A. Alfier, T. Bolzonella, L. Marrelli, M. E. Puiatti, G. Serianni, D. Terranova, M. Valisa, M. Agostini, L. Apolloni, F. Auriemma, F. Bonomo, A. Canton, L. Carraro, R. Cavazzana, M. Cavinato, P. Franz, E. Gazza, L. Grando, P. Innocente, R. Lorenzini, A. Luchetta, G. Manduchi, G. Marchiori, S. Martini,

R. Pasqualotto, P. Piovesan, N. Pomaro, P. Scarin, G. Spizzo, M. Spolaore, C. Taliercio, N. Vianello, B. Zaniol, L. Zanotto, and M. Zuin, "Active-feedback control of the magnetic boundary for magnetohydrodynamic stabilization of a fusion plasma," *Phys. Rev. Lett.*, vol. 97, p. 075001, Aug 2006.

[36] T. E. Evans, R. A. Moyer, P. R. Thomas, J. G. Watkins, T. H. Osborne, J. A. Boedo, E. J. Doyle, M. E. Fenstermacher, K. H. Finken, R. J. Groebner, M. Groth, J. H. Harris, R. J. La Haye, C. J. Lasnier, S. Masuzaki, N. Ohyabu, D. G. Pretty, T. L. Rhodes, H. Reimerdes, D. L. Rudakov, M. J. Schaffer, G. Wang, and L. Zeng, "Suppression of large edge-localized modes in high-confinement DIII-D plasmas with a stochastic magnetic boundary," *Phys. Rev. Lett.*, vol. 92, p. 235003, Jun 2004.

[37] A. H. Boozer, "Theory of tokamak disruptions," *Physics of Plasmas*, vol. 19, no. 5, 2012.

[38] D. A. Gates and L. Delgado-Aparicio, "Origin of tokamak density limit scalings," *Phys. Rev. Lett.*, vol. 108, p. 165004, Apr 2012.

[39] T. Hender, R. Fitzpatrick, A. Morris, P. Carolan, R. Durst, T. Edlington, J. Ferreira, S. Fielding, P. Haynes, J. Hugill, I. Jenkins, R. L. Haye, B. Parham, D. Robinson, T. Todd, M. Valovic, and G. Vayakis, "Effect of resonant magnetic perturbations on COMPASS-C tokamak discharges," *Nuclear Fusion*, vol. 32, no. 12, p. 2091, 1992.

[40] K. H. Finken, S. S. Abdullaev, M. W. Jakubowski, M. F. M. de Bock, S. Bozhenkov, C. Busch, M. von Hellermann, R. Jaspers, Y. Kikuchi, A. Krämer-Flecken, M. Lehnen, D. Schega, O. Schmitz, K. H. Spatschek, B. Unterberg, A. Wingen, R. C. Wolf, and O. Zimmermann, "Improved confinement due to open ergodic field lines imposed by the dynamic ergodic divertor in TEXTOR," *Phys. Rev. Lett.*, vol. 98, p. 065001, Feb 2007.

[41] P. Tamain, A. Kirk, E. Nardon, B. Dudson, B. Hnat, and the MAST team, "Edge turbulence and flows in the presence of resonant magnetic perturbations on MAST," *Plasma Physics and Controlled Fusion*, vol. 52, no. 7, p. 075017, 2010.

[42] C. D. Michelis and M. Mattioli, "Spectroscopy and impurity behaviour in fusion plasmas," *Reports on Progress in Physics*, vol. 47, pp. 1233–1346, Oct 1984.

[43] M. Wyman, B. Chapman, J. Ahn, A. Almagri, J. Anderson, F. Bonomo, D. Brower, S. Combs, D. Craig, D. D. Hartog, B. Deng, W. Ding, F. Ebrahimi, D. Ennis, G. Fiksel, C. Foust, P. Franz, S. Gangadhara, J. Goetz, R. O'Connell, S. Oliva, S. Prager, J. Reusch,

J. Sarff, H. Stephens, and T. Yates, "Plasma behaviour at high β and high density in the Madison Symmetric Torus RFP," *Nuclear Fusion*, vol. 49, p. 015003, Dec 2008.

[44] Y. Ueda, K. Tobita, and Y. Katoh, "PSI issues at plasma facing surfaces of blankets in fusion reactors," *Journal of Nuclear Materials*, vol. 313-316, pp. 32 – 41, 2003.

[45] K. Behringer, H. P. Summers, B. Denne, M. Forrest, and M. Stamp, "Spectroscopic determination of impurity influx from localized surfaces," *Plasma Physics and Controlled Fusion*, vol. 31, no. 14, p. 2059, 1989.

[46] S. Brezinsek, P. Greenland, P. Mertens, A. Pospieszczyk, D. Reiter, U. Samm, B. Schweer, and G. Sergienko, "On the measurement of molecular particle fluxes in fusion boundary plasmas," *Journal of Nuclear Materials*, vol. 313-316, pp. 967 – 971, 2003.

[47] M. R. Stoneking, S. A. Hokin, S. C. Prager, G. Fiksel, H. Ji, and D. J. Den Hartog, "Particle transport due to magnetic fluctuations," *Phys. Rev. Lett.*, vol. 73, pp. 549–552, Jul 1994.

[48] N. E. Lanier, *Electron density fluctuations and fluctuation-induced transport in the reversed-field pinch*. PhD thesis, The University of Wisconsin - Madison, 1999.

[49] K. Wilson and W. Hsu, "Hydrogen recycling properties of graphite," *Journal of Nuclear Materials*, vol. 145-147, pp. 121 – 130, 1987.

[50] J. Hackmann, Y. C. Kim, E. K. Souw, and J. Uhlenbusch, "Investigation of neutral particle behaviour between plasma and wall including wall interactions," *Plasma Physics*, vol. 20, pp. 309–322, Apr 1978.

[51] R. Norval, J.A.Goetz, and O. Schmitz, "Boundary viewing on the Madison Symmetric Torus," in *Proc. of the 21st Topical Conference on High-Temperature Plasma Diagnostics*, 2016.

[52] F. Chen, "Langmuir probes diagnostics," *Mini-Course on Plasma Diagnostics - IEEE*, vol. 1, no. 1, 2003.

[53] O. Schmitz, J. Coenen, H. Frerichs, M. Kantor, M. Lehnen, B. Unterberg, S. Brezinsek, M. Clever, T. Evans, K. Finken, M. Jakubowski, A. Kraemer-Flecken, V. Phillips, D. Reiter, U. Samm, G. Spakman, and G. Telesca, "Particle confinement control with resonant magnetic perturbations at TEXTOR," *J. Nucl. Mat.*, no. 390-391, pp. 330–334, 2009.

[54] V. Soukhanovskii, R. Maingi, R. Raman, H. Kugel, B. LeBlanc, A. Roquemore, and C. Skinner, "Core fueling and edge particle flux analysis in ohmically and auxiliary heated NSTX plasmas," *Journal of Nuclear Materials*, vol. 313-316, pp. 573 – 578, 2003.

[55] O. Schmitz, J. Coenen, H. Frerichs, M. Kantor, M. Lehnen, B. Unterberg, S. Brezinsek, M. Clever, T. Evans, K. Finken, M. Jakubowski, A. Kraemer-Flecken, V. Phillips, D. Reiter, U. Samm, G. Spakman, and G. Telesca, "Particle confinement control with resonant magnetic perturbations at TEXTOR," *Journal of Nuclear Materials*, vol. 390-391, pp. 330 – 334, 2009. Proceedings of the 18th International Conference on Plasma-Surface Interactions in Controlled Fusion Device.

[56] R. Bell, S. Kaye, D. Stutman, M. Bell, M. Bitter, C. Bourdelle, D. Gates, R. Maingi, S. Medley, J. Menard, D. Mueller, S. Paul, A. Roquemore, A. Rosenberg, S. Sabbagh, V. Soukhanovskii, E. Synakowski, J. Wilson, and t. Team, "Confinement studies of auxiliary heated nstx plasmas," *Nuclear Fusion*, vol. 44, p. 513, 03 2004.

[57] R. Maingi, G. Jackson, M. Wade, M. Mahdavi, P. Mioduszewski, G. Haas, M. Schaffer, J. Hogan, and C. Klepper, "Control of wall particle inventory with divertor pumping on DIII-d," *Nuclear Fusion*, vol. 36, pp. 245–253, feb 1996.

[58] L. A. Stephey, *The Effects of Edge Magnetic Structure on Particle Fueling and Exhaust in the HSX and W7-X Stellarators*. PhD thesis, The University of Wisconsin - Madison, Jan 2017.

[59] H. Dylla, P. LaMarche, M. Ulrickson, R. Goldston, D. Heifetz, K. Hill, and A. Ramsey, "Conditioning of the graphite bumper limiter for enhanced confinement discharges in TFTR," *Nuclear Fusion*, vol. 27, pp. 1221–1230, Aug 1987.

[60] D. Craig, "Magnetic mode analysis in the MST," *MST Internal Document*, 2005.

[61] J. Sarff, A. Almagri, J. Anderson, T. Biewer, A. Blair, M. Cengher, B. Chapman, P. Chattopadhyay, D. Craig, D. D. Hartog, F. Ebrahimi, G. Fiksel, C. Forest, J. Goetz, D. Holly, B. Hudson, T. Lovell, K. McCollam, P. Nonn, R. O'Connell, S. Oliva, S. Prager, J. Reardon, M. Thomas, M. Wyman, D. Brower, W. Ding, S. Terry, M. Carter, V. Davydenko, A. Ivanov, R. Harvey, R. Pinsker, and C. Xiao, "Tokamak-like confinement at a high beta and low toroidal field in the MST reversed field pinch," *Nuclear Fusion*, vol. 43, pp. 1684–1692, Dec 2003.

[62] L. Marrelli, P. Martin, G. Spizzo, P. Franz, B. E. Chapman, D. Craig, J. S. Sarff, T. M. Biewer, S. C. Prager, and J. C. Reardon, "Quasi-single helicity spectra in the Madison Symmetric Torus," *Physics of Plasmas*, vol. 9, no. 7, pp. 2868–2871, 2002.

[63] A. Kramida, Yu. Ralchenko, J. Reader, and and NIST ASD Team. NIST Atomic Spectra Database (ver. 5.6.1), [Online]. Available: https://physics.nist.gov/asd [2019, March 17]. National Institute of Standards and Technology, Gaithersburg, MD., 2018.

[64] M. C. Miller, *Non-Axisymmetric Flows and Transport in the Edge of MST*. PhD thesis, University of Wisconsin - Madison, Madison, Wisconsin, 2011.

[65] L. C. Johnson and E. Hinnov, "Ionization, recombination, and population of excited levels in hydrogen plasmas.," *JQSRT*, vol. 13, pp. 333–358, 1973.

[66] J. Waksman, *Neutral beam heating of a reversed-field pinch in the Madison Symmetric Torus*. PhD thesis, University of Wisconsin - Madison, Madison, Wisconsin, June 2013.

[67] D. H. G. Fiksel, J. Frank, "Fast pyrobolometers for measurements of plasma heat fluxes and radiation losses in the mst reversed field pinch," Tech. Rep. DOE/ER/53198–213, University of Wisconsin - Madison, 1993.

[68] Forschungzentrum Juelich, "The AMJUEL online database," 2006.

[69] K. Sawada and T. Fujimoto, "Effective ionization and dissociation rate coefficients of molecular hydrogen in plasma," *Journal of Applied Physics*, vol. 78, no. 5, pp. 2913–2924, 1995.

[70] W. Eckstein and D. Heifetz, "Data sets for hydrogen reflection and their use in neutral transport calculations," *Journal of Nuclear Materials*, vol. 145-147, pp. 332 – 338, 1987.

[71] R. Schneider, X. Bonnin, K. Borrass, D. P. Coster, H. Kastelewicz, D. Reiter, V. A. Rozhansky, and B. J. Braams, "Plasma edge physics with B2-Eirene," *Contributions to Plasma Physics*, vol. 46, no. 1-2, pp. 3–191, 2006.

[72] Y. Feng, H. Frerichs, M. Kobayashi, A. Bader, F. Effenberg, D. Harting, H. Hoelbe, J. Huang, G. Kawamura, J. D. Lore, T. Lunt, D. Reiter, O. Schmitz, and D. Sharma, "Recent Improvements in the EMC3-Eirene Code," *Contributions to Plasma Physics*, vol. 54, pp. 426–431, June 2014.

[73] W. X. Ding, D. L. Brower, W. F. Bergerson, and L. Lin, "Upgrade of far-infrared laser-based Faraday rotation measurement on MST," *Review of Scientific Instruments*, vol. 81, no. 10, p. 10D508, 2010.

[74] J. D. Hanson, S. P. Hirshman, S. F. Knowlton, L. L. Lao, E. A. Lazarus, and J. M. Shields, "V3Fit: a code for three-dimensional equilibrium reconstruction," *Nuclear Fusion*, vol. 49, p. 075031, Jul 2009.

[75] K. Sawada, K. Eriguchi, and T. Fujimoto, "Hydrogen-atom spectroscopy of the ionizing plasma containing molecular hydrogen: Line intensities and ionization rate," *Journal of Applied Physics*, vol. 73, no. 12, pp. 8122–8125, 1993.

[76] H. Frerichs, F. Effenberg, Y. Feng, O. Schmitz, L. Stephey, D. Reiter, P. Borner, and T. W.-X. Team, "Reconstruction of recycling flux from synthetic camera images, evaluated for the Wendelstein 7-X startup limiter," *Nuclear Fusion*, vol. 57, no. 12, p. 126022, 2017.

[77] E. Vietzke, M. Wada, and M. Hennes, *Reflection and Adsorption of Hydrogen Atoms and Molecules on Graphite and Tungsten*, pp. 51–58. Dordrecht: Springer Netherlands, 2000.

[78] E. Martines, R. Lorenzini, B. Momo, S. Munaretto, P. Innocente, and M. Spolaore, "The plasma boundary in single helical axis RFP plasmas," *Nuclear Fusion*, vol. 50, p. 035014, Mar 2010.

[79] R. Ikezoe, T. Onchi, K. Oki, A. Sanpei, H. Himura, and S. Masamune, "Characterization of MHD behavior in a low-aspect ratio RFP," *J. Plasma Fusion Res*, vol. 8, p. 1031, 2009.

[80] C. P. Kasten, D. J. D. Hartog, H. D. Stephens, C. C. Hegna, and J. A. Reusch, "Electron temperature fluctuations during sawtooth events in a reversed-field pinch," *Plasma Physics and Controlled Fusion*, vol. 53, p. 112001, oct 2011.

[81] T. Biewer, *Electron Thermal Transport in the Madison Symmetric Torus*. PhD thesis, University of Wisconsin - Madison, Madison, Wisconsin, 2002.

[82] B. Chapman, J. Ahn, A. Almagri, J. Anderson, F. Bonomo, D. Brower, D. Burke, K. Caspary, D. Clayton, S. Combs, W. Cox, D. Craig, B. Deng, D. D. Hartog, W. Ding, F. Ebrahimi, D. Ennis, G. Fiksel, C. Forest, C. Foust, P. Franz, S. Gangadhara, J. Goetz, M. Kaufman, J. Kulpin, A. Kuritsyn, R. Magee, M. Miller, V. Mirnov, P. Nonn, R. O'Connell, S. Oliva, S. Prager, J. Reusch, J. Sarff, H. Stephens, M. Wyman, and T. Yates, "Improved-confinement plasmas at high temperature and high beta in the MST RFP," *Nuclear Fusion*, vol. 49, no. 10, p. 104020, 2009.

[83] J. Roth and C. Garcia-Rosales, "Analytic description of the chemical erosion of graphite by hydrogen ions," *Nuclear Fusion*, vol. 36, pp. 1647–1659, Dec 1996.

[84] W. Eckstein and D. Heifetz, "Data sets for hydrogen reflection and their use in neutral transport calculations," *Journal of Nuclear Materials*, vol. 145-147, pp. 332 – 338, 1987.

[85] V. Antoni, M. Bagatin, H. Bergsaker, G. D. Mea, D. Desideri, E. Martines, V. Rigato, G. Serianni, P. Sonato, L. Tramontin, and S. Zandolin, "Plasma wall interaction and

energy fluxes in RFX," *Journal of Nuclear Materials*, vol. 220 - 222, no. 0, pp. 650 – 653, 1995.

[86] P. Innocente, A. Alfier, A. Canton, and R. Pasqualotto, "Plasma performance and scaling laws in the RFX-mod reversed-field pinch experiment," *Nuclear Fusion*, vol. 49, no. 11, p. 115022, 2009.

[87] M. Valisa, T. Bolzonella, L. Carraro, E. Casarotto, S. Costa, L. Garzotti, P. Innocente, S. Martini, R. Pasqualotto, M. Puiatti, R. Pugno, and P. Scarin, "Locked modes induced plasma-wall interactions in RFX," *Journal of Nuclear Materials*, vol. 241 - 243, no. 0, pp. 988 – 992, 1997.

[88] L. Marrelli, P. Martin, A. Murari, and G. Spizzo, "Total radiation losses and emissivity profiles in RFX," *Nuclear Fusion*, vol. 38, no. 5, p. 649, 1998.

[89] Y. Hirano, R. Paccagnella, H. Koguchi, L. Frassinetti, H. Sakakita, S. Kiyama, and Y. Yagi, "Quasi-single helicity state at shallow reversal in TPE-RX reversed-field pinch experiment," *Physics of Plasmas*, vol. 12, no. 11, 2005.

[90] G. Razdobarin, V. Semenov, L. Sokolova, I. Folomkin, V. Burakov, P. Misakov, P. Naumenkov, and S. Nechaev, "An absolute measurement of the neutral density profile in the tokamak plasma by resonance fluorescence on the H-alpha line," *Nuclear Fusion*, vol. 19, no. 11, p. 1439, 1979.

[91] J. A. Reusch, M. T. Borchardt, D. J. Den Hartog, A. F. Falkowski, D. J. Holly, R. OâŁ™-Connell, and H. D. Stephens, "Multipoint Thomson scattering diagnostic for the Madison Symmetric Torus reversed-field pinch," *Review of Scientific Instruments*, vol. 79, no. 10, p. 10E733, 2008.

[92] J. C. Reardon, D. Craig, D. J. Den Hartog, G. Fiksel, and S. C. Prager, "Comparison of ion temperature diagnostics on the madison symmetric torus reversed-field pinch," *Review of Scientific Instruments*, vol. 74, no. 3, pp. 1892–1895, 2003.

[93] K. J. McCollam, A. P. Blair, S. C. Prager, and J. S. Sarff, "Oscillating-field current-drive experiments in a reversed field pinch," *Phys. Rev. Lett.*, vol. 96, p. 035003, Jan 2006.